Ultrafast spectroscopy of ionic and covalent nanocrystals

Colin Sonnichsen, Dept. of Chemistry
McGill University, Montreal
December, 2020

A thesis submitted to McGill University in partial fulfillment of the requirements of the degree of

Doctorate of Philosophy

©Colin Sonnichsen, June 8, 2021

Abstract

Nanomaterials are being used in more and more applications and questions regarding the destiny of excited charges in these systems has become more pressing than ever. As the physics of confined carriers in traditional, II-VI systems comes to an almost full understanding, perovskite based nanocrystals have emerged as the new promising platform. In this thesis I present a brief overview of nanocrystal physics in two systems; covalently bound CdSe, and ionically bound CsPbBr₃ perovskites.

CdSe is a benchmark for comparison to other systems due to its well-resolved excitonic peaks and solid theoretical foundation. Perovskite nanocrystals are novel systems that show quantum confinement and high photoluminescent quantum yield, whose material properties are being intensely studied. These two systems are examined and contrasted with ultrafast, state-resolved pump-probe spectroscopy. These results and their implications to quantum confinement and material physics will be discussed. Interesting phenomena emerge, related to electron-lattice coupling, quantum confinement, exciton relaxation and Auger recombination.

In the last chapter of this thesis, I present results from multi-dimensional spectroscopy. By using an OPA-driven hollow core fibre, tunable, broadband pulses are generated that are ideal for multi-dimensional spectroscopy. A characterization of this source and initial results on CdSe quantum dots demonstrate the expansion of this powerful spectroscopy to new samples.

Abrégé

Les nanomatériaux sont utilisés dans de plus en plus d'applications et les questions qui concernent le destin des charges excitées dans ces systèmes sont devenues plus urgentes que jamais. Alors que la physique des porteurs confinés dans les systèmes II-VI traditionnels arrive à une compréhension presque complète, des nanocristaux à base de pérovskite sont émergés comme la nouvelle plate-forme prometteuse. Dans cette thèse, je présente un bref sommaire de la physique des nanocristaux dans deux systèmes; CdSe avec ses liaisons covalentes et CsPbBr₃ perovskites avec ses liaisons ioniques.

CdSe est un système de référence pour comparaison aux autres systèmes dû a ces pics excitoniques bien résolus et solide fondation théorique. Les nanocristaux de pérovskite sont de nouveaux systèmes qui présentent un confinement quantique et un rendement quantique photoluminescent élevé, dont les propriétés matériaux sont le sujet d'intenses études. Ces deux systèmes sont examinés et mis en contraste avec une spectroscopie pompe-sonde ultra-rapide avec résolution par état. Ces résultats et leurs implications pour le confinement quantique et la physique des matériaux seront discutés. Des phénomènes intéressants émergent, liés au couplage électron-réseau, au confinement quantique, à la relaxation des excitons et à la recombinaison Auger.

Dans le dernier chapitre de cette thèse, je présente des résultats de la spectroscopie multidimensionnelle. En utilisant une fibre à centre-creux pilotée par un amplificateur paramétrique, des impulsions accordables à large bande sont générées, idéales pour la spectroscopie multidimensionnelle. Une caractérisation de la source et les premiers résultats sur les boîtes quantiques de CdSe démontrent l'expansion de cette puissante spectroscopie à de nouveaux échantillons.

Acknowledgement

This thesis couldn't be possible without the contributions of many people. First and fore-most, my thesis supervisor Patanjali Kambhampati. Thanks for giving me expensive, fancy toys with which to do science. Thank you for also giving me the freedom to take apart, put back together, and occasionally break those expensive toys. Without Pat's guidance and scientific discussion, much of my results would remain unexplained and unpublished, so for his approach to material science I am also grateful.

Professor Tobias Kipp, from Universität Hamburg, worked with me for a year learning how to do state-resolved pump-probe spectroscopy. Together, we figured it out through a combination of trial-and-error and common sense. He also brought the CdSe/CdS DiRs samples used for chapter 4. I'll remember very fondly the long days we spent taking things apart and pressing random buttons on a 10 year old Labview script. He played a role of senior adviser to the entire group and brought a great perspective to all of our work.

The other members of the Kambhampati group I overlapped with were instrumental in shaping my ideas as a scientist and keeping me sane throughout these past several years. Brenna Walsh was instrumental in getting lab 1 working again, and was a joy to work with. Lakshay Jethi and Tim Mack did a phenomenal job pumping out CdSe

samples for the basement lab. Scientifically speaking, I owe the most to Hélène Seiler and Samuel Palato. Together they built the multi-dimensional spectrometer. Both Sam and Helene are inspirations for any student that had the privilege of working with them. Patrick Brosseau quickly learned how to work the basement lab and brought insights to our work there. He also helped a lot with the experimental and theoretical work in chapters 5 and 6. Harry Baker brought a lot of fun and energy to our group, and has helped keep us all on our toes with his quick wit. Dallas Strandell, thanks for putting up with all of my requests for samples. I think it happened more than once where you worked hard to make something on short notice, only for me to fail to have the laser ready when I said it would be. I'm honestly surprised you never said no. Gabriela, we didn't overlap as much, but your sensible personality and pleasant demeanor are a great break from a stressful day. And finally, Cameron Reid. I had a lot of fun working with you to get that last bit of data for this thesis. Keep working hard, and don't be afraid to touch *all* the knobs. Especially if a service call is coming!

Our office is shared with the students of Bradley Siwick, and we inevitably formed friendships and discussed our respective science projects. For this, I must thank Martin Otto, Laurent René de Cotret, and Mark Stern. I am grateful to my thesis committee, Bradley Siwick and Gonzalo Cosa. They provided useful insight and made sure I was on the right track with my research.

Lastly, I must thank my supportive and patient wife Caroline King. She took on plenty of extra dog walks and lonely suppers to make this work possible. Here's to the next experiment!

Table of Contents

A	bstra	ct		i
A	brégé	<u>.</u>		ii
A	cknov	wledge	ements	ii
St	atem	ent of o	contributions	viii
Li	st of	Figures	S	viii
Li	st of	Tables		xi
Li	st of	Abbrev	viations	xiii
In	trodu	ıction		1
1	Phy	sics of	Nanocrystals	7
	1.1	Band	theory of bulk semiconductors	. 7
		1.1.1	Tight-Binding Model	. 8
		1.1.2	Nearly Free Electrons	. 10
		1.1.3	Effective Mass Approximation	. 12
		1.1.4	Excitons	. 14
		1.1.5	Electron-phonon coupling in semiconductors	. 15
	1.2	Quan	tum mechanics of a Semiconductor Nanocrystal	. 18
		1.2.1	Particle in a Sphere	. 18
		1.2.2	Covalent II-VI Quantum dots	. 21
		1.2.3	Ionically bound ABX ₃ perovskite nanocrystals	. 24

2	Pun	ıp-prol	be spectroscopy	32
	2.1	Gener	rating short pulses	33
		2.1.1	Chirped pulse amplification	36
		2.1.2	Describing pulse phase	37
		2.1.3	Measuring ultrafast pulses	38
	2.2	Pump	p-probe spectroscopy of semiconductor nanocrystals	43
		2.2.1	State-resolved pump-probe spectroscopy	44
		2.2.2	Contributions to the SRPP signal	47
		2.2.3	Electronic relaxation	49
		2.2.4	Auger recombination	52
		2.2.5	Gain	54
	2.A	Popul	ation kinetics in 2, 3 and 4 level laser systems	64
		2.A.1	2-level systems	64
		2.A.2	3-level systems	65
		2.A.3	4-level systems	67
3	Two	-dimer	nsional Spectroscopy	70
	3.1	The 21	DES signal	72
		3.1.1	System response function	73
		3.1.2	Implementation of 2DES	79
		3.1.3	Electronic vs Vibrational Coherence	83
	3.2	Broad	band sources for 2DES	89
		3.2.1	NOPAs	90
		3.2.2	Hollow-core fibres	94
4	CdS	se / CdS	S Dots-in-Rods as a Gain Medium	99
	4.1	Introd	luction	99
	4.2	CdSe/	/Cds Dot-in-Rods	101
	4.3	Gain I	Measurements	106
	4.4	Surfac	re coupling	109

5	Qua	intum confinement in bulk-regime Perovskite nanocrystals	12 1
	5.1	Introduction	122
	5.2	SRPP results	126
	5.3	Relaxation and recombination	129
	5.A	Modelling the TA spectrum of CdSe quantum dots	141
6	An (OPA-driven hollow core fibre as a tunable source for 2DES	14 4
	6.1	Introduction	145
	6.2	Modelling	147
	6.3	Results	149
	6.4	Conclusion	151
Su	ımma	ary and outlook	155

Statement of Contributions

All of the text in chapters 1-3 was written by Colin Sonnichsen, with four figures adapted from the literature, figures 1, 2.6, 2.10, 2.8, 3.9, and 3.11 specifically. For specific citations, see the figure captions or the main text.

Chapter 4 discusses pump-probe results on CdSe dots with an overgrown CdS shell. These samples were prepared by Dr. Xiao Tang. The data were obtained by C. Sonnichsen and Prof. Tobias Kipp. T. Kipp also provided the TEM image shown in figure 6.2 and single crystal data presented in figures 4.3 and 4.4 from his lab in Hamburg. The Auger recombination data for CdSe and CdSe/ZnS samples presented in figure 4.8 were obtained by Dr. Pooja Tyagi in 2011. The data were analysed and presented by C. Sonnichsen. The text was written by C. Sonnichsen with editorial input from T. Kipp and Prof. Patanjali Kambhampati.

The data presented in chapter 5 were obtained by C. Sonnichsen, except for the data in figure 5.3**g**, which was obtained by previous student Dr. Sagar Doderri in 2008. The TEM image presented in the inset of figure 5.2**a** was obtained by Dallas Strandell. The CsPbBr₃ sample was prepared by D. Strandell, and the CdSe sample was purchased from NNLabs. Analysis was performed by C. Sonnichsen, with some modelling parameters provided by Patrick Brosseau, namely the multimode-Brownian oscillator modelling in figure 5.3**d**,**h**. Text was written by C. Sonnichsen with significant input from P. Kambhampati.

Data presented in chapter 6 were acquired by C. Sonnichsen, Cameron Reid, and P. Brosseau. Modelling of fibre output, shown in figure 6.3 was performed by P. Brosseau. Analysis and presentation of data were performed by C. Sonnichsen. Text was prepared by C. Sonnichsen.

List of Figures

1	Various applications of nanocrystals across physics, chemistry, and engi-	
	neering	2
1.1	A molecular Orbital diagram for an infinite crystal of CdSe	9
1.2	Band structure from a periodic potential	13
1.3	The first three radial wavefunctions for the particle in a sphere	20
1.4	The energy levels of a II-VI quantum dot	22
2.1	Longitudinal modes and pulse duration in a mode-locked laser	35
2.2	Ultrafast pulse measurement	40
2.3	Cross-correlation of optical pulses	41
2.4	SRPP experimental layout	45
2.5	Contributions to the transient absorption signal of CdSe QDs	49
2.6	Overview of carrier cooling in CdSe QDs	51
2.7	Auger recombination in CdSe QDs	53
2.8	Red and Green Lasing from CdSe QD films	55
2.9	Types of heterostructures classified by band alignment. Hole wavefunc-	
	tions are depicted in blue, electron wavefunctions in red	56
2.10	Two signs of ASE in thin films of CsPbBr ₃ NCs	58
2.11	Energy level diagram showing a 3 level laser system and relevant popula-	
	tion transfer rates	66

2.12	Energy level diagram showing a 4 level laser system and relevant popula-
	tion transfer rates
3.1	Common lineshapes observed in linear spectroscopy 71
3.2	The DSFD for the $R_1^{(3)}$ rephasing pathway
3.3	Double-sided Feynman diagrams for a 3 level system
3.4	The DSFDs for a two pulse pump-probe experiment. These correspond to
	a Ground state bleach, b Stimulated emission, and c Excited state absorption. 79
3.5	Geometry and phase-matching for box-CARS 2DES 80
3.6	Acquiring the 2DES signal in pump-probe geometry 83
3.7	2DES spectroscopic capabilities
3.8	Systems and pathways that produce coherent beats in 2DES 85
3.9	Electronic vs. vibrational coherences in 2DES
3.10	Coherent vibrations in SRPP
3.11	Geometry and pulse characteristics of a NOPA
4.1	Energy level diagram showing absorptive and emissive states for the exci-
	ton and biexciton in quantum confined systems
4.2	Linear absoprtion, emission and pump-probe spectrum of the CdSe/CdS
	DiR system
4.3	Single crystal emission trace for a CdSe/CdS DiR
4.4	Population decay of a single CdSe/CdS DiR crystal
4.5	Overview of SRPP results for CdSe/CdS DiRs
4.6	Gain properties of CdSe/CdS DiRs as captured through SRPP 107
4.7	Phonons in CdSe/CdS DiRs
4.8	Auger recombination of biexcitons show good surface passivation in CdSe/CdS
	DiRs
4.9	Energetics of states involved in gain revealed by linear and non-linear spec-
	troscopies for CdSe/CdS DiRs

5.1	Electron-phonon coupling in covalent CdSe
5.2	Electron-phonon coupling in ionic perovskite systems
5.3	Overview of SRPP signals in $CsPbBr_3$ and $CdSe$ systems
5.4	Extracting lineshape dynamics in CsPbBr ₃ NCs and CdSe QDs 128
5.5	Presentation of lineshape dynamics in $CsPbBr_3\ NCs$ and $CdSe\ QDs\ \dots\ 130$
5.6	Carrier cooling and multiexciton recombination in bulk-regime CsPbBr $_3$ NCs131
5.7	Auger recombination in a bulk-like model for CsPbBr ₃ NCs
5.8	Result of fitting CdSe QD linear absorption data
5.9	Result of fitting CdSe QD transient absorption data
6.1	A hollow-core fibre driven by OPA pulses for tunable continuum generation 147
6.2	Fiber stability measurements
6.3	Simulated fiber performance across pressure and wavelength
6.4	Experimental 2DES results on CdSe QDs

List of Tables

1.1	Frölich coupling constants for ionic and covalent crystals
4.1	Results of biexciton structure measurements across CdSe QD samples 114
5.1	Fit parameters for the linear absorption model of CdSe in equation 5.13 and
	shown in figure 5.8
5.2	Fit results for the transient absorption model presented in equation 5.14-
	5.17 and figure 5.9

List of Acronyms

2DES two-dimensional electronic spectroscopy

ASE amplified spontaneous emission

CEP carrier-envelope phase

cw continuous-wave

DiR dot-in-rod

ESA excited state absorption

FFCF frequency-fluctuation correlation function

FROG frequency-resolved optical gating

GSB ground state bleach

GVD group-velocity dispersion

HCF hollow-core fibre

NC nanocrystal

NOPA non-collinear optical parametric amplifier

PES potential energy surface

PL photoluminescense

SE stimulated Emission

SFG sum-frequency generation

SRPP state-resolved pump-probe

TG transient-grating

TMDC transition metal dichalcogenide

QD quantum dot

The power of ultrafast spectroscopy in materials science

Materials science of nanostructures is a broad discipline spanning physics, chemistry, biology, engineering, statistical thermodynamics and applied mathematics. On the nanoscale, many physical properties change. Surface area becomes very large relative to crystal volume, with implications for catalysis, surface states, mechanical and thermal properties. Thermal fluctuations also play a large role in the synthesis and stability of nanosystems. Important classes of nanosystems are nanocrystals, small crystals with dimension less than 100 nm. Nanocrystals have been used for multi-photon upconversion in lanthanide-doped systems [1, 2], allowing super-resolution multi-photon microscopy [3], localized plasmon enhanced light absorption in metal nanoparticles [4], antimicrobial coatings from wide band gap nanocrystals [5], quantum computing [6] and cryptography platforms [7, 8] in epitaxially grown nanosystems, light emitting systems now being used in consumer electronics [9] and solar photovoltaics [10]. Some of these applications are shown in figure 1.

All of these systems behave differently, and their interesting properties arise for different reasons. In metal nanoparticles, such as gold or silver nanoparticles, the electrons can move collectively and respond to electromagnetic radiation like a liquid being sloshed in a bucket. This collective response is called a plasmon, and has resonant be-

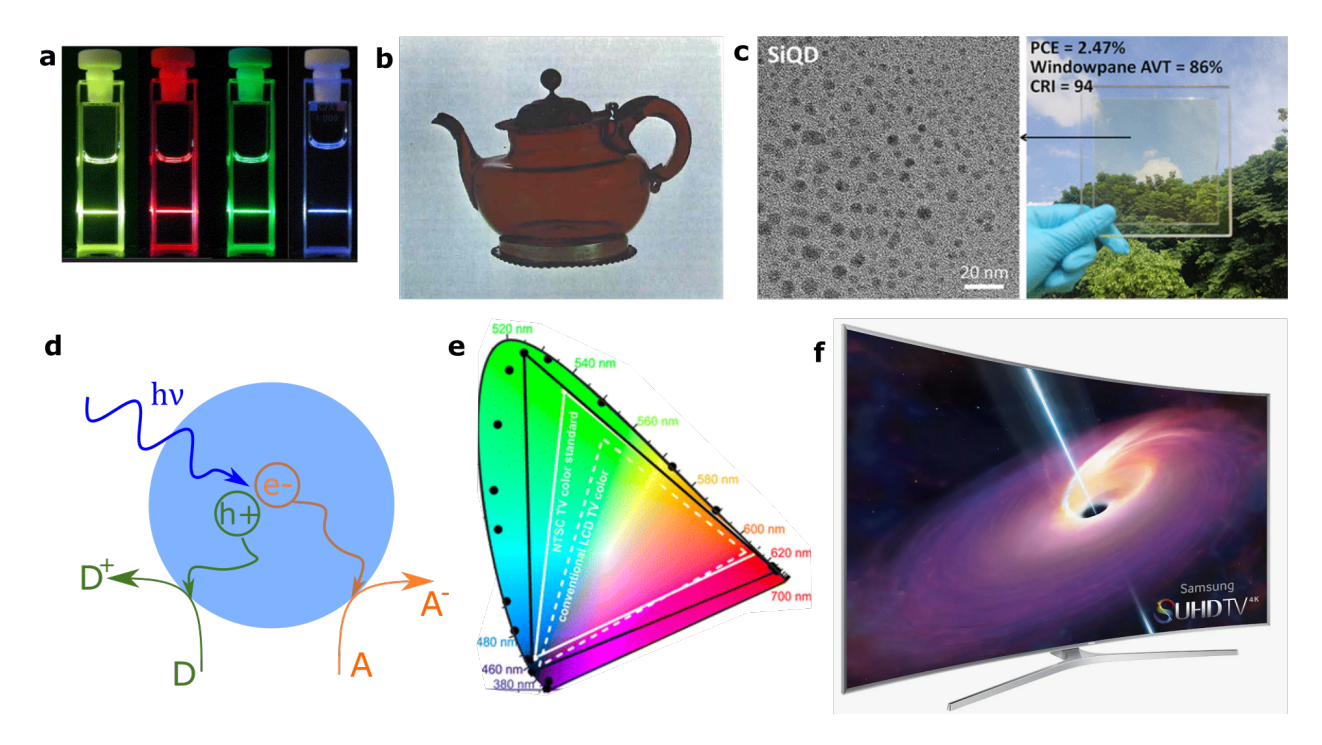


Figure 1: Various applications of nanocrystals across physics, chemistry, and engineering. **a** Lanthanide doped nanocrystals undergoing photon upconversion. These samples are all pumped in the IR but emit visible light. **b** Gold nanoparticles are responsible for the deep red color in many ceramics, such as this teapot from the 17th century. **c** Nanocrystals have been used in transparent solar photovoltaics. Here Si nanocrystals, shown on the left, are the active layer in the solar cell on the right. **d** In wide bandgap materials high energy electrons and holes can be used to drive chemical reactions on the nanocrystal surface. **e** Nanocrystals can be tuned through size or composition to emit over the entire visible spectrum, providing greater color purity than previous standards. **f** This color purity has inspired the use of nanocrystals for lighting and displays, such as this QLED television. Figures reproduced from [2](a), [11](b), [12](c), [13](e) and [9](f)

haviour. The frequency of this resonance is size-dependent, and this is the principle way that optical behaviour of metal nanoparticles changes with size. This plasmon resonance has been used in nanomedicine. An injection of metal nanoparticles is relatively harmless, until they are heated by an outside laser to create highly localized tissue damage, for example at the site of a tumour [14].

Wide-gap nanocrystals, such as TiO₂, usually act in a catalytic way or as an oxygen sensitizer. Here, absorption of a UV photon creates an excited electron with lots of potential energy. This can then react with oxygen to form triplet oxygen, which has antimicrobial properties. This highly excited electron can also be used to break down pollutants or organic compounds, which has found an application in self cleaning concrete [15]. The high reactivity of these nanocrystals is due to their large surface area; excited charges in the core of the nanocrystal quickly react with adsorbed species on the nanocrystal surface.

Perhaps the most scientifically interesting applications of nanocrystals are in opto-electronics. Here quantum confinement tunes the optical absorption and emission of the nanocrystal. When quantum confinement effects are important, the nanocrystal is referred to as a quantum dot (QD), and these act as artificial atoms. The electronic wavefunctions in a QD have similar forms to atomic orbitals, and discrete states fan out as quantum dots decrease in size. This creates a platform for tunable optical properties, simply change the size of the QD so that transitions are at the desired wavelength. These systems are also bright emitters, with appropriate synthesis photoluminescence quantum yields can be in the range of 0.8 - 0.95. Quantum dots can be grown either epitaxially, as strained islands between buffer layers in III-V materials [16], or through nucleation in a solvent [17].

To study optical properties, the most obvious tool is optics. By interrogating these opto-electronic nanosystems with light it is possible to find absorption resonances and emission spectra. By using coherent, monochromatic laser radiation it is possible to do Raman spectroscopy and determine phonon spectra [18] and surface coupling [19]. Through short, single nanosecond pulsed excitation it is possible to determine the lifetime of the excited state. To capture the earliest events, such as relaxation through a manifold of excited states, it is necessary to use ultrafast lasers with pulses on the order of 100 fs in duration. With this incredible temporal resolution it is possible to watch electrons relax from one state to the next, or see the atomic nuclei move to accommodate a new charge distribution.

In this thesis I will explore some of the important concepts in ultrafast spectroscopy of nanocrystals and show data and results drawn from my own research. Using state-resolved pump/probe spectroscopy I explore the ultrafast dynamics in CdSe and CsPbBr₃ systems. In my research I have also used multidimensional non-linear spectroscopies, and I report experimental developments I have made in that area. The results presented here highlight the importance of the lattice response to an excited charge. If the response is underdamped there is little charge-screening. On the other hand, if the lattice is highly damped, excited charges will be confined by the displaced lattice potential. The deformed lattice potential can cause quantum confinement effects in systems that are not in a quantum size regime.

Bibliography

- [1] Song, H.; Sun, B.; Wang, T.; Lu, S.; Yang, L.; Chen, B.; Wang, X.; Kong, X. Solid State Communications **2004**, 132, 409–413.
- [2] Suyver, J. F.; Aebischer, A.; Biner, D.; Gerner, P.; Grimm, J.; Heer, S.; Krämer, K. W.; Reinhard, C.; Güdel, H. U. *Optical Materials* **2005**, 27, 1111–1130.
- [3] Chen, L.; Li, B.; Zhang, C.; Huang, X.; Wang, X.; Xiao, M. Nano Letters 2018, 18, 2074–2080.
- [4] Amendola, V.; Pilot, R.; Frasconi, M.; Maragò, O. M.; Iatì, M. A. *Journal of Physics Condensed Matter* **2017**, 29.
- [5] Fu, G.; Vary, P. S.; Lin, C. T. Journal of Physical Chemistry B **2005**, 109, 8889–8898.
- [6] Kloeffel, C.; Loss, D. Annual Review of Condensed Matter Physics 2013, 4, 51–81.
- [7] Waks, E.; Inoue, K.; Santori, C.; Fattal, D.; Vuckovic, J.; Solomon, G.; Zhang, B.; Yamamoto, Y. **2015**, *420*, 187904.
- [8] Chang, W. H.; Chen, W. Y.; Chang, H. S.; Hsieh, T. P.; Chyi, J. I.; Hsu, T. M. *Physical Review Letters* **2006**, *96*, 3–6.
- [9] Moynihan, T. WIRED.com 2015.
- [10] Lu, D. NewScientist **2020**.

- [11] Hunt, L. B. Gold Bulletin 1976, 9, 134–139.
- [12] Han, S.; Chen, G.; Shou, C.; Peng, H.; Jin, S.; Tu, C. C. ACS Applied Materials and Interfaces 2020, 12, 43771–43777.
- [13] Protesescu, L.; Yakunin, S.; Bodnarchuk, M. I.; Krieg, F.; Caputo, R.; Hendon, C. H.; Yang, R. X.; Walsh, A.; Kovalenko, M. V. *Nano Letters* **2015**, *15*, 3692–3696.
- [14] Hirsch, L. R.; Stafford, R. J.; Bankson, J. A.; Sershen, S. R.; Rivera, B.; Price, R. E.; Hazle, J. D.; Halas, N. J.; West, J. L. Proceedings of the National Academy of Sciences of the United States of America 2003, 100, 13549–13554.
- [15] Jafari, H.; Afshar, S. Photochemistry and Photobiology 2016, 92, 87–101.
- [16] Leonard, D. Journal of Vacuum Science & Technology B: Microelectronics and Nanometer Structures **1994**, 12, 1063.
- [17] Peng, Z. A.; Peng, X. Journal of the American Chemical Society **2001**, 123, 183–184.
- [18] Yaffe, O.; Guo, Y.; Tan, L. Z.; Egger, D. A.; Hull, T.; Stoumpos, C. C.; Zheng, F.; Heinz, T. F.; Kronik, L.; Kanatzidis, M. G.; Owen, J. S.; Rappe, A. M.; Pimenta, M. A.; Brus, L. E. Physical Review Letters 2017, 118, 1–12.
- [19] Mack, T. G.; Jethi, L.; Kambhampati, P. Journal of Physical Chemistry C 2017, 121, 28537–28545.

Chapter 1

Physics of Nanocrystals

To understand the spectroscopy of nanocrystals and quantum confined structures, it is necessary to know the energy level structure of these systems. For confined structures that are in a quantum dot regime, rather than a molecular regime, it is easiest to start from the level structure of a bulk solid, then add confining potentials as a perturbation to the bulk band structure. In this chapter we will explore the well known physics of both covalent II-VI quantum dots and ionic perovskite-based quantum dots.

1.1 Band theory of bulk semiconductors

The defining characteristic of any crystal is its periodicity. The repeating motif of the crystal unit cell and its periodic boundary conditions is imparted to the quantum mechanical properties of the material. The energy structure and wavefuntion both take on the period of the lattice. This is described using equations 1.1-1.4, where Ψ is the total wavefunction, n is an integer, and \vec{a} is the lattice constant. This periodicity is the motivation for a plane wave expansion:

$$U(\vec{r}) = U(\vec{r} + n\vec{a}) \tag{1.1}$$

$$\Rightarrow |\Psi(\vec{r})|^2 = |\Psi(\vec{r} + n\vec{a})|^2 \tag{1.2}$$

$$\Rightarrow \Psi(\vec{r}) = u_k(\vec{r})e^{i\vec{k}\cdot\vec{r}} \tag{1.3}$$

$$=\sum_{k=-\pi/a}^{\pi/a} C_k e^{i\vec{k}\cdot\vec{r}} \tag{1.4}$$

Where the envelope function $u_k(\vec{r})$ is periodic, $u_k(\vec{r}) = u_k(\vec{r} + n\vec{a})$. For a crystal of dimension $L_x \times L_y \times L_z$, the values of \vec{k} that are allowed in equation 1.4 are given by the periodic boundary conditions.

$$\vec{k} = \frac{2\pi n_x}{L_x} a_x \hat{x} + \frac{2\pi n_y}{L_y} a_y \hat{y} + \frac{2\pi n_z}{L_z} a_z \hat{z}$$
(1.5)

Here the set of integers n_i range between $\pm N_i/2$, and \hat{x} , \hat{y} , and \hat{z} are unit vectors. The conditions in equation 1.5 ensure that $|\Psi(\vec{r})| = |\Psi(\vec{r} + \vec{a})|$.

1.1.1 Tight-Binding Model

The wavefunction of any crystal must satisfy equation 1.1. As a specific example, let us take a tight-binding approach to solve for the electronic energy levels of a solid. In the tight-binding model, the electrons at a given lattice site are tightly bound to the atomic potential, and there is only a small wavefunction overlap with neighboring sites. This means the actual potential can be treated as a perturbation to the atomic potential, and the atomic orbitals should form a good basis set. This is in opposition to a free-electron approximation, where there is significant overlap between sites and electrons travel from site to site very easily. Given a cubic structure crystal of only a single atomic species, e.g.

Si or Ge, the energy of an electron in an s orbital in this lattice is E_s , the isolated orbital energy, minus a bonding energy, Δ , that is shared with its' 6 nearest neighbours.

$$H = \sum_{n=0}^{5} E_s |n\rangle \langle n| - \Delta_{ss} |n\rangle \langle n \pm 1|$$
(1.6)

The relations in equation 1.1 show that $|n\pm 1\rangle=|n\rangle\,e^{\pm i\vec{k}\cdot\vec{r}}$. Substituting this back into equation 1.6 yields the following Hamiltonian relation, now for a single lattice site:

$$E(\vec{k}) = E_s - \Delta_{ss} \sum_{n=0}^{5} e^{i\vec{k} \cdot \vec{r_n}}$$
 (1.7)

$$= E_s - 2\Delta_{ss}\cos(\vec{k}\cdot\vec{a}) \tag{1.8}$$

A similar approach can be used to find the energy of p orbitals, sp orbitals, and other excited orbitals. This leads to a band diagram that resembles the one shown in figure 1.1. Including interactions from the eight diagonal neighbors of the lattice site and between more electronic orbitals will produce a more accurate prediction of energy.

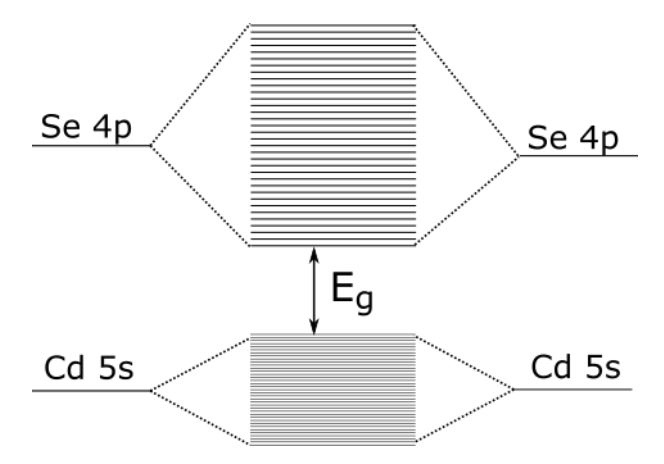


Figure 1.1: A molecular Orbital diagram for an infinite crystal of CdSe. The valence band is made up of Cd 5s orbitals, and the conduction band is made up of Se 4p orbitals.

Nearly Free Electrons 1.1.2

Another way to think of electronic structure in crystals is by thinking of electrons as moving freely through the solid. The dispersion relation of a freely moving electron is given by the well known form $\epsilon_k = \frac{\hbar^2 k^2}{2m_e}$. The effect of the lattice is twofold: to change the effective mass of the electron, and to introduce electronic bands.

For certain values of the wavevector, the electronic wave couples resonantly with the lattice wave, leading to standing wavefunctions and an energy gap. This occurs when $\vec{k}=\pm n\pi/\vec{a}.$ A formal description of this approach for a single electron in one dimension is developed below, largely following that of Kittel's Introduction to Solid State Physics [1].

Free electron wavefunctions and energies will form the basis set for this approach, as opposed to atomic orbitals in the tight-binding approach. These are given by equations 1.10.

$$\psi_k(\vec{r}) = e^{i\vec{k}\cdot\vec{r}} \tag{1.9}$$

$$\psi_k(\vec{r}) = e^{i\vec{k}\cdot\vec{r}}$$

$$\epsilon_k = \frac{\hbar^2}{2m_e} k^2$$
(1.9)

For a crystal potential U(x), the potential will have the same period as the lattice, i.e. U(x) = U(x + a). Because of this periodicity, the potential can be expanded in the reciprocal lattice vectors G.

$$U(x) = \sum_{G} U_G e^{iGx} \tag{1.11}$$

According to the Bloch theorem, and the periodic boundary conditions of the lattice, the solution to the Schrödinger equation must have a particular form:

$$\psi_k(\vec{r}) = u_k(\vec{r})e^{i\vec{k}\cdot\vec{r}} \tag{1.12}$$

With $u_k(\vec{r})$ having the period of the lattice, i.e. $u_k(\vec{r}) = u_k(\vec{r} + \vec{a})$.

This form of the potential can be substituted directly into the time-independent Schrödinger equation, as in 1.15. In combination with our electronic basis set, given by equation 1.1, we have:

$$\left(\frac{-\hbar^2}{2m_e}\frac{\partial^2}{\partial x^2} + \sum_G U_G e^{iGx}\right)\psi_k(x) = \epsilon\psi_k(x) \tag{1.13}$$

$$\left(\frac{-\hbar^2}{2m_e}\frac{\partial^2}{\partial x^2} + \sum_G U_G e^{iGx}\right) \sum_k C_k e^{ikx} = \epsilon \sum_k C_k e^{ikx} \tag{1.14}$$

$$\Rightarrow \sum_{k} \left(\frac{\hbar^2 k^2}{2m_e} - \epsilon \right) C_k + \sum_{k,G} U_G C_k e^{Gx} = 0$$
 (1.15)

Because this sum holds for all k, we can simplify to the central equation:

$$(\lambda_k - \epsilon) C_k = \sum_G U_G C_{k-G}$$
(1.16)

With $\lambda_k=\hbar^2k^2/2m_e$. Here the U_g can be interpreted as the various harmonic Fourier components of the lattice potential. For a sinusoidal potential, $U(x)=U\cos(\pi x/a)$, There would be only one Fourier component to the potential and the Hamiltonian takes

the form below:

$$\mathcal{H} = \begin{pmatrix} U & \lambda_{k-1} & U & 0 & 0 & \cdots \\ 0 & U & \lambda_{k} & U & 0 & \cdots \\ 0 & 0 & U & \lambda_{k+1} & U & \cdots \\ \vdots & \vdots & \vdots & \vdots & \vdots & \ddots \end{pmatrix}$$
(1.17)

The eigenvalues of this matrix can be labelled ϵ_{nk} . For each value of k, there is now a spectrum of energy states available, instead of simply $\hbar^2 k^2/2m_e$. The subscript n refers to one particular solution of equation 1.17 for a given k. Across a single n, the k dependence to the energy will yield a quasi-continuous band of states. At a single k, there will be large discrete jumps in energy going from one band to another. This is depicted in Figure 1.2a. It is clear that the ϵ_{nk} are periodic in k, which should be expected. To simplify things, it is conventional to only look in the region $k \in [-\pi/a, \pi/a]$, as in figure 1.2b.

It should further be noted, that since an optical photon carries very little momentum compared to band edge electrons, only direct, vertical transitions in k-space are allowed. Indirect transitions require a lattice vibration or phonon to be born or annihilated with the photon to compensate the extra momentum associated with moving over in k-space, and these have much smaller probabilities. Both types of transition are shown in figure 1.2b.

1.1.3 Effective Mass Approximation

No matter the approach for calculating bands and energies, it is often the case in semiconductors that band edges are nearly parabolic in shape, particularly near the band edge. This gives rise to the useful concept of an effective mass. For k near the band edge, which

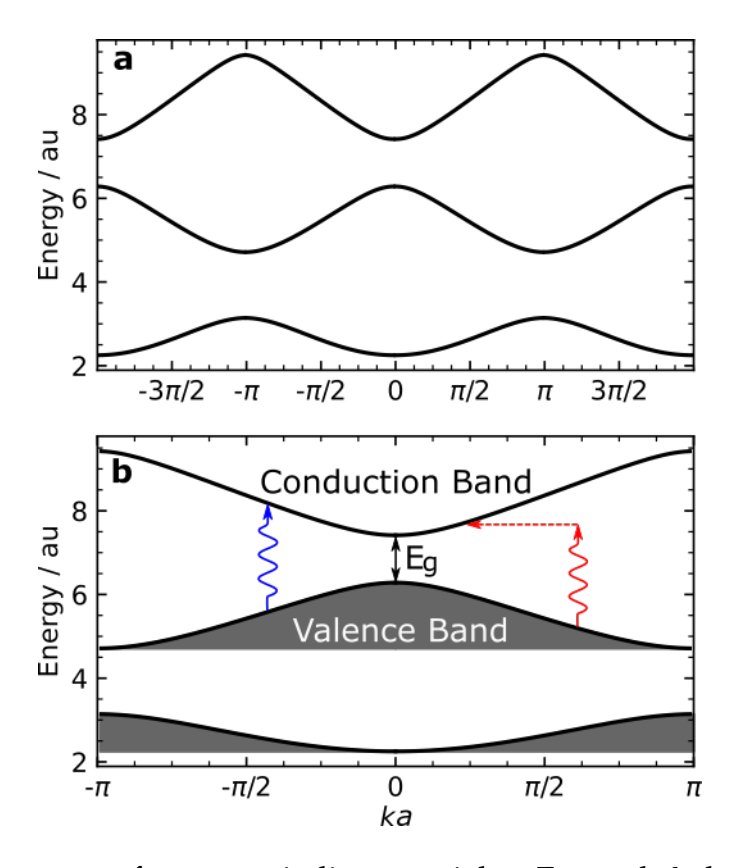


Figure 1.2: Band structure from a periodic potential. **a** For each k there is a discrete set of solutions to equation the central equation. **b** Because of the periodicity in k-space, it is sufficient to look at the zone $k \in [-\pi/a, \pi/a]$. Filled states are depicted by gray filled curves. Shown in blue is a direct transition, and in red an indirect transition.

is where all of the interesting physics takes place, the dispersion relation is as follows:

$$E(k) \approx \frac{\hbar^2 k^2}{2m^*} \tag{1.18}$$

with m^* the effective mass. This is directly analogous to the energy of a free particle, leading to the relation

$$m^* = m_e \left[\left. \frac{\partial^2 E}{\partial k^2} \right|_{BE} \right]^{-1} \tag{1.19}$$

Where $\frac{\partial^2 E}{\partial k^2}|_{BE}$ is the band curvature evaluated at the band edge. The concept of an effective mass is central to describing the transport and behaviour of charge carriers in these materials, as will be seen below.

1.1.4 Excitons

To understand the last important term needed to calculate the energy spectrum of a quantum dot, we must introduce the idea of holes as charge carriers. A hole is simply an electron vacancy. Holes exist in the valence band, since the electrons from which they are born reside there. Holes carry the effective mass associated with the valence band, and have a positive charge. The most important source of holes in the context of opto-electronics are those created through photo-excitation. Here a photon of sufficient energy is absorbed, exciting an electron from the valence band to the conduction band. This leaves a hole behind in the valence band and an electron in the conduction band.

After the creation of an electron-hole pair, they will feel each others charge, and undergo Coulomb attraction. The Hamiltonian of this Coulomb attraction in the effective mass approximation is directly analogous to the hydrogen atom, only the mass of the particles are replaced by effective masses, and the material permittivity replaces the permittivity of free space. This is written explicitly below:

$$\mathcal{H}_{coul} = \frac{-\hbar^2 e^2}{\epsilon \mu |r_e - r_h|} \tag{1.20}$$

With μ the reduced mass of the electron/hole pair, $\mu = m_e^* m_h^* / (m_e^* + m_h^*)$. In bulk semiconductors this leads to a series of states with energies $E_n = R_X / n^2$, where R_X is the binding energy.

$$R_X = \frac{\mu}{m_0 \epsilon_r^2} R_y \tag{1.21}$$

In equation 1.21 R_y is the usual hydrogen atom Rydberg energy of \sim 13.6 eV and ϵ_r the relative permittivity.

Since exciton binding energies are often on the order of 5-50 meV, they may be thermally depopulated and it is often necessary to cool samples to cryogenic temperatures for unambiguous observation of bulk excitons. However, as the lowest excited states,

they play an enormous role in semiconductor physics. To continue the analogy with the hydrogen atom, the excitonic radius can easily be calculated for a given crystal lattice, with a_0 the hydrogen atom Bohr radius of 0.53Å.

$$a_X = \frac{m_0 \epsilon_r}{\mu} a_0 \tag{1.22}$$

Two important classes of excitons exist in bulk semiconductors, based on their size:

- Small Frenkel excitons, whose Bohr radius is on the order of the unit cell size. These will be bound to a single lattice site and have limited mobility. They tend to be found in materials with low ϵ_r , where the lattice is ineffective at screening charge.
- Large Wannier-Mott excitons, whose Bohr radius is larger than the unit cell size. These tend to diffuse through the crystal, and can contribute to energy transport but not charge transport. They tend to be found in materials with high ϵ_r , where the lattice effectively screens excited charges.

1.1.5 Electron-phonon coupling in semiconductors

An electronic excitation will couple to the nuclear system, causing the lattice to move in order to accommodate the new charge distribution. If the coupling is weak, the lattice will have a small displacement and oscillate around a new equilibrium arrangement. The lattice oscillations, or phonons, are a delocalized phenomenon. If the coupling is strong, the lattice will rapidly rearrange itself in the immediate vicinity of the excited charge rapidly (with timescale on the order of the phonon period). This excited charge dressed with a distorted lattice is commonly referred to as a polaron, a localized quasiparticle. Polaron formation can be thought of as the solid-state equivalent of solvation in liquids.

In analogy with solvation, polaron formation is determined by crystal polarity. Polar, ionic crystals tend to couple strongly to excited charges. Less polar covalent crystals have weak coupling and tend to couple to the atomic lattice through delocalized coherent phonons.

Polaron formation has several effects on the excited charge, from increased mass[2] to improved transport properties[3]. The physics of this problem was first described by Herbert Fröhlich in 1954 [4] and expanded upon by Richard Feynman soon afterwards [5]. These two works state the problem in terms of a free electron coupled to a phonon gas, and solve the Hamiltonian for the lowest energy using variational methods. The size of the lattice distortion, and whether or not it is coherent, is of great interest to material scientists [6]. Lattice screening is thought to give rise to defect tolerance and impressive carrier mobility in halide-perovskite materials [7, 8]. The strength of this coupling is given by equation 1.23 [4].

$$\alpha_{e-ph} = \frac{e^2}{\hbar} \left(\frac{1}{\epsilon_{\infty}} - \frac{1}{\epsilon_0} \right) \sqrt{\frac{m^*}{2\hbar\omega_{LO}}}$$
 (1.23)

Where ϵ_{∞} and ϵ_{0} are the optical and static dielectric constants, m^{*} is the carriers reduced mass, and ω_{LO} is the LO phonon frequency. The most important term in equation 1.23 is the term in brackets, $(1/\epsilon_{\infty}-1/\epsilon_{0})$. This is the *lattice screening*, the difference in dielectric constants at fast, electronic frequencies and slow, nuclear frequencies. For example, the static and optical permittivities of GaAs are 13.1 [9] and 10.89[10], respectively, while CH₃NH₃PbI₃, the prototypical perovskite for photovoltaics, has a static dielectric constant of \approx 70, and an optical dielectric constant of \approx 8 [11]. In general, ionic compounds have significantly larger α_{e-ph} than covalently bound compounds, and a few examples are given in table 1.1.

Formation of a polaron also causes an increase to the carrier effective mass, as the carrier now has to displace the lattice as it moves around the crystal. The new effective

Covalent Material	α_{e-ph}	Ionic Material	α_{e-ph}
InAs	0.052	AgBr	1.53
GaAs	0.068	KI	2.50
ZnSe	0.43	$CsPbBr_3$	2.64(e ⁻) 2.76 (h ⁺)
CdS	0.53	$SrTiO_3$	3.77

Table 1.1: Frölich coupling constants for ionic and covalent crystals

mass is given by equation 1.24, in the limit of $\alpha \lesssim 10$ [4, 5].

$$m_p \approx m^* \left(1 + \frac{\alpha}{6} \right) \tag{1.24}$$

There is also a binding energy associated with the lattice displacement that favors the formation of a polaron; this is given by equation 1.25

$$\frac{\Delta E}{\hbar \omega_{LO}} \approx -\alpha - 0.0159\alpha^2 \tag{1.25}$$

Much like excitons, polarons can either be large or small. Large polarons span several lattice sites, and can be coherently transported. Small polarons are bound to a singular lattice site, and require thermal energy to hop from site to site. This produces a qualitative difference in thermal transport measurements, large polarons have decreased mobility with temperature while small polarons have increased mobility with temperature [3, 12]. This makes the polaron radius an important parameter, and is given by the following relation [4]:

$$l_p = \sqrt{\frac{\hbar}{2m^*\omega_{LO}}} \tag{1.26}$$

This formalism of electron-phonon coupling is important for describing the interaction of charge carriers with lattice potentials. The central parameter, α_{e-ph} , through the term $1/\epsilon_{\infty} - 1/\epsilon_{0}$, describes the ability of the slow lattice to screen the field of a fast electronic charge. Polar, ionic lattices do this very well. Covalent lattices much less so.

This has important consequences on the nature of excited state dynamics in these materials, as will be shown in chapter 5.

1.2 Quantum mechanics of a Semiconductor Nanocrystal

The quantum states of a semiconductor nanocrystal start with the bulk Bloch states developed above. This requires a consideration of the material band structure, i.e the band degeneracy, electron total angular momentum in those bands, and which bands contribute to which optical transitions. For optical transitions it is also necessary to consider electron-hole attraction in their mutual Coulomb potential. On top of this already rich structure, we dress the wavefunctions with an envelope function that arises from the boundary conditions of the nanocrystal. Before continuing with this development, it is useful to make a note about terminology. Many researchers reserve the term "nanocrystal" for any small crystal, with dimensions up to 1000 nm, reserving the term "quantum dot" for any crystal displaying a spectrum of quantum confined states. Here, we will treat the general case of a nanocrystal in developing theory, but in discussing experimental results I make an effort to distinguish the specific case of quantum dots where appropriate.

1.2.1 Particle in a Sphere

As the physical size of a semiconductor is reduced, the surface of that nanostructure becomes more and more important. The most important effect of a reduced size is quantum confinement. This is simply the problem of a particle in a box added to the effective mass approximation of the infinite crystal lattice. The problem of the particle in a rectangular box is a standard undergraduate quantum mechanics problem, and its precise statement and solution will not be described here. However, it is important to review the important aspects.

- For an infinite square well, the wavefunction goes to zero at the box boundaries.
- The n^{th} eigenstate state of a particle of mass m in a box of length L has energy E_n given by

$$E_n = \frac{\hbar^2 \pi^2}{2mL^2} n^2 \tag{1.27}$$

• The n^{th} level will have n-1 nodes in its' wavefunction.

For spherical nanocrystals, the problem must be re-framed in spherical coordinates (r, θ, ϕ) . The mathematics of this are developed below, for a nanocrystal sphere of radius R.

$$\mathcal{H}\psi = E\psi \tag{1.28}$$

$$\Rightarrow \left[-\frac{\hbar^2}{2m} \nabla^2 + V(r) \right] \psi(r, \theta, \phi) = E \psi(r, \theta, \phi)$$

$$V(r) = \begin{cases} 0 & r < R \\ \infty & r \ge R \end{cases}$$

$$(1.29)$$

Using spherical coordinates the angular momentum operator \hat{l} comes about naturally.

$$\hbar^2 \nabla^2 = \frac{\hbar^2}{r^2} \frac{\partial}{\partial r} \left(r^2 \frac{\partial}{\partial r} \right) - \frac{\hat{l}^2}{r^2}$$
 (1.30)

The solution to equation 1.29 can be found through separation of variables, i.e. we assume $\psi(r,\theta,\phi)=f(r)g(\theta,\phi)$. This yields the following form of equation 1.29.

$$\frac{\hat{l}^2}{2mr^2}g(\theta,\phi) = Eg(\theta,\phi) \tag{1.31}$$

$$\left[-\frac{\hbar^2}{2m} \left(\frac{1}{r^2} \frac{\partial}{\partial r} r \frac{\partial}{\partial r} - \frac{\hat{l}^2}{\hbar^2 r^2} \right) + V(r) \right] f(r) = Ef(r)$$
 (1.32)

The spherical harmonics, $Y_L^m(\theta,\phi)$, are solutions to the angular part (equation 1.31) and the spherical Bessel functions, $J_L(k_{n,L}r)$ are solutions to the radial part (equation 1.32). Quantization comes from the boundary conditions, $\psi(r=R)=0$. To satisfy this condition the radial function must go to zero at the nanocrystal boundary, $J_L(k_{n,l}R)=0$. All order of Bessel functions have multiple zeroes, and the quantization in n comes from which zero is used. To reflect this, we introduce the argument $k_{nL}=\alpha_{nL}/R$ where α_{nL} is the nth zero-crossing value of J_l . This idea is depicted in figure 1.3. Shown are the first 3 wavefunctions for L=0 in figure 1.3a and L=1 in figure 1.3b. These are very similar to hydrogen wavefunctions, in the number of nodes and the angular dependence of the wavefunction. The labelling of angular momentum states follows that of atomic orbitals, L=0,1,2 are s,p,d states with projections $m=-L,-L+1,\cdots,L-1,L$.

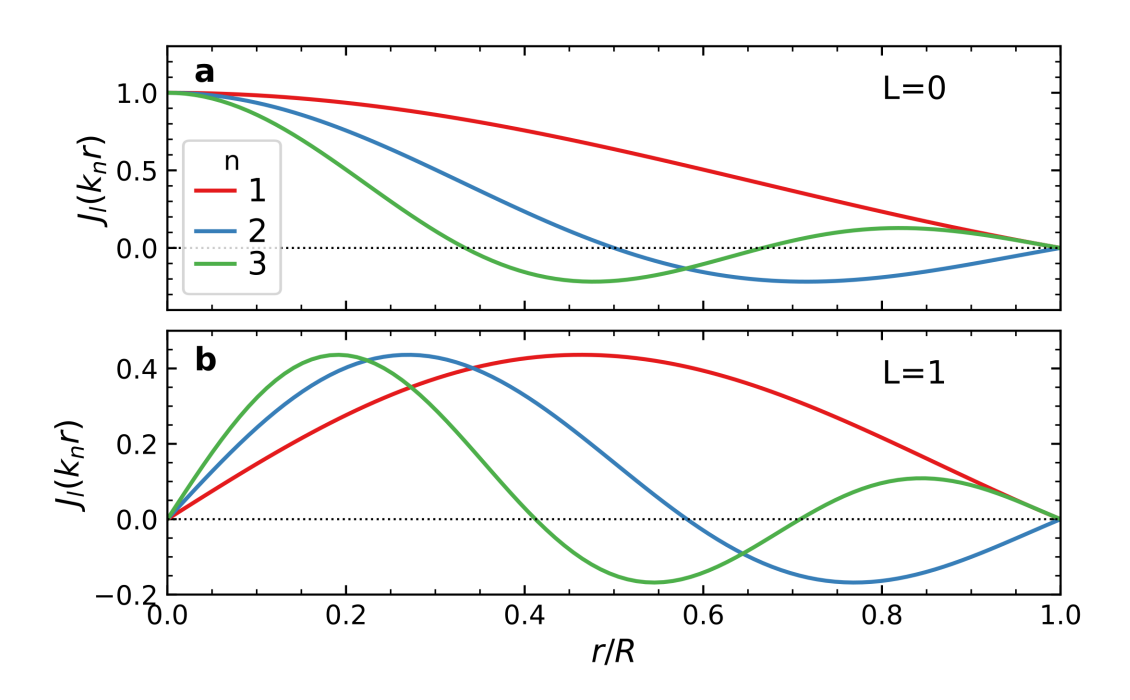


Figure 1.3: The first three radial wavefunctions for the particle in a sphere for both **a** L = 0, S states and **b** L = 1, P states.

The eigenenergies of this Hamiltonian are given by:

$$E_n = \frac{\hbar^2 \pi^2}{2mR^2} n^2 \tag{1.33}$$

The energies given by equation 1.33 are remarkably similar to those found in equation 1.27, the energies of a particle in a box. One finds the same dependence in n and the same $1/L^2$ dependence on the dimension of the confinement.

1.2.2 Covalent II-VI Quantum dots

One of the best platforms for quantum dots in terms of size-tuneability, stability, polydispersity, and ease of synthesis is CdSe. In fact, the entire family of II-VI semiconductors has been explored for research and application purposes. In terms of electronic structure all II-VI compounds are similar, and the development below can largely be applied across the family, with substitution of appropriate parameters (effective masses, band gaps, dielectric constants, etc.). PbSe is an important exception, relativistic effects of the Pb atom alter the ordering of atomic levels, and ultimately creates an 8-fold degenerate 1st exciton instead of the 2-fold degenerate case in other systems[13]. The approach below follows that of Efros and Rosen [14]. Bergman's *Handbook of Luminescent Semiconductor Materials* is another good reference that covers effective mass and band mixing approaches as well as atomistic calculations [15].

The band structure of II-VI compounds is the starting point. This is shown schematically in figure 1.4 **a**. There is only 1 low lying, two-fold spin degenerate conduction band composed of II-type s-orbitals. Conduction electrons thus have j=1/2. The valence band is more complicated; it is essentially composed of VI-type p-orbitals. Because the valence band electrons have $l \neq 0$, there is a spin-orbit effect in the valence band, creating a low energy, two-fold degenerate $p_{1/2}$ band and a higher energy, four

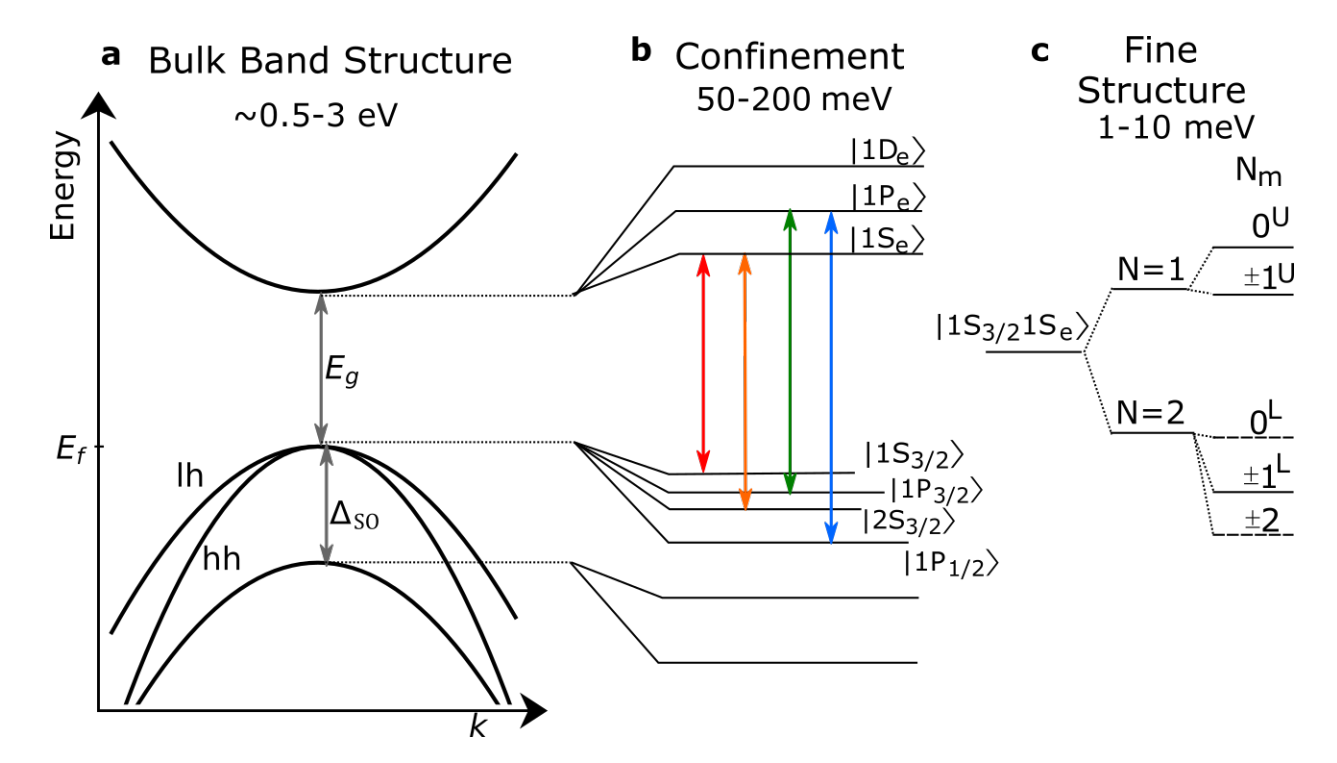


Figure 1.4: The energy levels of a II-VI quantum dot. **a** The bulk band structure has a single conduction band, and three valence bands. **b** The effect of strong quantum confinement is to increase the band gap and create a spectrum of discrete states. **c** The fine structure of a CdSe quantum dot.

fold degenerate $p_{3/2}$ band, with subscripts referring to electronic total angular momentum j=l+s. The lower energy band is labelled the split-off band, and is separated by the split-off energy, Δ_{SO} . For crystals with hexagonal or wurtzite symmetry, a particular spatial axis will have a different effective mass. The effect of this is to create two subbands from the higher j=3/2 valence band, a so-called heavy-hole and light-hole with different projections of j along the crystal axis.

This level of theory is sufficient to calculate the energy of the first optical transition. The initial theoretical work of Louis Brus is qualitatively correct and captures the important size-dependence of the excitonic states [16]. A more complete calculation, including band mixing, was performed by Efros and Rosen [14]. More modern methods can calculate levels from an atomistic, ab. initio approach for the smallest QDs [17]. In

the Brus model the energy of the lowest optical transition for a quantum dot of radius R is given as the sum of three terms:

$$E = E_g + E_{conf} + E_{coul} (1.34)$$

$$= E_g + \frac{\hbar^2 \pi^2}{2R^2} \left[\frac{1}{m_e^*} + \frac{1}{m_h^*} \right] - \frac{1.8e^2}{\epsilon R}$$
 (1.35)

Where E_g is the bulk energy gap. The Coulomb term is found by averaging over 1S wavefunctions in a variational approach. Notice that the confinement energy applies to both electrons and holes in equation 1.35.

The Efros and Rosen model is discussed below for strongly confined systems. Here the angular momentum of not only the band edge, but higher lying states as well, is taken into account and allows the assignment of optically bright and dark transitions.

The effect of confinement is to increase the band gap and create a series of discrete, well separated states from the continuum. This is applied to the conduction and each of the three valence bands. Because each band has a different effective mass, they are all affected differently by confinement. Notably, electrons have a smaller effective mass, and are thus more confined than holes. States are labelled by the quantum number of the particle in a sphere angular momentum and quantum number, with a subscript denoting the electronic band angular momentum projection. Since the conduction band has only j=1/2 angular momentum, the subscript e is used instead. The conduction band states are thus labelled $|nL_e\rangle$ and valence bands $|nL_{1/2}\rangle$ or $|nL_{3/2}\rangle$. This series of states is depicted in figure 1.4b. To assign and understand optical spectra, the next step is to apply optical selection rules. This produces the optical transitions shown in figure 1.4b. Only the four lowest allowed transitions are shown, at higher energies transitions tend to overlap and the spectra become too congested to confidently assign.

There is one more important aspect to discuss, and that is the fine structure of the lowest energy confined state. This is made up of a four-fold degenerate hole in the $|1S_{3/2}\rangle$

valence band and two-fold degenerate $|1S_e\rangle$ electron, for a total degeneracy of eight. This degeneracy is lifted by two interactions, an exchange interaction between electron and hole, and crystal field and shape asymmetry. The combination of these two effects yields the fine structure spectrum depicted in figure 1.4c; three doubly degenerate states and two singly degenerate states, with an optically passive ground state.

The exchange interaction between electrons and holes is due to Pauli exclusion effects and is proportional to electron-hole wavefunction overlap. Because of the significant confinement in quantum dots, this exchange interaction can be 100 times greater than in bulk materials. It is also a very size dependant energy splitting. The exchange interaction lifts the degeneracy between the N=2 and N=1 angular momentum states, where N is the total exciton angular momentum, $N=j_e+j_h$. This is analogous to exchange interactions splitting singlet and triplet levels in molecules.

The second important effect in the fine structure of the first excited state is crystal asymmetry. There are two contributions to this; intrinsic asymmetry due to the crystal, and shape asymmetry of the overall quantum dot. This has the effect of lifting degneracy on the projections along the crystal axis, and splits each N level into its N+1 projections along N_m . This is shown on the far right side of figure 1.4 c. Optically passive states are marked with dashed lines, and bright states with solid lines. The precise ordering of these levels will depend on the strengths of the two interactions, whether the crystal is prolate or oblate, and if there is cubic or hexagonal symmetry. However, the dark ground state or dark exciton exists for all sizes of quantum dot.

1.2.3 Ionically bound ABX₃ perovskite nanocrystals

Perovskite based materials, with general formula ABX_3 , are an exciting new class of materials in opto-electronic applications. The A cation can take many forms, both organic and inorganic. Common choices are methyl-ammonium, CH_3NH_3 , formadimium, $CH(NH_2)_2$,

or Cs. The metal atom occupies the B site. The most common metal used is Pb, but other options include Sn or Ge. The halide at X will be either chlorine, bromine, or iodine. The halide is the primary determinant of the material band edge, with larger atoms creating a larger lattice constant and a smaller bandgap. It is possible to mix halides, which opens up bandgap tuning across the visible spectrum. These materials take on a cubic, tetrahedral, or orthorhombic crystal structure, depending on lattice temperature and composition.

Since the discovery of high solar power conversion efficiency in simple, solution processed films of perovskite materials, [18] interest in these materials has exploded. Perovskites are particularly attractive from a material science point of view. Important effects, such as long carrier diffusion lengths [19, 20], Rashba splitting [21, 22], polaron formation [12, 2], defect tolerance [23], and the long lifetime of carriers in these materials have intrigued scientists for several years. These phenomena have important consequences on device performance, and are a wonderful playground for researchers in material science.

In 2015, a synthesis for colloidal nanocrystals of caesium lead halide perovskite nanocrystals was published [24]. These display quantum confinement for sufficiently small samples, and retain bandgap tuning through composition. This allows for bandgap tuning through both size and composition. The excitonic bohr radius for CsPb halides is amenable to size tuning, $a_X = 5$, 7, and 12 nm for X = Cl, Br, and I respectively.

Because of the ortho-rhombic crystal structure, these nanocrystals form cubes and rectangles instead of spheres. This has the consequence of forming a true three-dimensional particle in a box, as opposed to a particle in a sphere. Of particular interest, and what remains a largely open question, is the nature of the ground state exciton in per-ovskite nanocrystals. A good theoretical treatise has been done by Sercel et. al. [25]. The method for determining the energy structure in perovskite nanocrystals is similar to that for II-VI quantum dots; start with the bulk bands, apply an envelope quantum confine-

ment, then look at fine structure effects due to exchange interactions, shape asymmetry, and in the case of perovskites, spin-momentum coupling through the Rashba effect.

Following the development of Sercel et. al, the energy levels of CsPbBr₃ nanocrystals are described [25]. Because the room temperature phase of CsPbrBr₃ is tetragonal, there is a crystallographic axis with lower energy, leading to a 2 fold degenerate, p-type conduction band with j=1/2 and a two-fold degenerate s-type valence band, also with j=1/2. These states are described below:

$$|v_1\rangle = |S\rangle |+\rangle \tag{1.36}$$

$$|v_2\rangle = |S\rangle |-\rangle \tag{1.37}$$

$$|c_1\rangle = -\sin\theta |Z\rangle |+\rangle - \frac{\cos\theta |X\rangle + i\cos\theta |Y\rangle}{\sqrt{2}} |-\rangle$$
 (1.38)

$$|c_2\rangle = +\sin\theta |Z\rangle |-\rangle - \frac{\cos\theta |X\rangle - i\cos\theta |Y\rangle}{\sqrt{2}} |+\rangle$$
 (1.39)

Here $|X\rangle$, $|Y\rangle$, $|Z\rangle$ are Bloch functions along crystallographic axes, and θ is an angle that serves to mix these Bloch functions through spin-orbit interactions and the tetragonal crystal field in the conduction band. $|+\rangle$ and $|-\rangle$ are spin up and down states, respectively.

The coarse structure consists of the bulk bands dressed by the confinement potential and Coulomb attraction between electron and hole, as in figure 1.4 **b**. Fine structure corrections to this picture include a short-range exchange interaction, long-range exchange interaction, and crystal field splittings.

There are 4 exciton wavefunctions overall, made from combinations of valence band and conduction band wavefunctions. Together these form two states, a triplet state with $J = j_e + j_h = 1$ and a singlet state with J = 0. The short-range exchange interaction

is defined as a contact interaction between electron and hole, described by a δ -function in electron and hole positions.

$$\mathcal{H}^{SR} = \Omega C M^{SR}(\theta) \delta(\mathbf{r_e} - \mathbf{r_h}) \tag{1.40}$$

In equation 1.40, Ω is the unit cell volume, C is an exchange constant, and $M^{SR}(\theta)$ encodes the symmetry of the Bloch functions.

$$M^{SR}(\theta) = \begin{pmatrix} \cos^2 \theta & 0 & 0 & 0\\ 0 & \sin^2 \theta & \sin^2 \theta & 0\\ 0 & \sin^2 \theta & \sin^2 \theta & 0\\ 0 & 0 & 0 & \cos^2 \theta \end{pmatrix}$$
(1.41)

The effect of the short-range exchange interaction is to split the four degenerate states into a triplet and a singlet state. In a cubic lattice the triplet isn't split, in a tetragonal lattice it is split into a doublet and a singlet, and in ortho-rhombic crystals the triplet is fully split. In all cases the singlet state is below the triplet state and this state is dark. Further corrections in taking into account long-range exchange interactions and the effect of the dielectric nanocrystal barrier are taken into account by Sercel et. al. [25], but these do not change the order of levels, only their relative spacing.

The most important new effect that must be taken into account is the Rashba effect. The Rashba effect describes a spin-momentum coupling that is due to inversion-breaking symmetry, such as broken symmetry along the \hat{z} axis in a tetragonal crystal lattice. This leads to a crystal field along z, E_z . A charge moving in this electric field experiences a magnetic field B perpendicular and proportional to its' velocity \mathbf{v} .

$$\mathbf{B} = -(\mathbf{v} \times \mathbf{E})/c^2 \tag{1.42}$$

This magnetic field creates a spin-orbit effect type of Hamiltonian. The mathematics of this are shown below.

$$\mathcal{H}_{SO} = -\mu \cdot \mathbf{B} \tag{1.43}$$

$$=\frac{g\mu_B}{2c^2}(\mathbf{v}\times\mathbf{E})\cdot\sigma\tag{1.44}$$

$$\Rightarrow \mathcal{H}_R = \alpha_R(\sigma \times \mathbf{p}) \tag{1.45}$$

Where $\alpha_R = -g\mu_B E_0/(2mc^2)$ is the Rashba coefficient, σ is a spin matrix, \mathbf{p} is charge momentum, $g \approx 2$ is the electron spin g-factor and μ_B is the Bohr magneton. This hamiltonian leads to energy shifts of the form

$$\Delta E^R = -2A\mathcal{E}_R(\sigma_x^e \sigma_x^h + \sigma_y^e \sigma_y^h) \tag{1.46}$$

Here A is a coefficient reflecting exciton motion and \mathcal{E}_R is the Rashba energy, $\mathcal{E}_R = \alpha_e \alpha_h \mu/\hbar^2$. The calculations presented by Efros et. al. show that the Rashba effect actually reverses the ordering of states introduced by exchange interaction for nanocrystals above a certain size, leading to a bright triplet state as the ground state. Below a certain size the ground state may be a dark exciton. Experimental evidence for the ordering of these states is found through single crystal cryo-PL and magneto-optical studies [26, 27, 28]. With application of a magnetic field the triplet / singlet basis is broken, and the singlet state takes on some triplet character, making it partially bright. Interestingly, prominent reports have produced a variety of results, with magneto-optical measurements showing a dark-exciton as the ground state [26, 27] and single crystal PL showing a bright triplet as the ground state [28], while four-wave mixing has shown very different dephasing rates for one of the triplet states, possibly due to rapid relaxation to an intermediate dark state [29].

Bibliography

- [1] Kittel, C. Introduction to Solid State Physics, 8th ed.; John Wiley & Sons, Inc, 2005.
- [2] Puppin, M.; et al. *Physical Review Letters* **2020**, 124, 206402.
- [3] Yi, H. T.; Wu, X.; Zhu, X.; Podzorov, V. Advanced Materials 2016, 28, 6509–6514.
- [4] Fröhlich, H. Advances in Physics 1954, 3, 325–361.
- [5] Feynman, R. P. Physical Review **1955**, 97, 660–665.
- [6] Miyata, K.; Meggiolaro, D.; Tuan Trinh, M.; Joshi, P. P.; Mosconi, E.; Jones, S. C.; De Angelis, F.; Zhu, X. Y. *Science Advances* **2017**, 3.
- [7] Valverde-Chávez, D. A.; Ponseca, C. S.; Stoumpos, C. C.; Yartsev, A.; Kanatzidis, M. G.; Sundström, V.; Cooke, D. G. Energy and Environmental Science 2015, 8, 3700–3707.
- [8] Yettapu, G. R.; Talukdar, D.; Sarkar, S.; Swarnkar, A.; Nag, A.; Ghosh, P.; Mandal, P. *Nano Letters* **2016**, *16*, 4838–4848.
- [9] Strzalkowski, I.; Joshi, S.; Crowell, C. R. Applied Physics Letters 1976, 28, 350–352.
- [10] McKitterick, J. B. *Physical Review B* **1983**, 28, 7384–7386.
- [11] Lin, Q.; Armin, A.; Chandra, R.; Nagiri, R.; Burn, P. L.; Meredith, P. *Nature Photonics* **2015**, 9.

- [12] Miyata, K.; Atallah, T. L.; Zhu, X. Y.; Lead halide perovskites: Crystal-liquid duality, phonon glass electron crystals, and large polaron formation; 2017. http://advances.sciencemag.org/lookup/doi/10.1126/sciadv.1701469.
- [13] An, J. M.; Franceschetti, A.; Dudiy, S. V.; Zunger, A. Nano Letters 2006, 6, 2728–2735.
- [14] Efros, A. L.; Rosen, M. Annual Review of Materials Science 2000, 30, 475–521.
- [15] Bergman, L. Handbook of Luminescent Semiconductor Materials 2011, 279–305.
- [16] Brus, L. IEEE Journal of Quantum Electronics **1986**, 22, 1909–1914.
- [17] Long, R.; Prezhdo, O. V. 2015.
- [18] Kojima, A.; Teshima, K.; Shirai, Y.; Miyasaka, T. Journal of the American Chemical Society **2009**, 131, 6050–6051.
- [19] Stranks, S. D.; Eperon, G. E.; Grancini, G.; Menelaou, C.; Alcocer, M. J.; Leijtens, T.; Herz, L. M.; Petrozza, A.; Snaith, H. J. *Science* **2013**, *342*, 341–344.
- [20] Xing, G.; Mathews, N.; Lim, S. S.; Lam, Y. M.; Mhaisalkar, S.; Sum, T. C. *Science* **2013**, 342, 346–347.
- [21] Todd, S. B.; Riley, D. B.; Binai-Motlagh, A.; Clegg, C.; Ramachandran, A.; March, S. A.; Hoffman, J. M.; Hill, I. G.; Stoumpos, C. C.; Kanatzidis, M. G.; Yu, Z. G.; Hall, K. C. APL Materials 2019, 7.
- [22] Isarov, M.; Tan, L. Z.; Bodnarchuk, M. I.; Kovalenko, M. V.; Rappe, A. M.; Lifshitz, E. *Nano Letters* **2017**, *17*, 5020–5026.
- [23] Kang, J.; Wang, L. W. Journal of Physical Chemistry Letters 2017, 8, 489–493.
- [24] Protesescu, L.; Yakunin, S.; Bodnarchuk, M. I.; Krieg, F.; Caputo, R.; Hendon, C. H.; Yang, R. X.; Walsh, A.; Kovalenko, M. V. *Nano Letters* **2015**, *15*, 3692–3696.

- [25] Sercel, P. C.; Lyons, J. L.; Wickramaratne, D.; Vaxenburg, R.; Bernstein, N.; Efros, A. L. Nano Letters 2019, 19, 4068–4077.
- [26] Mitioglu, A. A.; Biadala, L.; Bayer, M.; Yakovlev, D. R.; Christianen, P. C. M.; Rogge, T.; Lhuillier, E.; Canneson, D.; Ballottin, M. V.; Shornikova, E. V. Nano Letters 2017, 17, 6177–6183.
- [27] Tamarat, P.; Bodnarchuk, M. I.; Trebbia, J.-B.; Erni, R.; Kovalenko, M. V.; Even, J.; Lounis, B. *Nature Materials* **2019**.
- [28] Becker, M. A.; et al. Nature 2018, 553, 189–193.
- [29] Liu, A.; Almeida, D. B.; Bonato, L. G.; Nagamine, G.; Zagonel, L. F.; Nogueira, A. F.; Padilha, L. A.; Cundiff, S. T. **2020**, 2–7.

Chapter 2

Pump-probe spectroscopy

Ultrafast spectroscopy is a broad and productive field. The techniques of ultrafast spectroscopy have answered fundamental questions about atomic physics through high harmonic generation [1, 2, 3], observed chemical reactions proceed in real time [4], and answered questions about the role and dynamics of the solvent[5, 6]. Various methods have coupled ultrashort time resolution to real-space nanometer scale spatial resolution, either through coupling ultrafast THz pulses to an STM tip [7], through near field microscopy [8], atomic force microscopy [9] or even by observing photo-electron products [10]. High spatial resolution can also be obtained in k-space through either ultrafast X-ray [11] or electron diffraction [12, 13], allowing the observation of collective changes in crystal phase or scattering potential with ultrafast temporal resolution. All of these ultrafast techniques rely on the concept of pump-probe spectroscopy, a two pulse experiment where one pulse puts the system in an excited state, and a second pulse probes the excited state. By controlling the delay between pump and probe pulses, the evolution of the excited state is tracked through time. The power of this type of experiment is that temporal resolution is no longer limited by the slow response of an electronic detector, it is now limited by the duration of the pump and probe pulses.

The work presented here is focused on optical pump, optical probe spectroscopy of nanomaterials. This chapter will focus on the experimental details of optical pump-probe spectroscopies, and the particular implementation in the Kambhampati lab. The various signals and insights gained from ultrafast pump-probe spectroscopy of nanocrystals will also be discussed, including hot carrier cooling, gain characterization, and Auger recombination. Electron-phonon coupling signals are discussed in chapter 3.

2.1 Generating short pulses

As mentioned above, the ultimate resolution limit in a pump-probe experiment is pulse duration. This always starts with what is called a *mode-locked* laser, although other approaches using fast phase modulation are being explored [14, 15]. To understand the workings of a mode-locked laser, a brief explanation of the operating frequencies of a laser is necessary. The cavity mirrors of a laser of length L impose boundary conditions on the electric field. This means that any electric field must go to zero at the cavity walls E(x=0)=E(x=L)=0, forcing the electromagnetic wavelengths λ_m to follow the condition $\lambda_m=L/2m$ or $\nu_m=\frac{2c}{L}m$. If the laser cavity is circular instead of linear, the boundary conditions are E(x)=E(x+L), forcing the wavelengths to follow the relation $\lambda_m=L/m$. For linear cavities, the boundary conditions translate into modes spaced by $\delta_{nu}=c/2L$ in frequency, which is generally anywhere between a few MHz to a few GHz. The λ_m are the longitudinal modes of a laser. The actual wavelengths that will lase must have net amplification after one round trip of the cavity, i.e have gain provided by two passes through the active medium 2G greater than loss by reflection R at the exit mirror, 2GR>1.

Generally there is competition between longitudinal modes, with the laser perhaps hopping between a few neighboring modes if it's designed for power, or remaining fixed on a single mode if the laser is designed for high-precision frequency applications. This is termed continuous-wave or cw operation, where only one or a few modes are active. Mode-locked lasers operate in a different way, where many longitudinal modes are forced to operate at once. If many modes operate together in phase, they will produce a short pulse that circulates in the cavity. This short pulse has a high peak intensity compared to cw operation, so the trick to making a mode-locked laser work is to create loss for low peak-power operation relative to high peak-power operation. This can be done passively, through a saturable absorber as in many fiber lasers [16] today or dyelasers [17] in the past. Saturable absorbs absorb well under low fluence, but become more transparent under higher fluence [18]. The difference in absorption may be less than 1%, but over many cavity round-trips this is sufficient to favor mode-locked over cw operation. Another passive method, used in Ti:Sapphire lasers, is Kerr-lens mode-locking [19]. In Kerr-lens mode-locking the ultrafast pulse instantaneously creates a lens in the active medium through nonlinear optical interactions. This lens produces a mode-locked beam with a smaller size then the cw beam. By introducing a slit that blocks the cw beam and passes the mode-locked beam, mode-locked operation is favored.

Active mode-locking usually uses an electro-optic or acousto-optic crystal in the laser cavity to create amplitude modulation or frequency modulation. By driving these devices at the cavity-mode spacing $\delta\nu$, modes that are in phase with the driving frequency will be amplified over those that are out of phase, creating a phase relation between modes that leads to short pulses. Active-mode locking adds complexity and potential sources of instability, and is not often used.

The duration of the pulse emitted by a mode-locked laser is limited by the width of the emitted spectrum. The broader the spectrum, or the more longitudinal modes that contribute, the shorter the pulse can be. This is shown in figure 2.1. For a gain system

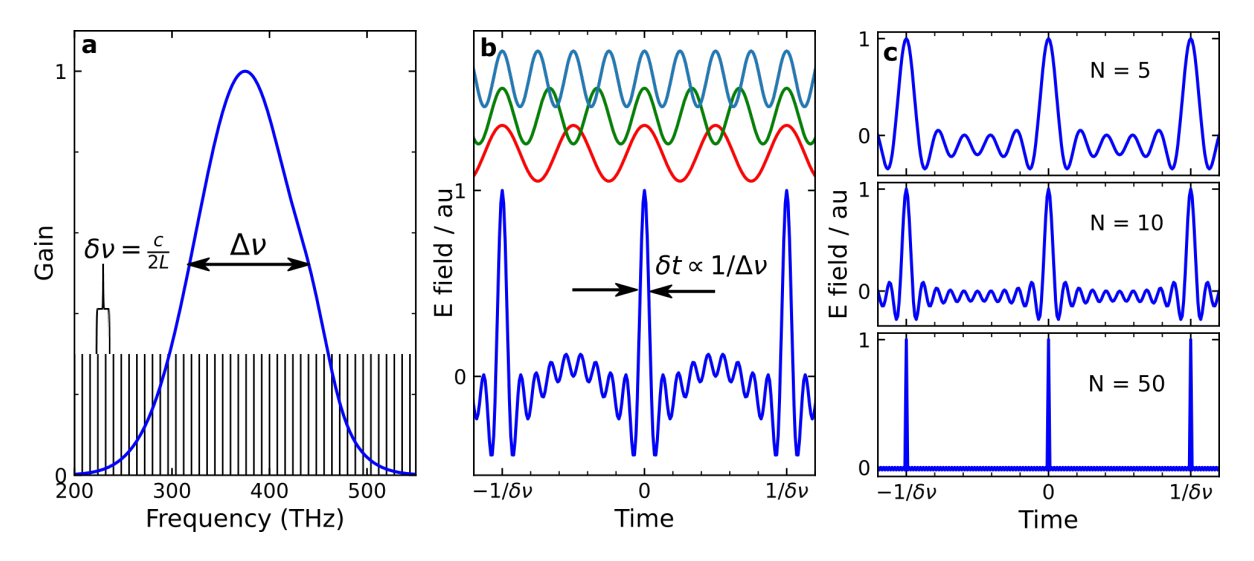


Figure 2.1: Longitudinal modes and pulse duration in a mode-locked laser. **a** A broad gain spectrum (blue curve) can support many modes (black sticks). **b** The addition of several modes in phase create a short pulse. **c** As the number of modes in phase increases, pulses become shorter and sharper.

such as that shown in figure 2.1a, longitudinal modes are depicted as black sticks and the gain spectrum as the blue curve. The modes are separated by $\delta\nu=c/2L$. Any mode that lies below the blue curve has gain greater than loss and could contribute to mode-locking. The total spectral width is denoted $\Delta\nu$. The mode-locked pulse is composed of many longitudinal modes operating at once, as shown in figure 2.1b. Here 10 modes add in phase, creating a pulse at t=0 and $t=\pm 1/\delta\nu$. As the number of modes contributing in phase grows, the pulse becomes shorter and sharper, as shown in figure 2.1c. As a point of reference, Ti:Sapphire lasers can have $\sim 10^6$ modes over 50 THz of bandwidth lasing at once, producing pulses ~ 10 fs long.

Mode-locked lasers produce a train of ultrashort pulses separated by the cavity round trip time $1/\delta\nu$, typically around 10 ns (100 MHz) for Ti:Sapphire systems and as little as 1 ns (1 GHz) for fibre based systems. This pulse train provides a convenient clock frequency that can be actively stabilised through the optical cavity length L with a simple piezoelectric. Locking this clock frequency will simultaneously lock the RF repeti-

tion rate $\delta\nu$ and the optical frequency ν of the laser, providing a convenient link between the RF and optical frequency of the longitudinal modes. This has made ultrafast lasers a workhorse of ultra-precise time/frequency metrology. [20].

2.1.1 Chirped pulse amplification

Through a technique called chirped pulse amplification, extraordinary laser pulse peak powers can be obtained [21]. The impact of this amplification technology is tremendous, and Gérard Mourou and Donna Strickland were awarded the 2018 Nobel prize in Physics for its discovery. In chirped-pulse amplification, the mode-locked pulse is stretched in time, yielding a longer pulse with the same total energy but much lower peak power. This can then be safely amplified to very large pulse energies without damage to the amplifier system due to high peak intensities. By then re-compressing the pulse, the ultrashort pulse is recovered. This technique has yielded the highest peak powers ever obtained, on the order of \sim 10 Petawatts [22]. For comparison, the United States generated an average of \sim 0.0034 PW over 2018 from all primary energy sources [23]. These extremely intense fields can be used as a particle accelerator, accelerating electrons to 100s of MeV of energy in the space of just a few millimeters [24], and hold the promise of new physics in these extraordinary fields.

Chirped pulse amplifiers are powerful tools for spectroscopy. With the high peak powers available in off the shelf systems, wavelength tuning and continuum generation through non-linear interaction is very efficient. It is quite simple to make a white-light continuum through self-phase modulation (SPM) in transparent media. Here, the field intensity alters the refractive index of the medium, leading to a phase modulation of the pulse with duration on the order of the pulse duration. Phase modulation leads to the cre-

ation of new frequencies, which can span the entire visible range. To create high-power, narrow band pulses another non-linear process is required; optical parametric amplification. Here, a white light seed pulse is generated through SPM. This seed is then mixed with a pump pulse to create signal and idler beams, through the process $\omega_p \to \omega_i + \omega_s$, where ω_p,ω_s , and ω_i are the frequencies of the pump, signal, and idler beams, respectively. For Ti:Sapphire systems operating near 800 nm, parametric amplification can generate IR wavelengths in the region 1 - 3 μ m. To obtain visible wavelengths, the signal and idler can be frequency doubled or mixed with the pump beam. Optical Parametric Amplifiers can produce wavelengths spanning the UV to the Far IR. There are also other approaches for creating broadband pulses that will be discussed in chapter 6. The combination of high power and short pulses are what makes chirped pulse amplification so important to ultrafast spectroscopy.

2.1.2 Describing pulse phase

In order to understand pulse compression and phase relations, a few terms should be introduced. The Fourier limit of a pulse occurs when all Fourier components, or frequencies, oscillate in phase. This phase is central to describing pulses, and is often described in the frequency domain. It is convenient to expand the spectral phase in a Taylor series about the pulse central frequency.

$$\phi(\omega) = \phi_0 + \frac{d\phi}{d\omega}\Big|_{\omega_0} (\omega - \omega_0) + \frac{1}{2} \frac{d^2\phi}{d\omega^2}\Big|_{\omega_0} (\omega - \omega_0)^2 + \dots$$
 (2.1)

In equation 2.1 ϕ_0 is called the carrier-envelope phase (CEP). This is because it relates the phase of the high frequency optical wave to the envelope, $\phi_0 = 0$ (π) means that at the peak of the envelope the field is at a maximum (minimum). For $\phi_0 = \pm \pi/2$ the field is zero where the envelope is maximum. The ϕ_0 term is important in few-cycle pulses, be-

cause the envelope function might change significantly over one optical period. The CEP is also important in phase-cycling applications and interferometry. $d\phi/d\omega$ is the group velocity of the pulse, and is related to the velocity of the pulse envelope in the medium. $d\phi/d\omega$ does not change the pulse width, only the pulse arrival time. The most important term for pulse compression is $d^2\phi/d\omega^2$, which is the group velocity dispersion (GVD), or more commonly, chirp. Transmission through most windows, prisms, crystals will impart positive GVD on a pulse, and red wavelengths will travel faster than blue wavelengths, causing the pulse to stretch in time. Pulse compression refers to undoing this stretching in a controlled manner, and can be done through prisms, gratings, or pulse shapers. Prisms work well for small amounts of chirp, and gratings work well for larger amounts of chirp and have higher damage thresholds. The most precise method of phase control is the use of pulse shapers. These devices apply an amplitude and phase mask to the electric field of the pulse, allowing for arbitrary phase control over all terms in equation 2.1.

2.1.3 Measuring ultrafast pulses

To measure an ultrafast light pulse, conventional electronics simply will not do. The fastest response times of photodiodes are in the 100s of picoseconds range, roughly 1000 times too slow. For ultrafast pulse measurement generally, optical gating techniques must be used. All of these techniques exploit optical nonlinearities with instantaneous response times, such as sum-frequency generation (SFG), or Kerr effects that modulate the material refractive index. These are shown in figure 2.2. The simplest implementation of optical gating is intensity auto-correlation. Here an input pulse is split into two copies, one goes through a variable delay with either a delay stage or wedge pair, and the pulses are recombined in a non-linear crystal such as BBO. When the pulses overlap in time, they can

interact to form a third pulse through SFG. For a Gaussian input pulse given by:

$$E(t) = E_0 e^{-i\omega t} \exp\left(-\frac{t^2}{2\sigma^2}\right) + c.c.$$
 (2.2)

$$I_0(t) \propto E(t)E^*(t) \tag{2.3}$$

$$=|E_0|^2 e^{-t^2/\sigma^2} (2.4)$$

the SFG pulse will be as follows:

$$E_{SFG}(t) \propto \chi^{(2)} E^2(t) \tag{2.5}$$

$$= \chi^{(2)} E_0^2 \left(e^{-2i\omega t} e^{-t^2/\sigma^2} + c.c. \right)$$
 (2.6)

Where $\chi^{(2)}$ is a second order non-linear susceptibility. This electric field has twice the frequency of the fundamental, and is often referred to as a special case of SFG, second-harmonic generation. When one pulse copy is delayed by τ with respect to the other, the electric field is instead a convolution of those pulses.

$$E_{SFG}(t,\tau) \propto \chi^{(2)} \int_{-\infty}^{\infty} E_1(t) E_2(t-\tau') dt'$$
(2.7)

$$\Rightarrow I_{SFG}(\tau) \propto \chi^2 \int_{-\infty}^{\infty} |E(t)E(t-\tau)|^2 dt$$
 (2.8)

$$= \int_{-\infty}^{\infty} I(t)I(t-\tau)dt \tag{2.9}$$

Substituting in our Gaussian pulse given by equation 2.4 and performing the integration by switching to Fourier space, we find the form of the detected intensity trace.

$$I_{SFG}(\tau) = |E_0|^4 e^{-\tau^2/\sqrt{2}\sigma^2}$$
 (2.10)

(2.11)

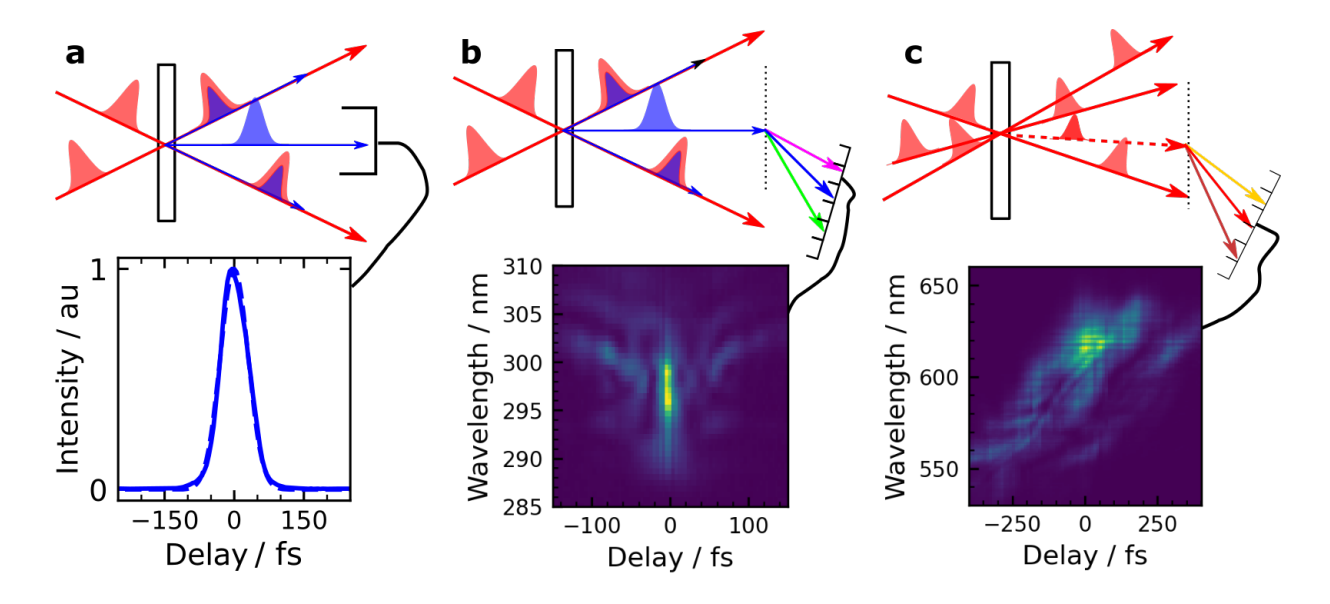


Figure 2.2: Three ways to measure an ultrafast pulse. **a** two pulses are mixed in a $\chi^{(2)}$ medium. When they overlap in time and space an SFG signal is produced that traces the pulse auto-correlation. Here a simple, nearl-transform limited pulse is measured. **b** By spectrally dispersing the auto-correlated signal in SFG-FROG, pulse reconstruction becomes possible but the resulting trace is non-intuitive, even for a well-compressed pulse as shown here. **c** TG-FROG, which relies on a $\chi^{(3)}$ process, yields intuitive traces and is not bandwidth limited. Here a long, complicated pulse is accurately measured.

The auto-correlation trace is broader than the fundamental pulse given by equation 2.4 by a deconvolution factor of $\sqrt{2}$. Another common pulse shape is given by sech², and this has a deconvolution factor of 1.54.

Intensity auto-correlation works best for simple pulses which require only quadratic spectral phase correction. The retrieved pulse width can be compared to a Fourier-limited width, and if they agree then the pulse is fully compressed. However, it is also possible to use SFG to measure complex pulses. By mixing a well-characterized pulse with an unknown, complex one, the time envelope of the more complex pulse can be retrieved. This is referred to as cross-correlation, and is shown in figure 2.3. Cross-correlation in the Kambhampati lab is used to characterize the GVD of the white-light probe. By selecting one part of the white light spectrum and mixing it with the 800 nm fundamental, the sum-

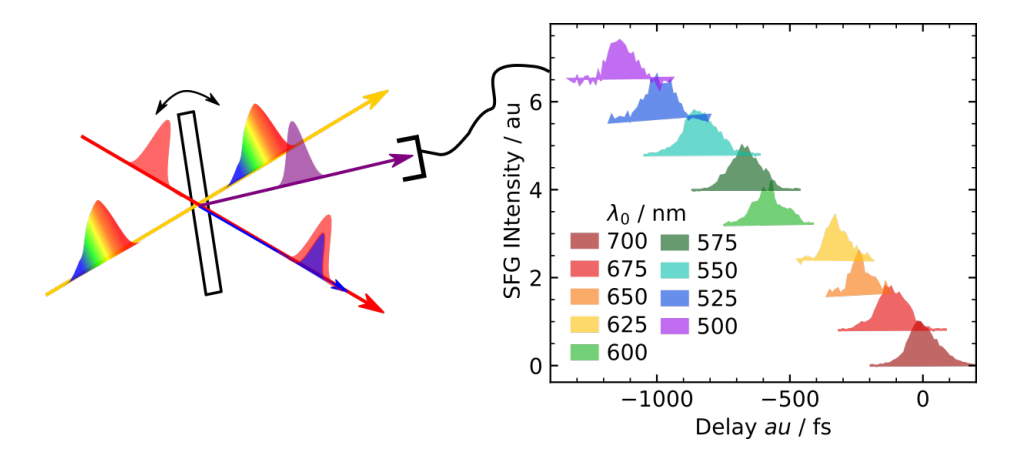


Figure 2.3: Cross-correlation of a complicated pulse with a simple pulse, allowing for reconstruction of the complicated pulse. Here a white light pulse spanning \sim 480-750 nm and > 1100 fs long has it's chirp accurately measured.

frequency is generated. By scanning the delay the cross-correlation between fundamental and a portion of the white-light is measured. By scanning the part of the white-light spectrum that is mixed the relative arrival time of each frequency is retrieved. This is a direct measure of the GVD.

Pulse characterization through auto-correlation is the simplest to implement, but does not have the information required to fully reconstruct the pulse. Furthermore, examination of an auto-correlation trace, as in figure 2.2a, is not intuitive.

In order to fully reconstruct the phase profile of the pulse, it is necessary to disperse the gated signal using a spectrometer. This is termed Frequency-resolved optical gating, or FROG. There are many flavors of FROG, based on the non-linear process used to gate the optical signal. For full details see [25]. For SFG-FROG the signal is simply:

$$I_{SFG}(\omega,\tau) = \left| \int_{-\infty}^{\infty} E_{SFG}(t,\tau) e^{-i\omega t} dt \right|^{2}$$
 (2.12)

These SFG techniques are very sensitive, since they rely on $\chi^{(2)}$ nonlinear processes. However there are significant drawbacks; using SFG requires phase-matching be-

tween the fundamental and signal wavelengths. For very short, very broadband pulses it can be difficult to achieve phase-matching over the entire bandwidth of the pulse. Thin crystals can be used, but this will reduce signal. Another drawback is the difficulty in reading the produced FROG-traces. As can be seen in figure 2.2b the trace has some phase that needs to be compensated, but it isn't clear how to do this.

Another FROG-based technique that is widely used is transient-grating, or TG-FROG. Here a nonlinear Kerr effect is used to measure the pulse. The Kerr effect describes how an optical pulse will alter the refractive index of a medium, $n(\vec{r},t) = n_0 + n_2 I(\vec{r},t)$. The non-linear index n_2 arises from $\chi^{(3)}$ effects. The Kerr effect has important consequences both the spatial and temporal dimensions. Spatially, a Gaussian beam spatially modulates the index, creating a lens that leads to self-focusing. This can very quickly lead to catastrophic destruction of optical components. When the pulse has rapid temporal variations, which is almost always the case in ultrafast spectroscopy, self-phase modulation can occur. This is the source of the white-light continuum used in many pump-probe experiments. In TG-FROG the Kerr effect is exploited to create a phase grating for pulse measurement. This requires three copies of the pulse to be created. These three pulses are focused to the same spot in some transparent medium, where two of the pulses create an index of refraction grating through a $\chi^{(3)}$ Kerr effect. For two pulses travelling in the x-z plane, this looks like the following:

$$\Delta n(x) = n_2 I(x) = n_2 \left| E_0 e^{i(k_z z + k_x x)} + E_0 e^{i(k_z z - k_x x)} \right|^2$$
(2.13)

$$=2n_2E_0^2(1+\cos(2k_xx))$$
(2.14)

The third pulse is delayed relative to these two; If it arrives at the same time it will be diffracted off of this transient grating in the direction $k_s = k_1 - k_2 + k_3$. Detecting this signal as a function of delay and wavelength produces the trace shown in figure 2.2c.

Mathematically this signal is given by equation 2.15 - 2.17.

$$E_{TG}(\omega,\tau) = \int_{-\infty}^{\infty} E^*(t)E(t)E(t-\tau)e^{-i\omega t}dt$$
 (2.15)

$$= \int_{-\infty}^{\infty} I(t)E(t-\tau)e^{-i\omega t}dt$$
 (2.16)

$$\Rightarrow S_{TG}(\omega, \tau) \propto \left| \int_{-\infty}^{\infty} I(t)E(t - \tau)e^{-i\omega t}dt \right|^{2}$$
 (2.17)

This technique has several advantages. One is readability; TG-FROG traces can roughly be read like musical scores, it is a plot of what frequencies are played at what time. This allows for easy identification of how much chirp to add or subtract, and whether or not here is any higher order phase distortions in the pulse. Because there is no frequency mixing in TG-FROG, and the $\chi^{(3)}$ there is no need for phase-matching considerations. This allows TG-FROG to measure extremely short pulses across a large spectral range. The TG-FROG trace shown in figure 2.2c has a clear slope, this indicates quadratic spectral phase. The pulse measured in figure 2.2c is the direct output of an OPA driven hollow core fibre, with over 100 nm of spectral width and a complicated temporal shape. TG-FROG is able to characterize this without loss.

2.2 Pump-probe spectroscopy of semiconductor nanocrystals

Ultrafast spectroscopy famously began with the direct observation of the transition state in the dissociation of iodine cyanide; ICN \rightarrow I + CN [4]. This work earned Ahmed Zewail the 1999 Nobel prize in chemistry. Since those experiments, ultrafast spectroscopy has since extended to cover nearly the entire electromagnetic spectrum, from THz to X-rays. Advanced techniques, such as mulitdimensional spectroscopy [26, 27], fluorescence upconversion[28] and ultrafast Raman[29] have been developed and used to an-

swer unique questions. Below, the common premise of pump-probe spectroscopy is explained, followed by its specific application in the Kambhampati lab.

2.2.1 State-resolved pump-probe spectroscopy

Pump-probe spectroscopy is a general term that applies to most of ultrafast science. Pumpprobe refers to the method of using two pulses to create temporal resolution. In pumpprobe spectroscopy, the fastest processes that can be measured are not limited by detector resolution, but rather pulse duration. One pulse, the pump, excites the sample. After a controlled delay, a second pulse probes the excited state. Delays can be imparted in a number of ways, often with a retro-reflector mounted to a mechanical delay stage. For more precise control a pair of glass wedges can be used, as one wedge is moved closer/further to the other the beam passes through more or less glass, creating very fine control over pulse delay. Another method is through pulse shaping techniques. By controlling the index of refraction in a material, a pulse can be delayed or advanced. The spectral phase can be altered to compress the pulse or look at effects due to pulse chirp [30]. Pulse shaping is commonly done in acousto-optic crystals in both collinear [31] and transverse geometries [32] and in liquid crystals [33]. Mechanical delay stages have the greatest range of delays, from \sim 1 fs to \sim 1 ns, but cannot achieve the same precision as a pair of glass wedges. Pulse shapers have the added benefit of pulse shaping, e.g. removing phase distortions to create transform-limited pulses, create trains of pulses or perform phase cycling and chopping all within the same device. The disadvantage is that these devices can only create delays up to \sim 1 ps. Also, pulse shapers are expensive and have relatively low damage thresholds. Compared to retroreflectors, they also have a more limited bandwidth.

One implementation of pump-probe spectroscopy that is very powerful for teasing out the effects of the initial state is state-resolved pump-probe spectroscopy (SRPP).

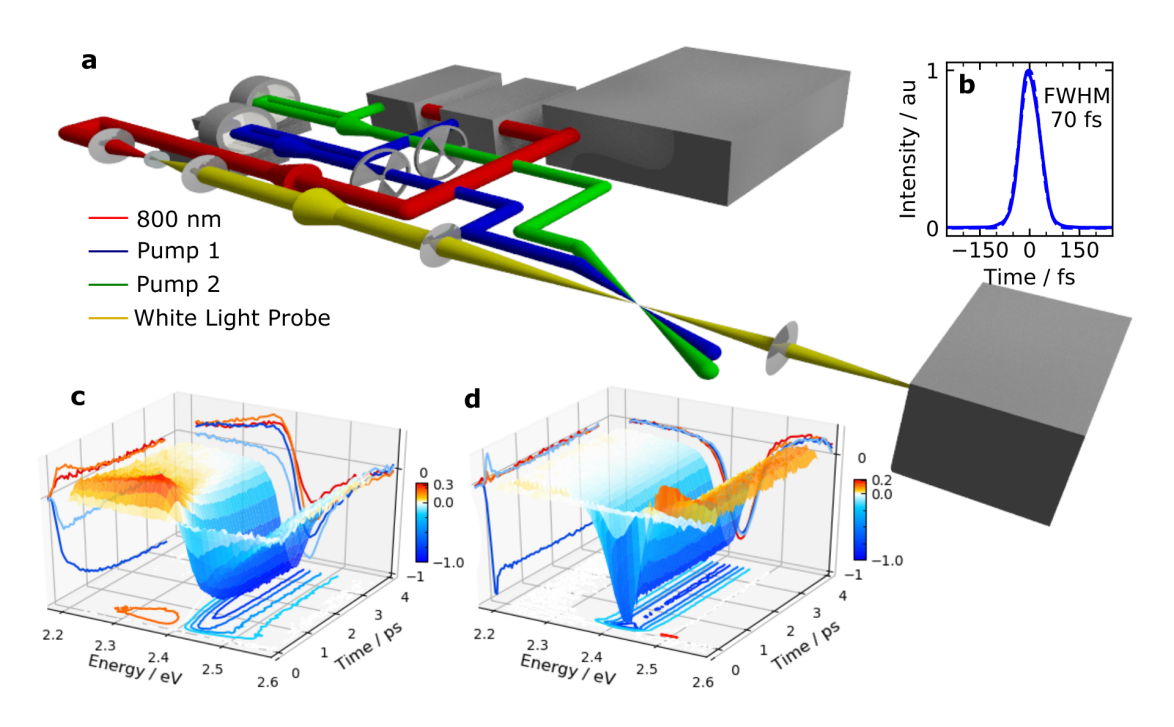


Figure 2.4: Layout of the SRPP setup. **a** Optical components and beam paths. **b** autocorrelation of a 2.4 eV pump pulse. **c,d** SRPP data obtained on CsPbBr₃ NCs for **c** 3.1 eV pump and **d** 2.4 eV pump

Traditional pump-probe experiments will use one pulse to optically excite the sample, and another to probe the effect of that pump pulse. In SRPP, two pump-probe experiments are performed in parallel, with two different pump wavelengths. To observe pump energy effects on dynamics in traditional pump-probe spectroscopy, one experiment at a given pump wavelength must run its course. Afterwards the pump wavelength is tuned, and a second experiment is started. In the meantime, the sample may have degraded or the laser drifted in some way, creating systematic error. In SRPP these two experiments are performed in parallel, making the effect of the pump energy obvious and removing artifacts in the comparison due to degradation or drift.

The experimental layout and results from the SRPP setup are shown in figure 2.4. Figure 2.4a shows the layout. 2.4 mJ, 70 fs pulses at 810 nm are produced in a Ti:Saph amplifier. 90% of this energy is used to drive two optical parametric amplifiers (OPAs). These OPAs serve to convert the 810 nm pulses to visible wavelengths, which are depicted

by the blue and green beams in figure 2.4a. The remainder of the 810 nm beam is used to generate a white-light continuum probe through SPM in sapphire, shown as the red and yellow beams in figure 2.4a for the 810 nm and white light probes respectively. To perform a general pump-probe experiment, the excited sample is probed by the probe pulse on one shot, and on the next shot the pump is blocked and the unexcited sample is probed. The pump-probe signal is the difference in these two values, as given by equations 2.18 to 2.20. The signal monitored in this case is the change in absorption of the excited sample.

$$\Delta OD(t) = OD^{off} - OD^{on}(t) \tag{2.18}$$

$$= \log \left(\frac{I_{pr}^{off}}{I_{ref}}\right) - \log \left(\frac{I_{pr}^{on}}{I_{ref}}\right) \tag{2.19}$$

$$= \log \left(\frac{I_{pr}^{off}}{I_{pr}^{on}} \right) \tag{2.20}$$

Here OD is the sample optical density, the superscripts on/off denote whether or not the pump is blocked, and I is the detected intensity of the probe pulse. In typical linear absorption experiments the intensity of the transmitted beam must be compared to a reference, this is I_{ref} in equation 2.19, which cancels out in the subtraction of logarithms.

The arrival time of each of the pump pulses is set by precisely controlled delay stages. The pump is blocked by a chopper in each pump arm. By scanning the delay time between pump and probe pulses, and scanning a monochromator or detecting a spectrum on a CCD, time and energy resolved ΔOD signals can be retrieved. These are shown in figure 2.4**c**,**d**. In figure 2.4**c**, the sample is excited by a pulse centered at 3.0 eV, roughly 600 meV above the band edge of the sample. Fast electronic relaxation to the band edge can be seen in the growth of the negative signal near 2.4 eV in the first picosecond. In figure 2.4**d** the sample is excited at the band edge. Here, population of the band edge state is

instantaneous so no electronic relaxation is observed. Nuclear dynamics, however, can still be observed through either phonons [34, 35] or polaron formation (see chapter 5).

Since temporal resolution is no longer limited by the electronic response time of a slow detector, dynamics on sub-ps timescales can be observed. The new limit on temporal resolution is the area of temporal overlap between pump and probe pulses at time zero, mathematically speaking their cross-correlation. This is called the instrument response function (IRF) and describes the detected signal for a kronecker- δ system response. The IRF between two intensity envelopes, $I_1(t)$ and $I_2(t)$, is described below:

$$IRF(\tau) \propto \int_{-\infty}^{+\infty} I_1(t)I_2(t-\tau)dt$$
 (2.21)

For two Gaussian pulses with FWHM of σ_1 and σ_2 , this evaluates to a third Gaussian with FWHM $(\sigma_1^2 + \sigma_2^2)^{1/2}$. The pump and probe pulses used in the SRPP experiments have typically ≈ 70 fs FWHM, giving a total temporal resolution on the order of 100 fs. An auto-correlation of a 2.4 eV pump pulse is shown in figure 2.4b with FWHM of 70 fs, demonstrating the excellent resolution for SRPP experiments. The IRF can be measured precisely through cross-correlation between pump and probe beams, as in figure 2.3. Measurement of the cross-correlation is important for measuring and compensating the probe GVD as well. By moving delay stages as the probe wavelength is scanned in a monochromator, this GVD is effectively cancelled in the measurement (although the IRF can't be improved this way). This means that a ΔOD spectrum can be measured where the red and blue parts of the spectrum experience the same delay relative to the pump.

2.2.2 Contributions to the SRPP signal

For a detailed example of modelling the transient absorption spectrum of CdSe QDs, The group of H.S. Tan has presented an excellent method[36], summarised here and in figure 2.5 and the appendix to chapter 5. For a CdSe QD system with an absorption spectrum as shown in figure 2.5a, there are 3 important excitonic transitions, X1-X3. Generally, there are three overall contributions to the transient absorption signal. These are the ground state bleach (GSB), stimulated emission (SE), and excited state absorption (ESA). The shape and sign of these three contributions is depicted in figure 2.5b. Ground state bleach is a reduction in absorption due to depopulation of the ground state, and creates a negative Δ OD signal that follows the shape of the excitonic absorption spectrum, the three filled curves in figure 2.5a and the orange spectrum in figure 2.5b. Stimulated emission is the photo-induced recombination of electrons and holes, which can be used to monitor the population of electrons and holes. Because SE increases optical power in the probe beam, it appears as a negative signal in a Δ OD spectrum at the energy of the electron-hole recombination, as in the yellow curve in figure 2.5b. ESA is absorption from one excited state to another, for QDs this could be creation of a second exciton or an intraband absorption in the IR. This signal is absorptive, so appears as a positive signal in a Δ OD spectrum. This signal follows the spectrum of the excited state transitions, as in .

The overall interaction between two excitons is attractive, and the bound two exciton system is called a *biexciton*. The biexciton is slightly lower in energy than twice the singly excited energy, and this difference is called the biexciton binding energy. Transient absorption spectroscopy is one of many methods for determining the biexciton binding energy [37, 38, 36], but there are several others, and there are several ways to describe the biexciton binding energy to account for fine structure in both the exciton and biexciton [39, 40]. The biexciton binding energy is the main reason that the ESA and GSB contributions don't exactly cancel, since ESA will be redshifted with respect to GSB.

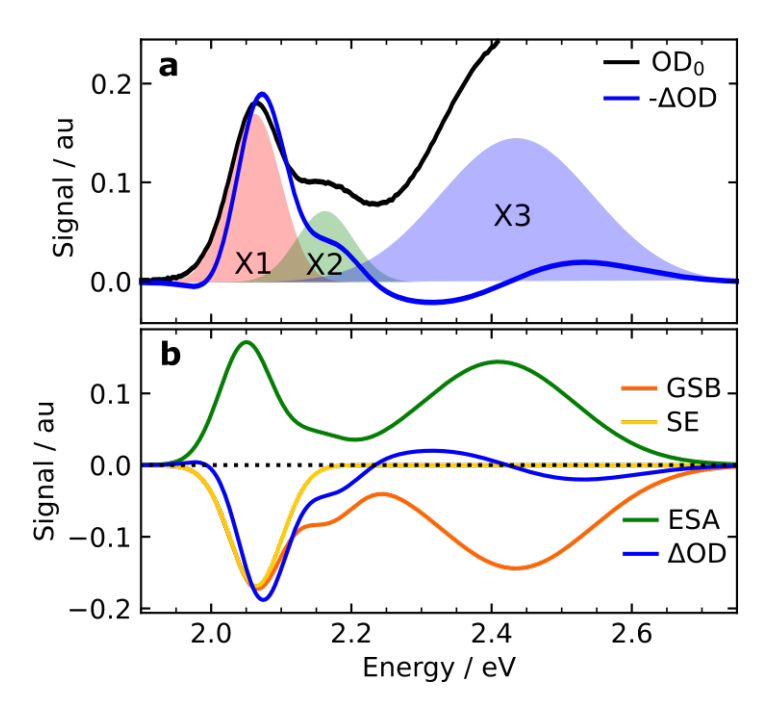


Figure 2.5: Contributions to the transient absorption signal of CdSe QDs. **a** The transient absorption spectrum (blue line) closely follows the linear absorption (black line) near the first excitonic peak. The overall absorption spectrum can be modelled as three excitonic transitions (filled curves) on top of a polynomial background. **b** The TA spectrum has 3 contributions; negative GSB and SE, and positive ESA.

2.2.3 Electronic relaxation

Electronic relaxation is the rapid relaxation of electrons and holes from initially excited states towards the band edge. Measures of electronic relaxation rates are important in designing useful materials, as highly excited charge carriers are necessary for applications like hot-carrier photocells [41]. Examining size and state dependence can shed light on the relative importance of three decay channels: phonon-mediated, surface trapping, and electron-hole Auger energy transfer.

As a QD decreases in size, the excitonic energy levels get further apart. At some point the separation in energy is greater than the optical phonon modes, and this decay channel should become less important. At the same time, surface traps play a more important role, as core electrons and holes will be closer to the surface. The final effect,

Auger energy transfer, describes transfer of energy from one excited carrier to another. For CdSe QDs it's the electron that transfers its energy to the hole, based on the effective mass of the two particles. This brings the electron to the band edge and gives the hole excess kinetic energy.

To untangle the relaxation pathways, a state-resolved approach is necessary. The CdSe absorptions in 1.4c show that the difference between the first two transitions is only in the hole state. By exciting this transition and monitoring signals unique to the hole, it is possible to extract hole relaxation times. By exciting the third transition, which couples P states in the conduction and valence bands, and monitoring electron signals, the relaxation time of electrons can be found. Previous work in our group has already explored this, and found that holes take significantly longer to reach the band edge, despite having a higher density of states that would increase phonon relaxation [42, 43]. Figure 2.6 summarises some of these results. Figure 2.6a and b shows the electron and hole cooling signals, respectively. By simultaneously probing the band edge pump signal, band edge dynamics are controlled for (red lines in figure 2.6a,b). The difference between the band edge pump and the excited state pumps for electrons and holes are shown in figure 2.6c,d respectively. This controls for any signal arising from surface traps or Auger recombination of band edge excitons. Figure 2.6e shows the cooling rate as a function of QD size, reported as the energy gap between the band edge and the pumped state. Smaller crystals have larger gaps and faster decay rates, opposite of the expected trend for phonon-mediated relaxation. The picture that emerges is that electrons very quickly transfer energy to holes. Holes then decay to the band edge through phonon interactions. A state-resolved approach is necessary to untangle these pathways; by exciting at only one energy electron and hole pathways cannot be discerned. An even blurrier picture emerges in size-dependant studies. By exciting all samples at one convenient energy you excite a different initial state across samples, so results are completely useless.

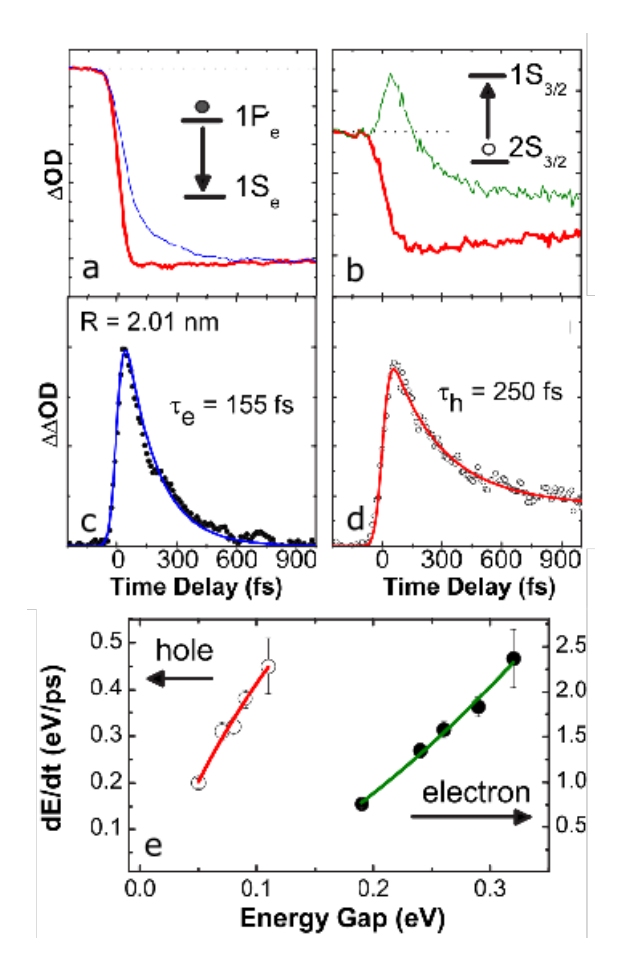


Figure 2.6: Overview of carrier cooling in CdSe QDs through SRPP. **a** Pumping the $|1P_e1P_{3/2}\rangle$ transition and probing the band edge bleach monitors electron cooling. **b** Pumping the $|1S_e2S_{3/2}\rangle$ transition and probing a sub-band edge ESA monitors hole cooling. **c**, **d** Subtracting out the contribution from the band edge pump (red lines in **a**,**b**) controls for dynamics of the ground state, so that only excited state dynamics of the **c** electron and **d** hole remain. **e** The size dependence of electron and hole cooling rates, as a function of the gap between the pumped state and the band edge. Figure reproduced from Cooney, Phys. Rev. B, 2007

•

The results discussed here are important to keep in mind when analysing results for new systems. What are the important relaxation channels at play? How should these behave with size or surface passivation? These questions will be explored in Chapter 5, section 5.3.

2.2.4 Auger recombination

The lowest conduction band state has *S*-type symmetry, and can thus hold 2 excitons. These two excitons interact through Coulomb and correlation potentials to form a bound two exciton system called a biexciton. Since there are now two bodies in the system, a new non-radiative channel is opened up; Auger recombination. This is schematically shown in figure 2.7a. One exciton recombines, transferring all of its energy to the second exciton. In confined systems Auger recombination is fast, on the 10-100 ps timescale, since the two excitons have significant interaction in the confined volume. Again, other non-radiative decay channels exist. For biexciton recombination there are two important ones; Auger processes and surface trapping. Both of these become more important as the QD becomes smaller.

Auger recombination and surface trapping can be distinguished by examining the decay of the band edge bleach under increasing pump fluence. At low fluence only single excitons exist and the bleach should decay on a very long time scale of the population decay rate, several nanoseconds. As fluence increases biexcitons start to contribute to the bleach signal, and these decay very quickly. This manifests in the growth of a fast decaying component with fluence. If the system is well passivated, only the Auger channel is open and the decay in the first few hundred picoseconds is essentially single exponential. Since only two excitons can occupy the band edge state, the normalized signal goes from -2 at early times to -1 at late times (single exciton recombination is ignored). For poorly passivated systems surface trapping occurs at rate similar to Auger recombina-

tion, and there are two parallel channels for biexciton decay. Since some excitons are lost to surface traps that don't contribute to the bleach, the normalized signals go from -2 to something less than -1. These ideas are presented in figure 2.7b, where the band edge bleach decay under very high fluence for three different samples is shown. Under these conditions, practically all nanocrystals initially have two excitons, but poorly-passivated or photo-treated samples quickly lose one to either Auger recombination or surface trapping. These ideas will be further discussed in chapters 4 and 5, in relation to specific systems.

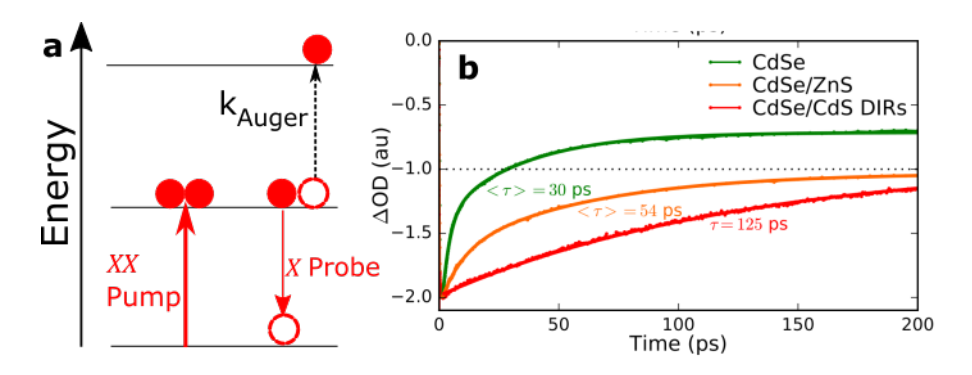


Figure 2.7: Auger recombination in CdSe QDs is determined by surface passivation. **a** Schematic depicting the Auger recombination process. **b** Auger decay measurement across three CdSe-based systems with similar core sizes.

One further point to note is that the scaling of the Auger rate with fluence gives information as to the nature of the interacting particles. Auger processes occur in bulk systems as well, although they are not as important because of the delocalized carriers that have little interaction in most cases. This is famously responsible for the Auger droop in LEDs that cause a loss of efficiency at high driving currents [44]. In bulk systems at room temperature free carriers are responsible for Auger interactions. Two free carriers recombine and transfer their energy to a third carrier, so it is a three-body process that scales as n^3 . In quantum confined systems, as discussed above, it is an interaction between two bound excitons. For some systems that support three or more excitons, it is possible to compare the rates k_{XXX} describing tri-exciton recombination and k_{XX} describing biex-

citon recombination to distinguish quantum confined excitonic systems versus bulk, free carrier systems. In excitonic systems the ratio of these rates will be $3^2/2^2 = 2.25$. In free carrier systems it will instead be $3^3/2^3 = 3.375$. This method showed that carbon nanotubes are excitonic systems [45, 46]. In systems where other decay channels compete with Auger, such as surface trapping or phonon-assisted recombination, this analysis is not so simple.

2.2.5 Gain

When determining whether or not a material is a good candidate as an optical gain medium, there are several factors to consider. The most important, in terms of lasing threshold, is whether it acts as a three level or as a four-level system. To demonstrate this, a brief description of laser dynamics in two, three, and four level systems can be found in appendix 2. Other important considerations are the materials thermal conductivity and how much the materials' refractive index changes with temperature, these two effects determine the maximum output power that can be achieved before a laser becomes unstable.

Since very early in the development of quantum dots (QDs), it was thought that the observed Stokes' shift would lead to a three level system that could support optical gain [47]. This is of great interest because the QD system is size tunable; the laser wavelength can be chosen to be any value in the size tuning of the QDs. In conventional systems, achieving a particular laser wavelength often requires external non-linear frequency conversion, or working with molecular dyes that tend to bleach over time. Using quantum dots as the gain medium opens the door to monolithic lasers at any wavelength, spanning the visible spectrum with CdSe[48] and well into the IR with PbSe based QDs.

An example of CdSe Quantum dot lasers operating in the green and red is shown in figure 2.8. Epitaxially grown QDs have already seen rapid progress in this field; with

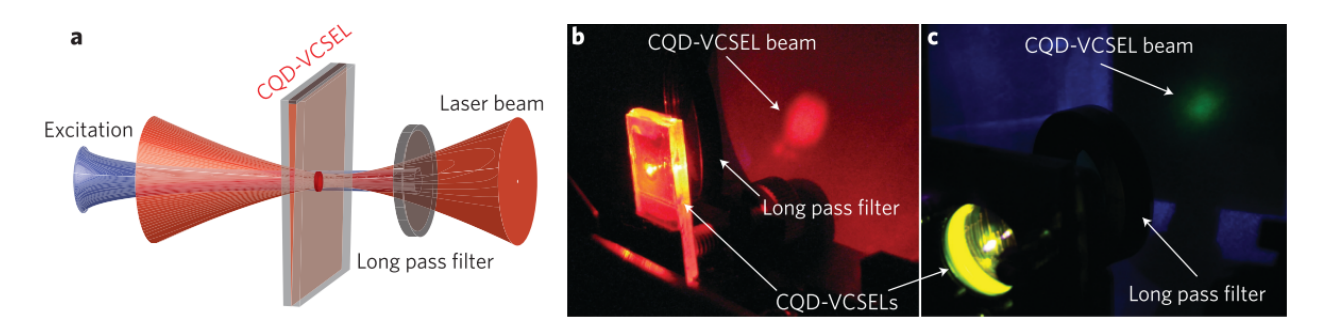


Figure 2.8: Red and green lasing from films of CdSe QDs. **a** laser design including pump beam, active medium, and cavity. **b,c** Lasing in action for **b** red and **c** green laser wavelengths. Reproduced from [48]

efficient, stable, electrically driven laser systems in the IR appearing as early as the 1990s [49, 50]. Epitaxial systems have also been shown to support mode-locked operation, with ~ 400 fs operation at \sim mW average powers. Because of the small size of these laser cavities they have very high repetition rates, approaching 100 GHz [51].

For colloidal systems, lasing is more difficult. This is due to polydisperisty of samples and the difficulty in transporting charge through the organic film and capping ligands, as opposed to using the solid medium of epitaxially grown QDs. Despite these difficulties, remarkable progress has been made. The group of Ted Sargent at the University of Toronto have synthesised strained quantum dots that have narrow emissive linewidths, due to an exaggerated fine structure splitting [52]. This system displays high PL quantum yield and cw lasing. The group of Zeger Hens and Pieter Geiregat have also studied a 4-level quantum dot system, HgTe, that uses intergap trap states for lasing action in the mid-IR at extremely low thresholds, in terms of pump power and exciton occupation[53]. It is also impossible to discuss colloidal quantum dot lasing without mentioning the work of Victor Klimov, who early on discussed the important concept of decoupling the lasing emissive transition from excited state absorption to the biexciton, as well as the idea of single exciton gain [47]. Recently his group has been developing an electrically driven QD laser[54, 55].

One consistent approach to colloidal QD laser systems is finding the appropriate heterostructure. The three important types of heterostructures are shown in figure 2.9. By growing a shell of the appropriate size, shape and composition the QD core can be decoupled from surface states [56]. By controlling the composition of the shell and the alignment of conduction and valence bands, it is possible to create a type-I system, a type-II system that separates electrons from holes, or to delocalize either of the carriers. Type-I systems behave like core-only QDs that are removed from their environment. In type-I systems less surface emission is observed and photo-luminescence quantum yield is increased. Type-II systems act to spatially separate electrons and holes, by having, for example the valence band of the core above that of the shell and the conduction band of the core below that of the shell. Type-II systems tend to have long radiative recombination times and weaker oscillator strengths, due to the physical separation of carriers. A third type of heterostructure is one in which either the conduction or valence band of the core is nearly degenerate with the shell. In this case the carrier in the nearly degenerate band is delocalized over the core/shell interface.

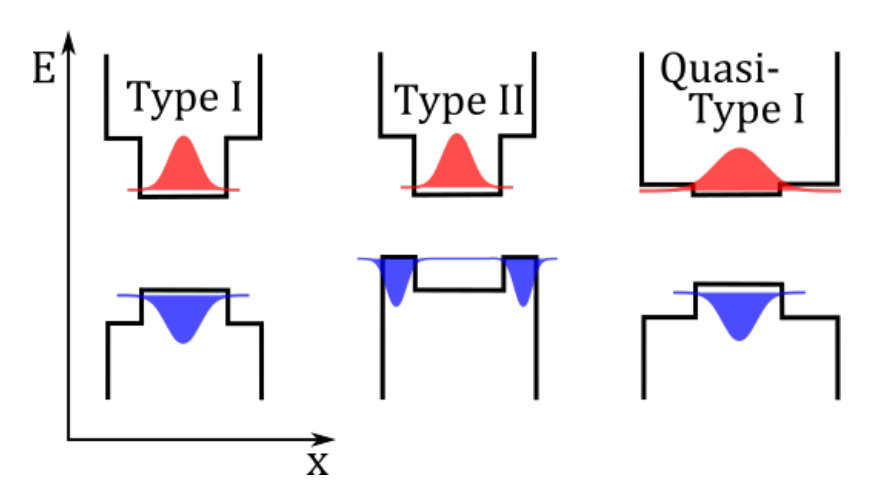


Figure 2.9: Types of heterostructures classified by band alignment. Hole wavefunctions are depicted in blue, electron wavefunctions in red.

A common method for determining gain is through amplified spontaneous emission (ASE). Here, the sample is optically pumped along a line and the fluorescence is detected. At a certain threshold of pump energy, the spontaneous emission travelling along

the line of excitation can initiate stimulated emission, getting amplified as it interacts with the excited sample. This results in a threshold behaviour, where below threshold any spontaneous emission on average is absorbed along that line of travel. At threshold, the sample is transparent, and above threshold there is amplification. This amplification is apparent in two measures of fluorescence as shown in figure 2.10; the overall intensity of the emitted light, and in the appearance of a narrow bump in the spectrum. The intensity of emission increases more quickly along the line of travel at the expense of isotropic spontaneous emission above threshold, so there is a step change in the slope of emission vs. pump intensity. this is shown in figure 2.10.

The narrow bump is due to ASE, and it's shape is narrowed for two reasons.

- 1. Because certain parts of the emission spectrum have residual absorption there will be a higher threshold for ASE.
- 2. In a homogeneously broadened system, amplification at one frequency means that the emitter cannot create ASE at another frequency. This leads to competition between parts of the spectrum, amplification at one frequency depletes gain at other parts of the spectrum.

This narrowed bump is apparent in figure 2.10**a**.

A more precise method for determining gain parameters is SRPP. By subtracting the change in absorption from the linear absorption, the nonlinear absorption of the excited state is retrieved, as in equation 2.22.

$$OD_{NL}(\omega) = OD_0(\omega) + \Delta OD(\omega)$$
 (2.22)

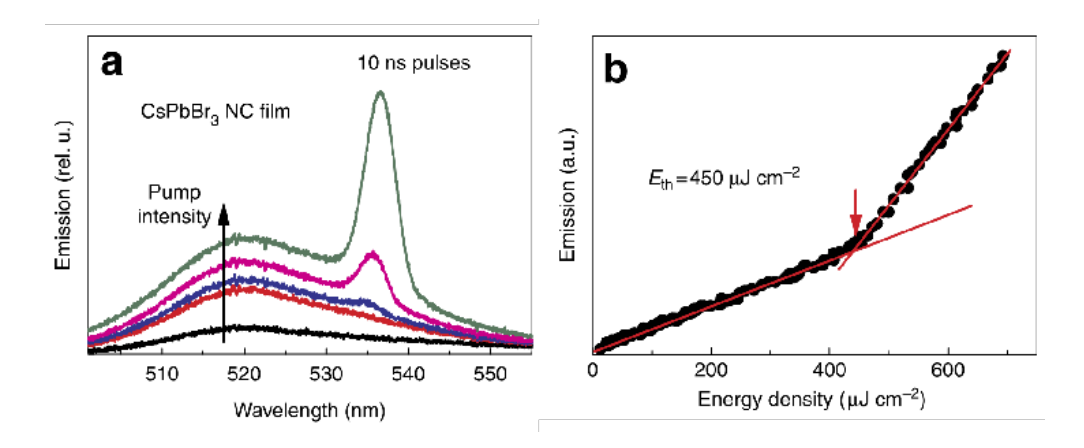


Figure 2.10: Two signs of amplified spontaneous emission (ASE) in thin films of CsPbBr₃ NCs. **a** A narrow bump in the emission spectrum where ASE takes place. **b** A step change in the increase of intensity with pump power, detected along excitation axis. Reproduced from [57]

Gain occurs for negative OD_{NL} . SRPP has the advantage of detecting the *entire* gain spectrum as a function of pump power and time, instead of simply the energies that are amplified. ASE will also overestimate gain thresholds in systems with very short-lived lasing upper states, as these states will decay before they can participate in the ASE process[58], and with the ~ 100 fs resolution of SRPP this is not an issue. The greatest advantage of SRPP is the ability to see the effect of the initial state on gain parameters, which resolved many open questions in this field [59, 60]. An application of SRPP to a type-I CdSe QD in a CdS rod system is presented in chapter 4. It will be shown that SRPP is a powerful tool in determining gain characteristics and electron-phonon coupling.

Bibliography

- [1] Lewenstein, M.; Balcou, P.; Ivanov, M. Y., 't Anne L'huillier; Corkum, P. B.; Livermore, L.; *Theory of high-harmonic generation by low-frequency laser fields*; Tech. Rep.; 1994. https://journals.aps.org/pra/pdf/10.1103/PhysRevA.49.2117.
- [2] L'Huillier, A.; Balcou, P. Physical Review Letters 1993, 70, 774–777.
- [3] Pfeiffer, A. N.; Cirelli, C.; Landsman, A. S.; Smolarski, M.; Dimitrovski, D.; Madsen, L. B.; Keller, U. *Physical Review Letters* **2012**, *109*, 1–5.
- [4] Dantus, M.; Rosker, M. J.; Zewail, A. H. J. Chem. Phys. 1987, 87, 129–132.
- [5] Fleming, G. R.; Passino, S. A.; Nagasawa, Y. *Philosophical Transactions of the Royal Society A: Mathematical, Physical and Engineering Sciences* **1998**, 356, 389–404.
- [6] Maroncelli, M.; Macinnis, J.; Fleming, G. R. 1988, 243.
- [7] Cocker, T. L.; Jelic, V.; Gupta, M.; Molesky, S. J.; Burgess, J. A.; Reyes, G. D. L.; Titova, L. V.; Tsui, Y. Y.; Freeman, M. R.; Hegmann, F. A. *Nature Photonics* **2013**, *7*, 620–625.
- [8] Mrejen, M.; Yadgarov, L.; Levanon, A.; Suchowski, H. Science Advances 2019, 5, 1-6.
- [9] Schumacher, Z.; Miyahara, Y.; Spielhofer, A.; Grutter, P. *Physical Review Applied* **2016**, 5, 1–6.

- [10] Aeschlimann, M.; Brixner, T.; Fischer, A.; Kramer, C.; Melchior, P.; Pfeiffer, W.; Schneider, C.; Strüber, C.; Tuchscherer, P.; Voronine, D. V. *Science* **2011**, 333, 1723–1726.
- [11] Rose-Petruck, C.; Jimenez, R.; Guo, T.; Cavalleri, A.; Siders, C. W.; Ráksi, F.; Squier, J. A.; Walker, B. C.; Wilson, K. R.; Barty, C. P. Nature 1999, 398, 310–312.
- [12] Morrison, V. R.; Chatelain, R. P.; Tiwari, K. L.; Henadoui, A.; Bruhács, A.; Chaker, M.; Siwick, B. J. *Science* **2014**, *346*, 463–463.
- [13] Siwick, B. J.; Dwyer, J. R.; Jordan, R. E.; Miller, R. J. Science 2003, 302, 1382–1385.
- [14] Murata, H.; Morimoto, A.; Kobayashi, T.; Yamamoto, S. *IEEE Journal on Selected Topics in Quantum Electronics* **2000**, *6*, 1325–1331.
- [15] Wu, R.; Supradeepa, V. R.; Long, C. M.; Leaird, D. E.; Weiner, A. M. *Optics Letters* **2010**, *35*, 3234.
- [16] Klenner, A.; Golling, M.; Keller, U. Optics Express 2014, 22, 11884.
- [17] Fork, R. L.; Greene, B. I.; Shank, C. V. Citation: Appl. Phys. Lett. Applied Physics Letters Applied Physics Letters Journal of Applied Physics 1981, 38, 671–270.
- [18] Keller, U.; Miller, D. A. B.; Boyd, G. D.; Chiu, T. H.; Ferguson, J. F.; Asom, M. T. *Optics Letters* **1992**, *17*, 505–507.
- [19] Spence, D. E.; Kean, P. N.; Sibbett, W. 1991, 16, 42–44.
- [20] Oelker, E.; et al. Nature Photonics 2019, 13, 714-719.
- [21] Strickland, D.; Mourou, G. Optics Communications 1985, 56, 219–221.
- [22] Li, W.; et al. Optics Letters 2018, 43, 5681.
- [23] Eia.gov; U.S. Energy Information Administration; https://www.eia.gov/energyexplained/us-energy-facts/. https://www.eia.gov/energyexplained/us-energy-facts/.

- [24] Geddes, C. G. R.; Toth, C. S.; Van Tilborg, J.; Esarey, E.; Schroeder, C. B.; Bruhwiler, D.; Nieter, C.; Cary, J.; Leemans, W. P. *Nature* 2004, 431, 538–541.
- [25] Trebino, R. Frequency-Resolved Optical Gating: The Measurement of Ultrashort Laser Pulses; Springer, 2000.
- [26] Wright, J. C. Annual Review of Physical Chemistry 2011, 62, 209–230.
- [27] Jonas, D. M. Annual Review of Physical Chemistry 2003, 54, 425–463.
- [28] Underwood, D. F.; Kippeny, T.; Rosenthal, S. J. Journal of Physical Chemistry B 2001, 105, 436–443.
- [29] Kim, J.; Yoon, T. H.; Cho, M. Journal of Physical Chemistry Letters 2020, 11, 2864–2869.
- [30] Mathew, R.; Dilcher, E.; Gamouras, A.; Ramachandran, A.; Yang, H. Y. S.; Freisem, S.; Deppe, D.; Hall, K. C. *Physical Review B Condensed Matter and Materials Physics* **2014**, *90*, 1–6.
- [31] Tournois, P. Optics Communications 1997, 140, 245–249.
- [32] Shim, S.-H.; Strasfeld, D. B.; Fulmer, E. C.; Zanni, M. T. Optics Letters 2006, 31, 838.
- [33] Lozovoy, V. V.; Pastirk, I.; Dantus, M. Optics Letters 2004, 29, 775.
- [34] Walsh, B. R.; Sonnichsen, C.; MacK, T. G.; Saari, J. I.; Krause, M. M.; Nick, R.; Coe-Sullivan, S.; Kambhampati, P. *Journal of Physical Chemistry C* **2019**, *123*, 3868–3875.
- [35] Tyagi, P.; Cooney, R. R.; Sewall, S. L.; Sagar, D. M.; Saari, J. I.; Kambhampati, P. *Nano Letters* **2010**, *10*, 3062–3067.
- [36] Zhang, C.; Do, T. N.; Ong, X.; Chan, Y.; Tan, H. S. Chemical Physics 2016, 481, 157–164.
- [37] Sewall, S. L.; Franceschetti, A.; Cooney, R. R.; Zunger, A.; Kambhampati, P. *Physical Review B* Condensed Matter and Materials Physics **2009**, 80, 1–4.
- [38] Sewall, S. L.; Cooney, R. R.; Anderson, K. E. H.; Dias, E. A.; Kambhampati, P. *Physical Review B* **2006**, *74*, 235328.

- [39] Palato, S.; Seiler, H.; Baker, H.; Sonnichsen, C.; Brosseau, P.; Kambhampati, P. *Journal of Chemical Physics* **2020**, 152.
- [40] Seiler, H.; Palato, S.; Sonnichsen, C.; Baker, H.; Kambhampati, P. *Nano Letters* **2018**, *18*, 2999–3006.
- [41] Kahmann, S.; Loi, M. A.; Hot carrier solar cells and the potential of perovskites for breaking the Shockley-Queisser limit; 2019. https://pubs.rsc.org/en/content/articlepdf/2019/tc/c8tc04641g.
- [42] Cooney, R. R.; Sewall, S. L.; Anderson, K. E. H.; Dias, E. A.; Kambhampati, P. *Physical Review Letters* **2007**, *98*, 1–4.
- [43] Cooney, R. R.; Sewall, S. L.; Dias, E. A.; Sagar, D. M.; Anderson, K. E.; Kambhampati, P. *Physical Review B Condensed Matter and Materials Physics* **2007**, *75*, 1–14.
- [44] Kioupakis, E.; Rinke, P.; Delaney, K. T.; Van De Walle, C. G. Applied Physics Letters 2011, 98.
- [45] Wang, F.; Dukovic, G.; Brus, L. E.; Heinz, T. F. Science 2005, 308, 838–841.
- [46] Huang, L.; Krauss, T. D. Physical Review Letters 2006, 96, 8–11.
- [47] Klimov, V.; Mikhailovsky, A.; Xu, S.; Malko, A.; Hollingsworth, J.; Leatherdale, C.; Eisler, H.; Bawendi, M. *Science* {(*New*} *York*, {*N.Y.*)} **2000**, 290, 314–317.
- [48] Dang, C.; Lee, J.; Breen, C.; Steckel, J. S.; Coe-Sullivan, S.; Nurmikko, A. *Nature Nanotechnology* **2012**, *7*, 335–339.
- [49] Maximov, M. V.; et al. Journal of Applied Physics 1998, 83, 5561–5563.
- [50] Chen, S.; Li, W.; Wu, J.; Jiang, Q.; Tang, M.; Shutts, S.; Elliott, S. N.; Sobiesierski, A.; Seeds, A. J.; Ross, I.; Smowton, P. M.; Liu, H. *Nature Photonics* 2016, 10, 307–311.
- [51] Rafailov, E.; Cataluna, M.; Sibbett, W. Nature Photonics 2007, 1, 395–401.
- [52] Fan, F.; et al. Nature 2017, 544, 75–79.

- [53] Geiregat, P.; Houtepen, A. J.; Sagar, L. K.; Infante, I.; Zapata, F.; Grigel, V.; Allan, G.; Delerue, C.; Thourhout, D. V.; Hens, Z. *Nature Materials* 2017 17:1 **2017**, 17, 35.
- [54] Lim, J.; Park, Y.-S.; Klimov, V. I. *Nature Materials* **2017**, *17*, 42–49.
- [55] Roh, J.; Park, Y. S.; Lim, J.; Klimov, V. I. Nature Communications 2020, 11, 1–10.
- [56] Walsh, B. R.; Saari, J. I.; Krause, M. M.; Nick, R.; Coe-Sullivan, S.; Kambhampati, P. *The Journal of Physical Chemistry C* **2015**, *119*, 16383–16389.
- [57] Yakunin, S.; Protesescu, L.; Krieg, F.; Bodnarchuk, M. I.; Nedelcu, G.; Humer, M.; De Luca, G.; Fiebig, M.; Heiss, W.; Kovalenko, M. V. *Nature Communications* **2015**, *6*, 1–19.
- [58] Kambhampati, P.; Mack, T.; Jethi, L. ACS Photonics 2017, 4, 412–423.
- [59] Cooney, R. R.; Sewall, S. L.; Sagar, D. M.; Kambhampati, P. *Physical Review Letters* **2009**, 102, 1–4.
- [60] Cooney, R. R.; Sewall, S. L.; Sagar, D. M.; Kambhampati, P. Journal of Chemical Physics 2009, 131.

2.A Population kinetics in 2, 3 and 4 level laser systems

2.A.1 2-level systems

When considering the probability of a radiative transition to occur between a ground state $|0\rangle$ and excited state $|1\rangle$, there are three important processes to consider: Relaxation, stimulated emission, and absorption. Relaxation can occur radiatively or non-radiatively, when it comes to laser dynamics it is simply movement between energy levels with no change to the laser radiation field. Stimulated emission can be thought of as the reverse of absorption, a photon incident on the excited system causes relaxation to the ground state with emission of an additional photon with the same frequency, polarization, and wavevector.

Using these 3 processes it is possible to make a system of rate equations to describe the population dynamics of the laser system. Under a few simple assumptions the performance of a laser gain medium can be quantified from physical constants, such as the lifetime and cross-section of the lasing state. For the curious reader, an excellent resource for laser physics and design is Orazio Svelto's *Principles of Lasers*, where many important concepts are given proper attention[1]

As an example, consider a 2-level system with states $|1\rangle$ and $|2\rangle$.

$$\frac{dN_1}{dt} = -\frac{I\sigma}{h\nu}N_1 + k_sN_2 + \frac{I\sigma}{h\nu}N_2$$
 (2.23)

$$\frac{dN_2}{dt} = -\frac{dN_1}{dt} = \frac{I\sigma}{h\nu}N_1 - k_sN_2 - \frac{I\sigma}{h\nu}N_2$$
(2.24)

Here N_1 and N_2 describe the population of the levels $|1\rangle$ and $|2\rangle$, I is the intensity of laser radiation, k_s is the total spontaneous decay rate between levels $|1\rangle$ and $|2\rangle$, ν and σ_{12} are the frequency and cross-section of the laser transition, respectively. It is useful to reframe equations 2.23 and 2.24 in terms of the total population, N, and the population inversion, $\Delta N = N_2 - N_1$. At equilibrium, when $dN_i/dt = 0$ for all i, the system has the following solution:

$$\Delta N = \frac{-N}{1 + I/I_0} \tag{2.25}$$

$$I_s = \frac{h\nu k_s}{2\sigma} \tag{2.26}$$

It is immediately apparent, that for whatever positive value of I, ΔN is strictly negative. In the limit of intense pumping, $I \gg I_s$, ΔN approaches 0, or transparency. This reflects the fact that a closed 2-level system cannot lase. Below it will be shown that a minimum three level system is required, but a four level system is best.

2.A.2 3-level systems

Consider the three level system shown in figure 2.11. The transition $|1\rangle \rightarrow |3\rangle$ is pumped, followed by fast relaxation to level $|2\rangle$. It is then possible to lase between levels $|1\rangle$ and $|2\rangle$, once more than half the population is in the upper lasing state. In this system, the relaxation from $|3\rangle$ to $|2\rangle$ must be very fast, on subpicosecond timescales. This is so that no stimulated emission from $|3\rangle$ to $|1\rangle$ occurs, and pump energy is efficiently transferred to the upper lasing state.

Following our procedure for the two-level system, we write down the system of rate equations governing population dynamics, rewrite in terms of ΔN and N, then solve for the steady state, $dN_i/dt=0$ for all i.

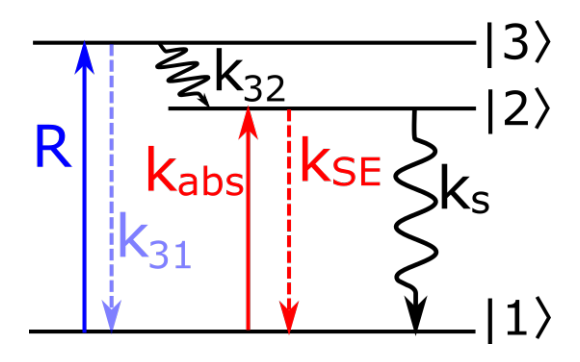


Figure 2.11: Energy level diagram showing a 3 level laser system and relevant population transfer rates.

$$\frac{dN_1}{dt} = -RN_1 + k_{31}N_3 + k_sN_2 + \frac{I\sigma}{h\nu}(N_2 - N_1)$$
(2.27)

$$\frac{dN_2}{dt} = k_{32}N_3 - \frac{I\sigma}{h\nu}(N_2 - N_1) - k_s N_2$$

$$\frac{dN_3}{dt} = RN_1 - (k_{31} + k_{32})N_3$$
(2.28)

$$\frac{dN_3}{dt} = RN_1 - (k_{31} + k_{32})N_3 \tag{2.29}$$

Here we've introduced the pump rate as R. In a system with fast relaxation from the upper level, $k_{32} \gg R, k_{31}$ for all pump intensities. Under steady state conditions equation 2.29 reduces to:

$$N_3 = \frac{R}{k_{21} + k_{22}} N_1 \tag{2.30}$$

which means that $N_3 \ll N_1$ under the condition that $k_{32} \gg k_{31}, R$. Under this condition $N \approx N_1 + N_2$. Substituting equation 2.30 into equation 2.29 and rewriting in terms of ΔN and N yields the following steady state solution:

$$\Delta N = \frac{R/k_s - 1}{I/2I_s + R/k_s + 1} \tag{2.31}$$

$$I_s = \frac{h\nu k_s}{\sigma} \tag{2.32}$$

In this situation a population inversion can exist if the pumping rate is greater than the spontaneous decay rate, or alternatively if more than half of the population is transferred to the upper lasing state. This puts a fundamental threshold of operation on any 3-level laser design.

4-level systems 2.A.3

In a four-level system such as is depicted in figure 2.12, it is possible to have population inversion at very low pump intensities. In these systems there is rapid relaxation from the highly excited state to the upper lasing state, and similarly rapid relaxation from the lower lasing state to the ground state. The system of rate equations and relations between rates are given below:

$$\frac{dN_0}{dt} = -RN_0 + k_{30}N_3 + k_{10}N_1 \tag{2.33}$$

$$\frac{dN_1}{dt} = \frac{I\sigma}{h\nu}(N_2 - N_1) + k_s N_2 - k_{10} N_1 \tag{2.34}$$

$$\frac{dN_2}{dt} = k_{32}N_3 - \frac{I\sigma}{h\nu}(N_2 - N_1) - k_sN_2 \tag{2.35}$$

$$\frac{dN_0}{dt} = -RN_0 + k_{30}N_3 + k_{10}N_1 \qquad (2.33)$$

$$\frac{dN_1}{dt} = \frac{I\sigma}{h\nu}(N_2 - N_1) + k_sN_2 - k_{10}N_1 \qquad (2.34)$$

$$\frac{dN_2}{dt} = k_{32}N_3 - \frac{I\sigma}{h\nu}(N_2 - N_1) - k_sN_2 \qquad (2.35)$$

$$\frac{dN_3}{dt} = RN_0 - (k_{30} + k_{32})N_3 \qquad (2.36)$$

$$k_{32} \gg R, k_{30}; k_{10} \gg \frac{I\sigma}{h\nu}, k_s$$

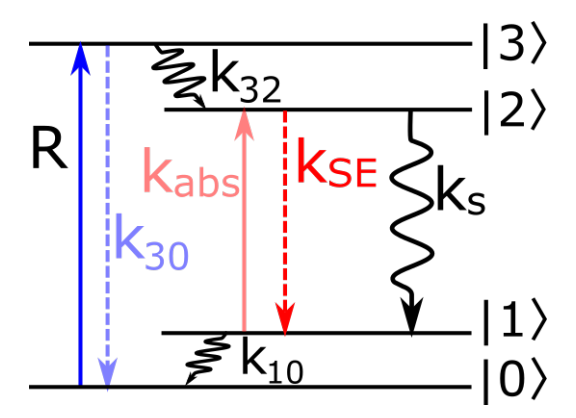


Figure 2.12: Energy level diagram showing a 4 level laser system and relevant population transfer rates.

Following the same steps as we did in our analysis of a three level system, we can eliminate N_3 from the system of equations. We first limit the analysis to the steady state equilibrium condition, $dN_i/dt=0$ for all i. Rearranging produces the following relations.

$$N_3 = \frac{R}{k_{30} + k_{32}} N_0 \approx \frac{R}{k_{32}} N_0 \tag{2.37}$$

$$N_1 = \frac{\frac{I\sigma}{h\nu} + k_s}{\frac{I\sigma}{h\nu} + k_{10}} N_2 \approx \frac{\frac{I\sigma}{h\nu} + k_s}{k_{10}} N_2$$

$$(2.38)$$

Under our assumptions about the rates k_{10} and k_{32} , we have $N_3, N_1 \ll N_0, N_2$, and thus $N \approx N_0 + N_2$ and $\Delta N \approx N_2$

Recasting equations 2.33-2.36 into the form of population inversion, ΔN , and using the relations 2.37 and 2.38, one finds an expression for the population inversion in a four-level system in terms of pumping rate and material parameters σ and I_s .

$$\frac{d\Delta N}{dt} = \frac{dN_2}{dt} - \frac{dN_1}{dt} = 0 \tag{2.39}$$

$$= \frac{-2I\sigma}{h\nu}\Delta N - 2k_sN_2 + k_{32}N_3 - k_{10}N_1 \tag{2.40}$$

Now substituting 2.37 and 2.38 for the terms $k_{32}N_3$ and $k_{10}N_1$ respectively, and using the approximation $\Delta N \approx N_2$:

$$0 = \frac{-2I\sigma}{h\nu}\Delta N - 2k_sN_2 + RN_0 - \left(\frac{I\sigma}{h\nu} + k_s\right)N_2$$
 (2.41)

$$\Rightarrow \Delta N \approx \frac{R}{3k_s(I/I_s+1)} N_0 \tag{2.42}$$

Here we see that population inversion occurs even for very small pump intensities. The lower lasing level is always empty and the upper lasing level is uncoupled from the ground state, so any excitation leads to population in N_2 and any laser radiation is not re-absorbed. This is the best case scenario for low laser thresholds and good power efficiency.

Almost all commercial laser systems are based on a four level system. However, certain laser media have closely spaced 3rd and 4th levels, or 1st and 2nd levels, creating quasi three level systems. In these systems good heat management is required to prevent thermal population of the interfering states. The two important material parameters are the saturation intensity and lifetime of the upper lasing state. The saturation intensity is a measure of small signal gain and also of how much intensity is required to start a laser cavity with a given output coupler. Small saturation intensities mean large gain and low threshold power. The lifetime of the upper lasing state, k_s^{-1} determines how much energy can be stored in the medium, with longer lifetimes meaning more potential to store energy. Long lifetimes are ideal for pulsed laser systems, and some lasers based on forbidden transitions can have lifetimes in the hundreds of microseconds in Nd to several milliseconds in Yb. The decay rate also represents a loss rate, which for 3 level systems must be overcome with a greater pump rate.

Bibliography

[1] Orazio Svelto. Principles of Lasers. 1998.

Chapter 3

Two-dimensional Spectroscopy

Two dimensional electronic spectroscopy (2DES) is a multiple pulse, nonlinear spectroscopy that is capable of monitoring diagonal and off-diagonal elements of the density matrix. That is to say 2DES can observe not only population transfer between states, but also electronic coherence and coupling between states. Furthermore, by using a coherent pair of pulses to pump the sample, 2DES resolves a fundamental limit to SRPP. In SRPP, to address only one particular state with the pump pulse, the bandwidth of the pump pulse can't overlap any other transitions. This limits the pump bandwidth, which limits temporal resolution. By using an interferometric pump pulse pair in 2DES, this limit no longer applies. In this chapter the theoretical and mathematical underpinnings of two-dimensional spectroscopy will be developed. It will be shown that conventional two pulse pump-probe spectroscopy retrieves one part of the third order response function of a system, while two-dimensional spectroscopy can retrieve the entire third order response. This has important consequences for lineshape analysis and experiment design, allowing researchers to exploit phase-cycling or frequency modulation techniques to isolate particular signals. The derivations below will follow closely those of Shaul Mukamel's Principles of Nonlinear Optical Spectroscopy[1] and Peter Hamm and Martin Zanni's Concepts and Methods of 2D Infrared Spectroscopy[2]. Because the concepts and the-

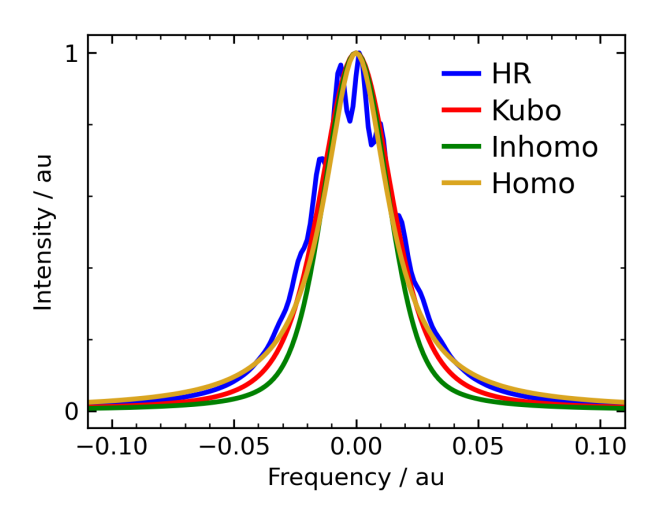


Figure 3.1: Common lineshapes observed in linear spectroscopy. HR refers to Huang-Rhys broadening in a displaced harmonic oscillator model.

ory of multidimensional spectroscopy were born from two-dimensional nuclear magnetic resonance (NMR), much of the terminology is borrowed from that discipline, such as dephasing times T_2 that describe a loss of phase coherence, and T_1 , that describes population relaxation.

To demonstrate the power of 2DES in the analysis of lineshapes, consider the spectra presented in figure 3.1. In linear spectroscopy, the lineshapes arising from homogeneous and inhomogeneous broadening are very similar. Also presented is the intermediate case of a Kubo lineshape, where oscillators undergo spectral diffusion. Even a series of overlapping transitions in a displaced harmonic oscillator can be indistinguishable from a single transition, shown as the blue curve in figure 3.1. Dynamic effects are quite clear in 2DES, and can be isolated through Fourier transform along certain temporal dimensions[3] or by retrieving the center line slope[4, 5] through a single peak. Homogeneous versus inhomogeneous broadening is separated along the diagonal axis of a 2DE spectrum, and is thus made rather obvious.

3.1 The 2DES signal

Two-dimensional spectroscopy is best carried out using the density matrix representation of a statistical collection of quantum systems. The density matrix ρ represents the ensemble statistical average over a collection of quantum systems. The elements of this matrix are shown below:

$$\rho_{ij} = \sum_{n} P_n \langle i | n \rangle \langle n | j \rangle \tag{3.1}$$

$$= \langle c_i c_j^* \rangle \tag{3.2}$$

In equation 3.1, P_n is the ensemble probability of a system occupying state $|n\rangle$, a real, positive number with $\sum_n P_n = 1$. The c_i are the complex coefficients describing the microscopic quantum systems, with important physical interpretations. Examining the diagonal components of ρ :

$$\rho_{ii} = \langle c_i c_i^* \rangle = P_i \tag{3.3}$$

These diagonal elements represent the probability of finding an individual system in quantum state $|i\rangle$. The ρ_{ii} are strictly positive and less than 1, with $\sum_i \rho_{ii} = 1$.

The off-diagonal elements, on the other hand, are complex and describe phase relations between states:

$$\rho_{ij} = \langle c_i c_j^* \rangle = \langle |c_i| |c_j| \exp(i\Delta\phi_{ij}) \rangle \tag{3.4}$$

The $e^{i\Delta\phi_{ij}}$ term in equation 3.4 describes the *phase coherence* between states $|i\rangle$ and $|j\rangle$. Phase coherence can be thought of as the degree to which a collection of systems are in sync. Soldiers marching on a parade ground walk in phase and don't lose coherence in their step. You hear the footfall of every soldier at the same time. There is a very narrow distribution to $\Delta\phi_{ij}$ in equation 3.4. On the other hand, a large group of runners passing

by all have their own pace and stride length, their steps are incoherent. All you hear is a steady background of footfalls. There is a large distribution to $\Delta \phi_{ij}$ in equation 3.4.

3.1.1 System response function

The 2DES signal is described by the material response to a sequence of 3 pulses, emitted in a particular direction with a particular frequency. Let us begin by framing the concept of linear absorption in the induced polarisation of a two-level system.

At time $t=-\infty$, the system is in the ground state and the only non-zero component of the 2×2 density matrix is $\rho_{00}=1$. This system interacts with an optical pulse, which for now will be described as a delta function in time. Optical excitation creates a coherence, or an off-diagonal element ρ_{01} and it's complex conjugate in ρ_{10} . The coherence will oscillate at frequency ω_{01} and decay with the decoherence time T_2 . Of course, there is also a population in the density matrix element ρ_{11} , but we are working in a weak pulse limit where $\rho_{11} \ll \rho_{10}$

$$\rho_{01} = i\mu_{10}e^{-t_1/T_2}e^{-i\omega_{01}t_1} \tag{3.5}$$

In equation 3.5 t_1 is the time after interaction with the first pulse and μ_{10} is the transition dipole moment. The time-dependent system response function is given as:

$$R^{(1)}(t_1) = \langle \mu \rangle = Tr[\mu \rho] \tag{3.6}$$

$$=i\mu_{10}^2 e^{-t_1/T_2} e^{-i\omega_{01}t_1} \tag{3.7}$$

An incident electric field, $E_{inc}(t)$, interacts with the system through the response function given by equation 3.7 to create a polarization, P(t). The polarization radiates a signal

field, $E_{sig}(t_1)$, that is $\pi/2$ out of phase with the polarization.

$$E_{sig}(t_1) \propto iP(t_1) \tag{3.8}$$

$$= i \int_{-\infty}^{+\infty} R^{(1)}(t_1) E_{inc}(t - t_1) dt$$
 (3.9)

This signal field will be superimposed with the incident field, that is to say the signal field is heterodyned by the incident field. The cumulative $\pi/2$ phase shifts in equations 3.7 and 3.8 cause the signal field to be out of phase with the incident field. This creates destructive interference and a reduction in field intensity. This intensity is typically detected through a square-law detector after dispersion by a spectrometer. Mathematically, this is Fourier transformation of the signal, and taking the absolute value squared.

$$S(\omega) = \left| \int_{-\infty}^{+\infty} \left[E_{inc}(t) + E_{sig}(t) \right] e^{i\omega t} dt \right|^2$$
 (3.10)

$$= I_0(\omega) + 2\operatorname{Re}\left[E(\omega)E_{siq}(\omega)\right] + I_{siq}(\omega) \tag{3.11}$$

Usually the term $I_{sig}(\omega)$ can be neglected, since it is so much smaller than $I_0(\omega)$. It should be noted that the energy lost by the electric field is recovered in the system, through the ρ_{11} population term which we have ignored so far.

We will now extend a similar development to a third order response, $R^{(3)}(t_1,t_2,t_3)$ and examine the detection and interpretation of such a signal. We begin again with a pulse creating a coherence on ρ_{01} at time t=0. This coherence again evolves according to equation 3.5. At time $t=t_1$ a second pulse interacts with the system, transferring the coherence to a population on ρ_{11} that evolves along t_2 . This decays with the population time T_1 .

$$\rho_{11}(t_1, t_2) = i\mu_{01}^2 e^{-i\omega_{01}t_1} e^{-t_1/T_2} e^{-t_2/T_1}$$
(3.12)

At time $t = t_1 + t_2$ a third pulse interacts with the sample and creates another coherence which evolves along t_3 . Through these three interactions the molecular response is described as below:

$$\rho_{01}(t_1, t_2, t_3) = i\mu_{10}^3 e^{-i\omega_{01}(t_1 + t_3)} e^{-(t_1 + t_3)/T_2 - t_2/T_1}$$
(3.13)

$$R^{(3)}(t_1, t_2, t_3) = \text{Tr}[\mu \cdot \rho(t_1, t_2, t_3)]$$
(3.14)

$$= i\mu_{10}^4 e^{-i\omega_{01}(t_1+t_3)} e^{-(t_1+t_3)/T_2} e^{-t_2/T_1}$$
(3.15)

In reality, we have only chosen a particular example of light matter interaction. With the complex representations of fields and quantum states there is no reason that the system cannot interact with a negative frequency on the bra, as opposed to a positive frequency on the ket. For example, if the third pulse interacted with the negative frequency this would have created a coherence ρ_{01} that looks somewhat different. We will label this interaction $R_1^{(3)}$ for reasons that will become clear.

$$R_1^{(3)} = i\mu_{10}^4 e^{-i\omega_{01}(t_1 - t_3)} e^{-(t_1 - t_3)/T_2} e^{-t_2/T_1}$$
(3.16)

Equation 3.15 and 3.16 differ in only one term: the oscillating term at ω_{01} . In 3.15 this simply oscillates with the sum of t_1 and t_3 , while in 3.16 there is an echo where $t_1=t_3$. During coherence time t_3 the phase evolution that happened during t_1 is unwound, and these third order response functions are called *rephasing* response functions. Pulse interactions that don't unwind the t_1 phase during t_3 are called *non-rephasing* response functions. The total response of the system is the sum of all possible response functions.

With multidimensional spectroscopy of multilevel systems, it can quickly become difficult to keep track of all the pulse interactions that are possible. One tool to make bookkeeping easier is the double-sided Feynman diagram (DSFD). Here time is on a vertical axis from bottom to top and pulse interactions transform the system through coherences and populations from the left and right. Because an oscillating electric field

has both positive and negative frequency components, they can act on either the *bra* or the *ket* of a system, according to the rotating wave approximation. The DSFD for the pulse ordering in $R_1^{(3)}$ is shown in figure 3.2.

$$\begin{vmatrix} \vec{k}_{sig} & |0\rangle \langle 0| \\ |1\rangle \langle 0| & \vec{k}_{3} \\ |1\rangle \langle 1| & \vec{k}_{1} \\ |0\rangle \langle 0| & \vec{k}_{1} \end{vmatrix}$$

Figure 3.2: The DSFD for the $R_1^{(3)}$ rephasing pathway.

There are some simple rules for interpreting and drawing DSFDs.

- 1. The last interaction is the signal field, which originates from $P^{(3)}(t_1, t_2, t_3)$, is by convention from the *ket*. Corresponding diagrams with the last interaction from the *bra* are the complex conjugate and don't carry additional information.
- 2. Each diagram carries an overall sign $(-1)^n$, where n is the number of interactions on the right, to account for action on the *bra*.
- 3. A right pointing arrow represents E, while a left pointing arrow represents E^* . This electric field not only contains positive and negative frequencies, but also positive and negative wave-vectors and phases.
- 4. The final interaction has wave-vector, frequency and phase given by the sum of the previous interactions.
- 5. The last interaction must end in a population state, $|n\rangle \langle n|$.

For a three level system as shown in figure 3.3a there are a total of 6 pulse interactions possible, and their DSFDs are shown in figure 3.3b. Each of these also has its complex conjugate, which is not shown. Responses R_1 to R_3 are rephasing signals, where the third coherence unwinds the phase evolution in the first coherence. R_4 to R_6

are non-rephasing signals. To borrow terms from pump-probe spectroscopy, R_1 and R_4 correspond to stimulated emission contributions to the signal, R_2 and R_5 to ground state bleach, and R_3 and R_6 to excited state absorption. By rule 2, R_3 and R_6 have an opposite sign to the other interactions, reflecting the absorption process. They also end in an excited state. The various responses will carry different phases and wave-vectors, and oscillate at different frequencies along the various time axes. For example both R_4 and R_5 will have wave-vector $\vec{k_s} = \vec{k_1} - \vec{k_2} + \vec{k_3}$, and similarly phase $\phi_s = \phi_1 - \phi_2 + \phi_3$. This allows some implementations of 2DES to discriminate between rephasing and non-rephasing pathways. The various response functions for a three-level system such as in figure 3.3a are given below:

$$R_1^{(3)}(t_1, t_2, t_3) = i\mu_{10}^4 e^{-i(\omega_{01}(t_1 - t_3))} e^{-(t_1 + t_3)/T_2} e^{-t_2/T_1}$$
(3.17)

$$R_2^{(3)}(t_1, t_2, t_3) = i\mu_{10}^4 e^{-i(\omega_{01}(t_1 - t_3)} e^{-(t_1 + t_3)/T_2} e^{-t_2/T_1}$$
(3.18)

$$R_3^{(3)}(t_1, t_2, t_3) = -i\mu_{10}^2 \mu_{12}^2 e^{-i(\omega_{01}t_1 - \omega_{12}t_3)} e^{-t_1/T_2^{(01)}} e^{-t_3/T_2^{(12)}} e^{-t_2/T_1}$$
(3.19)

$$R_4^{(3)}(t_1, t_2, t_3) = i\mu_{10}^4 e^{-i(\omega_{01}(t_1 + t_3)} e^{-(t_1 + t_3)/T_2} e^{-t_2/T_1}$$
(3.20)

$$R_5^{(3)}(t_1, t_2, t_3) = i\mu_{10}^4 e^{-i(\omega_{01}(t_1 + t_3))} e^{-(t_1 + t_3)/T_2} e^{-t_2/T_1}$$
(3.21)

$$R_6^{(3)}(t_1, t_2, t_3) = -i\mu_{10}^2 \mu_{12}^2 e^{-i(\omega_{01}t_1 + \omega_{12}t_3)} e^{-t_1/T_2^{(01)}} e^{-t_3/T_2^{(12)}} e^{-t_2/T_1}$$
(3.22)

Here the excited state absorption terms, R_3 and R_6 , dephase with T_2 of the first transition during t_1 , then with $T_2^{(12)}$, the dephasing time of the second transition during time t_3 . The total system response will be the sum over all of these terms, with Heaviside step functions to account for causality.

$$S^{(3)}(t_1, t_2, t_3) = \frac{1}{\hbar^3} \theta(t_1) \theta(t_2) \theta(t_3) \sum_{i=1}^6 R_i(t_1, t_2, t_3)$$
(3.23)

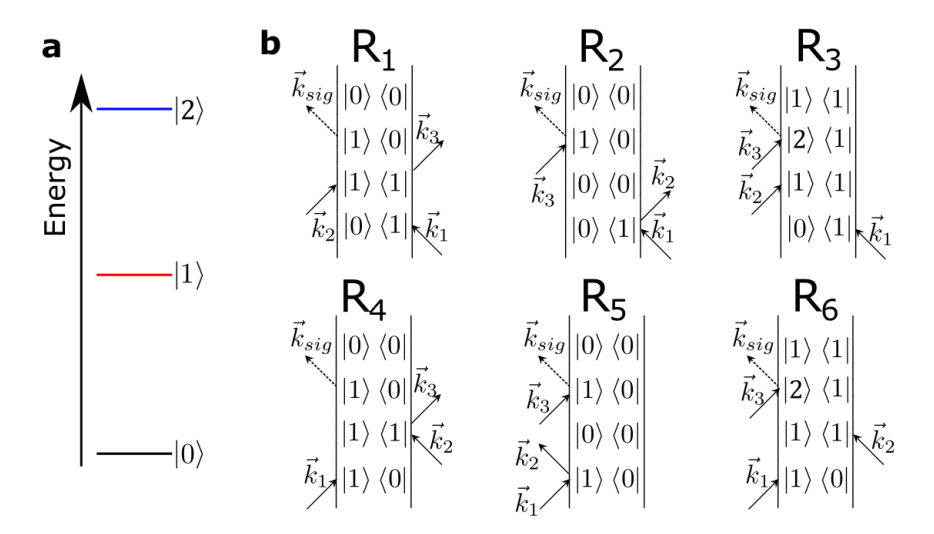


Figure 3.3: Double-sided Feynman diagrams for a 3 level system. **a** A three level system with optical transitions μ_{01} and μ_{12} . **b** The six DSFDs that are possible for this system.

It should be apparent that the DSFDs shown in figure 3.3 can become quite numerous if vibrational or electronic fine structure is taken into account, as in figure 3.8 [3]. Further complications arise from higher order pulse interactions, for example if the first pulse interacts twice with the system to create a $|2\rangle\langle 0|$ coherence along t_1 . There is also the possibility of a so-called two-quantum coherence along t_2 through two interactions on the right or left in a row [6].

One complication of 2DES is that the full phase information of the signal field must be retrieved. This is most easily accomplished through an optical local oscillator pulse. This is usually a fourth pulse used to heterodyne the optical signal, so that the phase evolution of the signal can be monitored. It can also be one of the pulses used in the experiment, which is the case for 2DES in the pump-probe[7] or co-linear geometries[8].

With this picture of nonlinear light-matter interactions, it is now possible to expand SRPP spectroscopy as a special case of 2DES. If the two pump pulses used in 2DES arrived at the same time, with the same wave-vector, and no interferometric scanning were performed we would have the exact same experiment that is described in 2.2. The three DSFDs that are responsible for the ground state bleach, stimulated emission, and

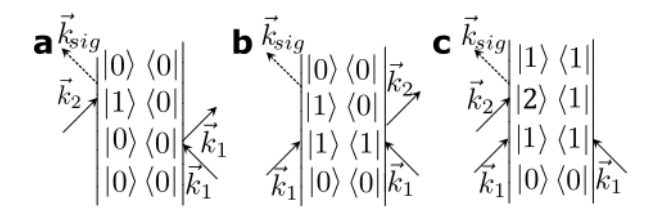


Figure 3.4: The DSFDs for a two pulse pump-probe experiment. These correspond to **a** Ground state bleach, **b** Stimulated emission, and **c** Excited state absorption.

excited state absorption are shown in figure 3.4. It should be noted that these pump-probe signals are independent of the phase and wave-vector relation between the first two interactions, where in 2DES the signal carries that phase. These pump-probe signals are usually emitted in a 2DES experiment as well, and their lack of phase and wave-vector dependence allows them to be separated from the 2DES signal. This separation is done with appropriate phase-cycling [8, 7] in the pump-probe geometry or through wave-vector selection in BOX-CARs [9].

3.1.2 Implementation of 2DES

The total molecular response function is a sum of all possible pulse interactions, $R = \sum R_i$. The signal field could be emitted in various directions given by phase-matching conditions for a particular experimental geometry. For example, a common approach is the so-called box-CARS geometry, which uses 3 beams travelling along the corners of a square, as in figure 3.5a. At the sample location they are overlapped, and the signal is emitted along appropriately phase-matched directions. These are given by the sums over \vec{k} , several of them are shown in figure 3.5b. The rephasing signals are emitted in $\vec{k}_r = -\vec{k}_1 + \vec{k}_2 + \vec{k}_3$. Non-rephasing signals are emitted in $\vec{k}_{rr} = \vec{k}_1 - \vec{k}_2 + \vec{k}_3$. The Local oscillator is a fourth beam travelling along \vec{k}_r that interferes with the signal beam at a fixed delay for phase retrieval.

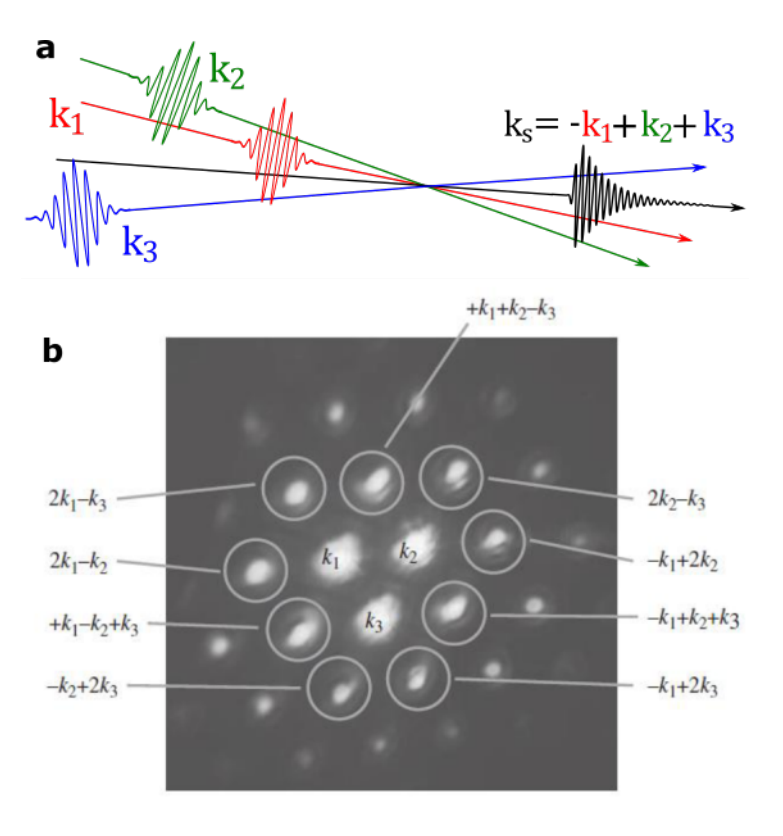


Figure 3.5: Experimental geometry and phase matching for box-CARS 2DES. **a** Beam geometry for box-CARS. **b** Phase-matched signals that come out of a box-CARS beam setup. Adapted from *Concepts and Methods of 2D Infrared spectroscopy*

An alternative geometry for performing 2DES is in the pump-probe geometry. Here only two beamlines are used, and the first two pulses travel along the same path. The delay between these two is imparted via pulse shapers, giving an additional degree of control over the relative phase between the pulses [7]. Here $\vec{k}_1 = \pm \vec{k}_2$ so rephasing and non-rephasing signals travel along the same direction, and co-linearly with \vec{k}_3 . This makes the third pulse along \vec{k}_3 serve as the local oscillator, simplifying experimental setups. To isolate the 2DES signal from regular pump-probe contributions phase-cycling is required. In it's most simple implementation the relative phase, between pulses 1 and 2, $\Delta\phi_{12}$, is cycled between 0 and π at every time step. Because the 2DES signal is sensitive to the phase of the fields, taking the difference between these two signals yields the 2DES signal, free from pump-probe artifacts.

It is even possible to perform 2DES in a fully collinear geometry [10]. This can be through an action detected signal such as a photocurrent [10], photoelectrons [11], or fluorescence [12, 13]. The 2DES signal is isolated either through phase cycling [12, 11, 8] or through frequency selection [14]. In the frequency domain, each beam has a small additional frequency Ω of several 10's of MHz added to the optical frequency of \sim 400 THz. The 2DES signal is then detected with a lock-in detector at the mixed frequency $\Omega_{det} = \Omega_1 - \Omega_2 + \Omega_3$, as in equation 3.28.

$$\omega_1 = \omega_0 + \Omega_1 \tag{3.24}$$

$$\omega_2 = \omega_0 + \Omega_2 \tag{3.25}$$

$$\omega_3 = \omega_0 + \Omega_3 \tag{3.26}$$

$$\omega_{2DES} = \omega_1 - \omega_2 + \omega_3 \tag{3.27}$$

$$=\omega_0 + \Omega_1 - \Omega_2 + \Omega_3 \tag{3.28}$$

An extension to fully collinear optically detected experiments was made by group member Hélène Seiler, who isolated rephasing and non-rephasing signals through appropriate phase-cycling schemes in an optically detected fully collinear experiment [8], without a pure action detected signal. This has the advantage of simplicity; there is no need to find time zero, spatial overlap, or characterize pulses from several beamlines. This implementation of 2DES can also be used in microscopy, or with samples with very low quantum yield for either photocurrents or photo-luminescence.

It is often convenient to look at the system response function as a frequency-frequency plot at a fixed population time $T=t_3-t_2$. This is done through Fourier transform of the signal along $\tau=t_2-t_1$ and t_3 . Often, the Fourier transform along t_3 is done by a spectrometer before detecting the entire spectrum on a linear or array CCD.

The coherence time t_1 is scanned at fixed t_2 , and the resulting coherence is Fourier transformed along t_1 to yield $\tilde{S}(\omega_1,t_2,\omega_3)$. This mathematical process is depicted in figure 3.6. Figure 3.6a shows the pulse sequence and the phase evolution of the signal along the labelled time coordinates. Figure 3.6b shows the detected spectrum after phase cycling, along coherence time $\tau=t_2-t_1$. This is a hybrid time-frequency domain implementation of 2DES. The signal along the detection energy axis is measured in the frequency domain, while the coherence energy axis is measured in the time domain and mathematically Fourier-transformed to obtain the coherence energy. Entirely time domain methods exist [12], as do entirely frequency domain methods [15]. The spectrum in figure 3.6b oscillates with the frequency of the pumped transitions, and absorptive signals will be π out of phase with bleached signals. After Fourier transform along the coherence time axis, the 2D spectrum in figure 3.6c is obtained. This particular spectrum shows one strong diagonal peak, one weak diagonal peak, and two cross peaks. The sample is a CdSe quantum dot with a first excitonic transition at 2.05 eV and a second excitonic transition at 2.15 eV. These energies correspond to the diagonal and cross-peaks, as one would expect.

Some of the things to look for in a two-dimensional spectrum are shown in figure 3.7. For a system of two coupled oscillators as shown in figure 3.7a, researchers may wish to know how the strength of their coupling, and rates of population relaxation between these two. Both of these effects are hidden in linear spectroscopy, 3.7b. 2DES shows couplings directly as cross-peaks in the spectrum. These are the green circles in figure 3.7c, greatly simplifying analysis. Population transfer rates are also clear in 2DES. As the population time increases, population transfer occurs toward lower energy states, figure 3.7d. This can be directly tracked in 2DES by taking several spectra at individual population times, figure 3.7e. It is also possible to Fourier transform the data along t_2 , to look at oscillations and coherences along t_2 . This is particularly powerful, as you can view which states couple to which frequencies, e.g. this provides a direct map to which electronic states couple most strongly to which phonons, and also tracks the relative phase of those phonons as a function of inital state [3].

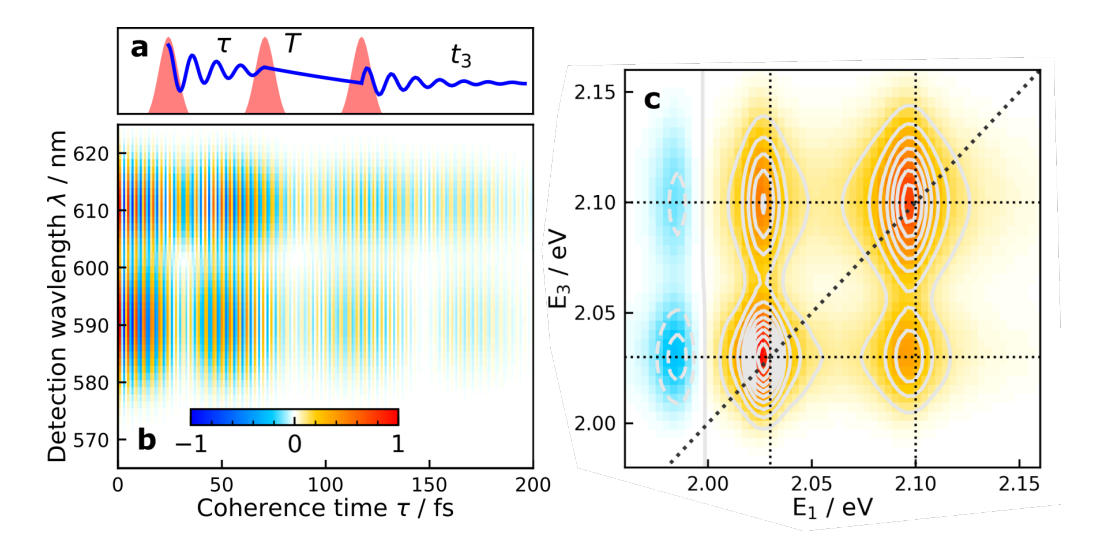


Figure 3.6: Acquiring the 2DES signal for a hypothetical system of 2 coupled oscillators with an excited state absorption. **a** Pulse sequence and signal evolution in 2DES. **b** Coherence along t_1 after dispersion by a grating. **c** 2DES spectrum after Fourier transform along t_1 , showing resonant energies on the diagonal, coupling on the anti-diagonal, and excited state absorption in blue.

One very important role for 2DES is in observing lineshape dynamics to understand electron-phonon coupling. This is shown in figure 3.7 \mathbf{e} and \mathbf{f} . The lineshape in 2DES has a diagonal and anti-diagonal component. The diagonal component is the total lineshape that should be observed in linear spectroscopy. The anti-diagonal component is an instantaneous distribution of frequencies, that at time $t_2 = 0$ is the homogeneous linewidth. As population time increases the sample has time to explore other configurations, or interact with the bath. This results in the anti-diagonal linewidth increasing as the system undergoes spectral diffusion. This process can be tracked through time, and allows for a direct reconstruction of the frequency-frequency correlation function.

3.1.3 Electronic vs Vibrational Coherence

It is not a strict rule that the signal along t_2 decay as a monotonic population relaxation. There are several pathways that can create oscillatory signals along t_2 that arise from

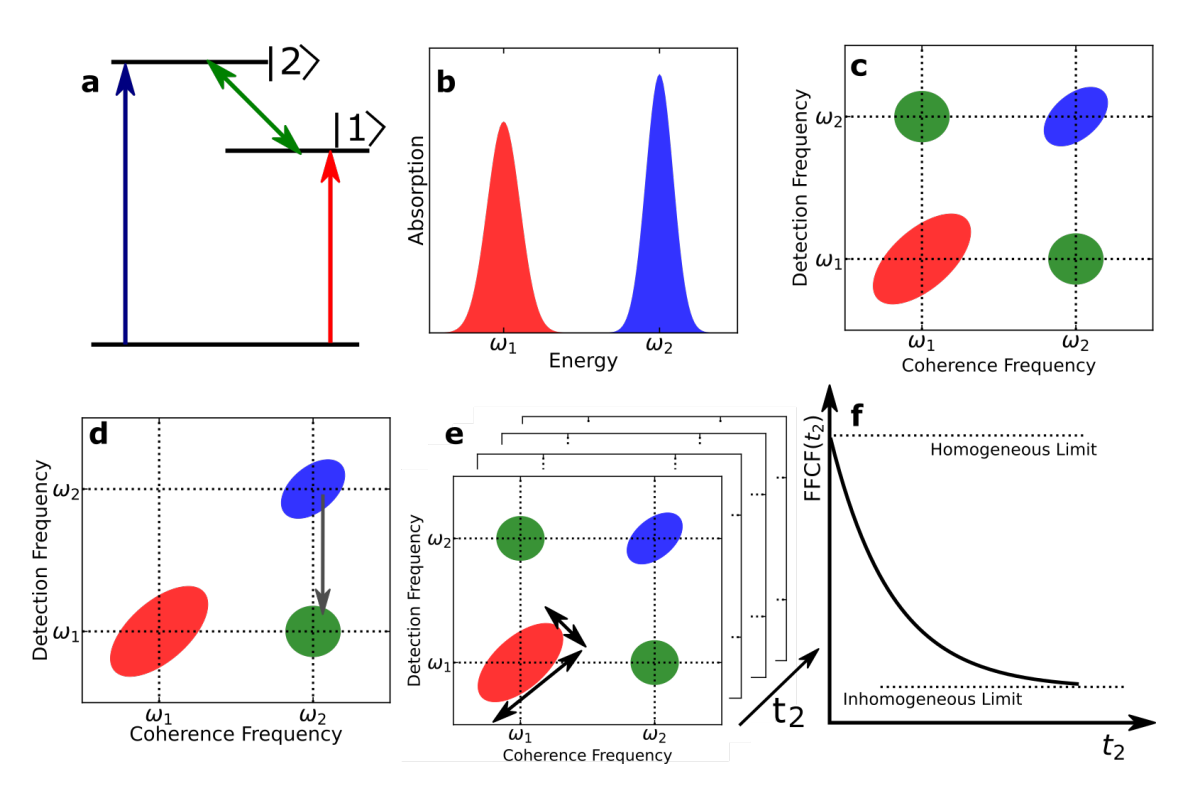


Figure 3.7: Capabilities of 2DES **a** Two coupled oscillators that are probed by 2DES. **b** In linear spectroscopy, coupling and dynamic information is hidden. **c** 2DES provides a direct measure of coupling, **d** Population relaxation, and **e** lineshape dynamics. **f** This can be used to reconstruct the frequency fluctuation correlation function.

either vibrational or electronic coherence. For example, when vibrational fine structure is taken into account, the coarse electronic structure in figure 1.4b is dressed with a ladder of states separated by the vibrational frequency. For CdSe systems, the most important vibrational mode is the LO phonon at 208 cm⁻¹, or 26 meV. States will be labelled $|n, \nu\rangle$ where n refers to the electronic state and ν the vibrational state. Any DSFD that has a term of type $|n, \nu\rangle\langle n, \nu \pm 1|$ after the second pulse will produce a signal that oscillates along t_2 with the phonon frequency. Such a DSFD is shown in figure 3.8a. Another possibility for oscillations along t_2 are electronic coherences. These can be either a double quantum coherence, with oscillations at $\approx 2\omega_{01}$, or at an arbitrary frequency determined by the spacing between electronic energy states. We will first describe the former, so called two quantum or double quantum coherences. This is depicted in figure 3.8b. In this case there is the possibility of doing two interactions in a row on the ket to create a $|2\rangle\langle 0|$

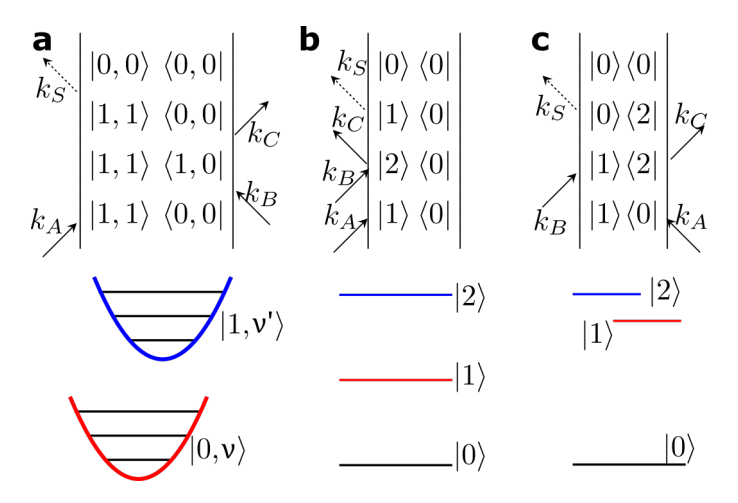


Figure 3.8: Examples of coherent oscillations along t_2 for several systems. **a** With vibrational structure, oscillations arise from coherences between vibrational states. **b** So-called two-quantum coherences arise after two interactions on the bra or ket in a row. **c** oscillations along t_2 can also be due to two closely spaced electronic energy levels.

coherence, that oscillates at roughly $2\omega_{01}$. There is also the equivalent sequence on the bras. Finally, there are purely electronic coherences between closely spaced electronic states. These are shown in figure 3.8c. In this case the oscillation frequency is simply the difference in energy between state $|1\rangle$ and $|2\rangle$. The two-quantum coherence is usually well resolved, because of its very high oscillation frequency, for example in [16]. The difference between electronic beats and vibrational coherences are more subtle, as these two could have nearly degenerate frequencies. By looking at the pathways that give birth to either of these coherences it is possible to create coherence maps that have different shapes and phase relations depending on the nature of the coherence, as in figure 3.9 [3].

The question of coherences is interesting because it has consequences in quantum computing and sheds light on atomistic dephasing mechanisms. Vibrational coherences illustrate the nature of electron-phonon coupling. The coherence time of the vibrational oscillatory signal reflects either coherent phonons or bound polarons. Prominent scientists have also made claims that quantum coherence can improve the transport of charges in biological photosystems [17, 18, 19, 20]. These results have spawned several

studies supporting [21] and attacking [22] the initial claims. Other groups have attempted to extend these debated results in biological photosynthesis to organic photovoltaics [23], leading to public debates in leading journals [24, 25]. This heated debate has even caused editors of leading journals to comment in their publications' news sections [26]. Aspects of this scientific controversy have also appeared in mainstream science news [27, 28].

Vibrational coherences have unambiguously been detected for as long as ultrafast spectroscopy has existed as a science [29]. Electronic coherences are much more difficult to detect due to their fast dephasing times, quite often highly ordered systems at cryogenic temperatures are necessary [30]. What is debated regarding the question of coherences in biological systems is their nature, electronic or vibrational. Vibrational coherences are nothing new or novel, but electronic coherences in these disordered systems at room temperature, as some have claimed to observe [31], would be extraordinary from a materials science perspective. Multidimensional spectroscopy is a powerful tool for disentangling electronic and vibrational coherences, as these should have different oscillation frequencies along t_2 , and also different phase relations as you move along the (E_1,E_3) surface [32, 3]. To observe so called coherence maps, the population transfer and static signals must be removed from the 2D spectrum, $S(E_1, t_2, E_3)$. This can be done through a global analysis with minimum parameters [3], or more often, an exponential function is fit along the t_2 dimension and subtracted. The residuals are then Fourier transformed along t_2 to obtain $\tilde{S}(E_1, E_2, E_3)$. Two theoretical coherence maps are shown in figure 3.9, for E_2 = 25 meV. Electronic coherence arises from a beating between two closely spaced electronic states, the frequency of this oscillation is given by the energy spacing between those levels. The amplitude of these oscillations in a 2DE spectrum are shown in figure 3.9a. Here the sample is a model system that could be a CdSe quantum dot with a band edge of 1.94 eV, and the two closely-spaced energy levels could be the first two excitonic states, $|1S_e1S_{3/2}\rangle$ and $|1S_e2S_{3/2}\rangle$. Two lobes are evident, separated along E_3 . These two lobes oscillate out of phase, as shown in figure 3.9b. Vibrational coherences are shown in figure 3.9c and d. These oscillations are due to wavepacket movement along the ground

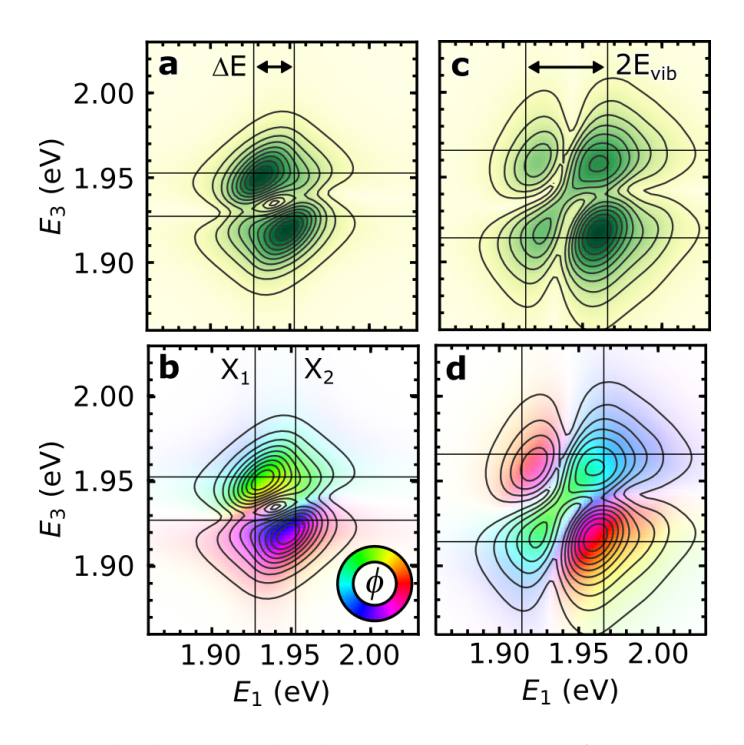


Figure 3.9: Electronic and vibrational coherences in 2DES for a model system. **a** Amplitude and **b** phase maps of electronic coherence at the coherence frequency. **c** Amplitude and **d** phase maps for vibrational coherences at the vibrational frequency. Reproduced from [3]

and excited state PES. In CdSe QDs this vibrational structure arises from the LO phonon at 24 meV. As the wavepacket moves, wavefunction overlap with the ground state PES oscillates at the same frequency. The vibrational coupling map has 4 lobes, separated by twice the phonon energy along E_1 and E_3 .

By altering the pump energy the excited state wavefunction will be launched with a different phase. By altering the probe wavelength, the excited state wavefunction will be detected at a different phase, leading to strong phase dependence of the coherences along E_1 and E_3 . This is shown in figure 3.9d. Oscillations along the diagonal, $E_1 = E_3$, are out of phase with those along the anti-diagonal. This is because vibrational coherences arise form a frequency modulation of the absorption at a particular energy, whereas electronic coherences between two closely spaced states are simply a beat frequency.

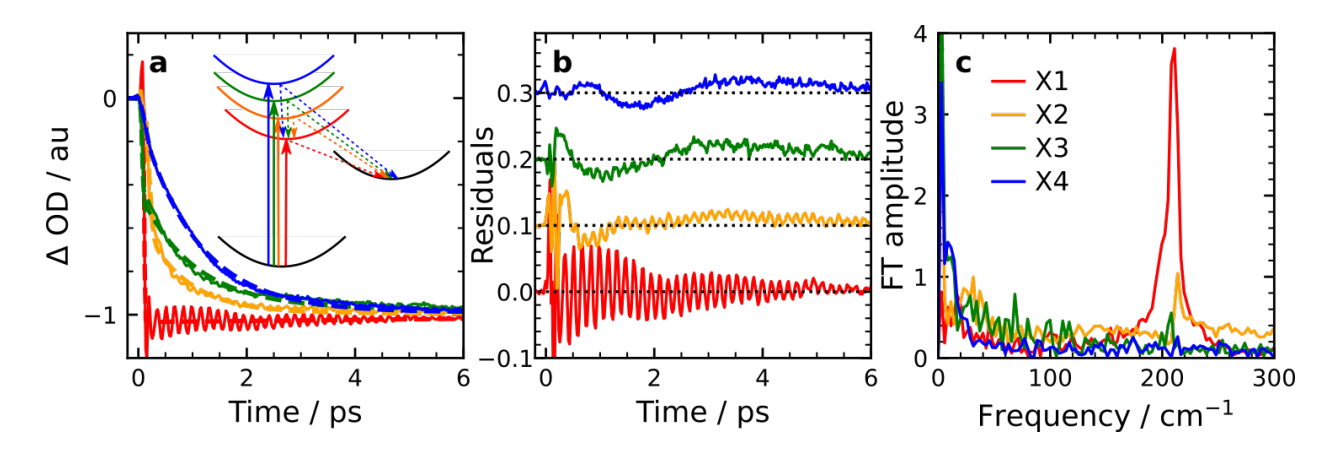


Figure 3.10: SRPP measurement of coherent phonons in graded-shell CdSe/CdSe $_x$ Zn $_{1-x}$ S QDs. **a** Total response after pumping into one of several excitonic states. schematic: Excitonic states depicted as displaced harmonic oscillators coupled to a trap state. **b** Residuals of each trace in **a** after fitting to model functions. **c** Fourier transform of residuals reveals the state-resolved electron-phonon coupling spectrum.

SRPP is another powerful tool for examining vibrational coherences, but due to trade-offs between the required time resolution and state-specificity it can be difficult to observe electronic coherences with SRPP. Furthermore, the broader the bandwidth used to pump or probe a vibrational coherence, the more the overall signal is blurred due to averaging over several phases of the coherence signal[3]. The power of SRPP is again its simplicity and its state specificity. An example SRPP phonon measurement is shown in figure 3.10. The system here is a CdSe quantum dot (QD) with an overgrown graded alloy shell, $CdSe/CdSe_{1-x}ZnS_x$, where x goes from zero to 1 radially away from the CdSe core. This system is very much decoupled from the QD surface[33]. After ultrafast electronic excitation into one of four excitonic states (X1-X4) in figure 3.10a, the total response of the electronic and nuclear systems is probed at the red edge of the band edge exciton. The schematic in figure 3.10a shows the quantum system used to model the nuclear response, a model of displaced harmonic oscillators. Each of the excitonic states is coupled to a surface state. The surface states are responsible for acoustic phonons [34].

The electronic response in figure 3.10 is removed by modelling the electronic response as a decaying exponential to an offset value. The residuals from this process are shown in figure 3.10b, showing prominent oscillations at high and low frequencies. The Fourier transform of these results are shown in figure 3.10c. The large peak at \sim 208 cm⁻¹ corresponds to the LO phonon in CdSe. It is clear that band edge pumping into X1 has the largest coupling to LO phonons, while higher excitation couples more to low frequency LA phonons, as would be expected[35]. These methods have been used to study complex mixed CdTe_{1-x}Se_x quantum dot systems that display a rich phonon structure[36].

3.2 Broadband sources for 2DES

One important limit in 2DES is the bandwidth of the source; this simultaneously limits temporal resolution and the states that can be examined. To enable pulse compression, the source must have a well-behaved and predictable spectral phase. For measurements across several coherence and population times, the source must be stable in overall intensity and spectral shape as well. In our lab, a typical 2DES spectrum at one population time can take on the order of 10 minutes. To properly sample some 50 population times, the source must therefore be stable for \sim 8 hours or more. Researchers have been steadily advancing the spectral width, intensity, and simplicity of broadband sources over the last 30 years. Notable techniques are high-harmonic generation [37], structured photonic crystal fibers [38], non-collinear optical parametric amplification (NOPA)[39], and hollow-core fibres (HCFs)[40]. Only these last two techniques will be discussed, as they are the most commonly used in ultrafast spectroscopy of nanomaterials.

3.2.1 NOPAs

Non-collinear optical parametric amplifiers (NOPAs) are a development of optical parametric amplifiers (OPAs) that increases the phase-matching bandwidth in optical parametric generation. This allows NOPAs to cover large parts of the electromagnetic spectrum[39, 41], producing sub-10 fs optical pulses. NOPAs have been developed to work in the visible [39], IR [42]. Through subsequent sum-frequency generation NOPAs have enabled tunable broadband UV pulses [43]. In typical OPAs, the input beam is split into 2 beams, a seed with very low intensity and a pump at high intensity. The low intensity seed path is used to generate a continuum through self-phase modulation in a transparent material. This white-light seed will contain frequencies spanning ~ 450 -1600 nm. The seed is overlapped in time and space with the high-energy pump for optical parametric amplification in a non-linear crystal. Here the seed takes energy from the pump in a $\chi^{(2)}$ process with $\omega_p = \omega_s + \omega_i$, where ω_p , ω_s , and ω_i refer to the pump, signal, and idler frequencies respectively. For an 800 nm input beam this can generate a signal beam in the range of \sim 1150-1600 nm and an idler beam in the range \sim 1600 - 2600 nm. For increased power, sometimes a second amplification stage is performed where the signal and idler beams are combined with the fundamental to further amplify output pulse energies. Through downstream frequency doubling and mixing, OPAs have been used to generate ultrafast pulses spanning the UV to the far IR. OPAs are now available in off the shelf devices configured to specific amplifier systems, whether it be Ti:Sapph with short, high energy pulses at 800 nm, or fiber based systems with high rep rates and lower pulse energies and fundamental wavelengths in the IR.

The signal and idler wavelengths produced by an OPA are determined by phase-matching in the non-linear parametric medium. For efficient $\chi^{(2)}$ processes to occur, the fundamental and signal beams must travel through the crystal at the same phase velocity. If there is a phase velocity mismatch, newly generated signal and idler radiation will be out of phase with the previously generated radiation, resulting in destructive interference

and reduced output. The phase-matching condition is stated mathematically as:

$$\Delta k = k(\omega_p) - k(\omega_s) - k(\omega_i) \tag{3.29}$$

This condition is very rarely met in most materials. In order to fulfill the condition specified by equation 3.29, elements of the $\chi^{(2)}$ tensor that couple orthogonal polarizations are necessary. In such a geometry, one beam will be polarized along one axis of a birefringent crystal, while the other two will be polarized along an orthogonal axis. For a certain incidence angle, the refractive indices along these optical axes will satisfy equation 3.29 at the desired frequency.

The approach outlined above works well for narrow-band frequency matching of a collinear pump and signal beam. It is this principle that allows for wavelength tuning of the OPAs in our downstairs, SRPP spectroscopy lab. The phase-matching bandwidth of the process in equation 3.29 is determined by crystal thickness and group velocity mismatch. By limiting crystal thickness, there will be smaller phase mismatch at the end of the crystal, but also less amplification of the seed beam. As seed amplification scales as L^2 , with L the crystal length, this is not an ideal solution for generating broadband pulses.

In order to consider broadband phase matching, it is useful to Taylor expand equation 3.29 about ω_s . By conservation of energy, if the signal changes from ω_s to $\omega_s + \delta \omega_s$, the idler frequency will change to $\omega_i - \delta \omega_i$. We will also consider a fixed pump frequency ω_p .

$$\Delta k = k(\omega_{p})$$

$$- \left[k(\omega_{s}) + \frac{\partial k}{\partial \omega} \Big|_{\omega_{s}} \delta \omega_{s} + \frac{\partial^{2} k}{\partial \omega^{2}} \Big|_{\omega_{s}} \delta \omega_{s}^{2} + \dots \right]$$

$$- \left[k(\omega_{s}) - \frac{\partial k}{\partial \omega} \Big|_{\omega_{i}} \delta \omega_{s} + \frac{\partial^{2} k}{\partial \omega^{2}} \Big|_{\omega_{i}} \delta \omega_{s}^{2} + \dots \right]$$

$$\approx \Delta k_{0} - \left(\frac{\partial k}{\partial \omega_{s}} + \frac{\partial k}{\partial \omega_{i}} \right) \delta \omega_{s}$$
(3.30)

In going from equation 3.30 to 3.31, we have dropped the higher order terms and used $\Delta k_0 = k(\omega_p) - k(\omega_s) - k(\omega_i)$. Here, it is clear that for broad bandwidth gain both terms in equation 3.31 must be zero. If the first term is non-zero the phase mismatch will be off and very little amplification will occur. If the second term is non-zero, only a narrow range of frequencies will be amplified. Matching the second terms of equation 3.31 is often referred to as group velocity matching, since the group velocity of the pulse is $(\partial k/\partial \omega)^{-1}$. To simultaneously obtain phase matching and group velocity matching, the solution is again to use birefringent crystals and off-diagonal elements of the $\chi^{(2)}$ tensor. To achieve the conditions set by equation 3.31 both the angle of incidence of the pump beam and the pump-seed crossing angle must be optimized [39, 41]. To make a visible NOPA from an 800 nm input beam, the pump must first be doubled to 400 nm. The 400 nm pump is crossed with a white-light continuum in BBO at an internal angle of 3.7°, which corresponds to approximately 6° going into the BBO from air. If the BBO is cut at an angle $\theta = 32^\circ$, one of the beams should be going straight through the crystal and very little angle tuning of the BBO is necessary.

The geometry of a typical NOPA is shown in figure 3.11. Figure 3.11**a** shows the beam layout and placement of crystals. Figure 3.11**b** shows the NOPA output spectrum, covering $\sim 520\text{-}800$ nm. The schematic in figure 3.11**b** shows a trick for ensuring the WL seed and the 400 nm pump are at the proper crossing angle: under sufficient pump

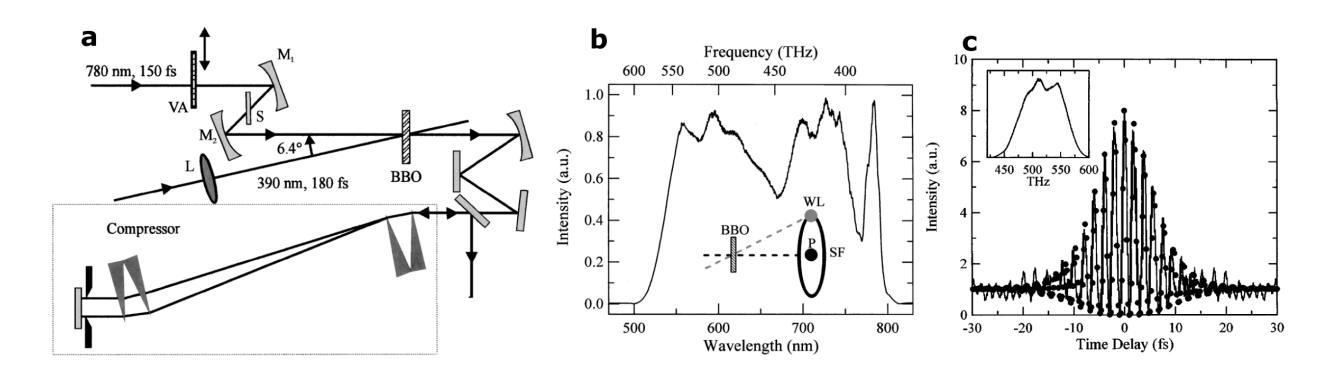


Figure 3.11: Geometry and pulse characteristics of a NOPA. **a** Geometry of a NOPA and external compressor. **VA** variable attenuator, **S** Sapphire. **b** Output spectrum with broadband phase matching. **WL** white-light seed, **SF** super-fluorescence cone **c** auto-correlation trace of the compressed NOPA output. inset: Spectrum of the compressed pulse. Figures reproduced from [44]

intensity spontaneous optical parametric generation creates a cone of white light around the pump beam (labelled SF in figure 3.11 b). If the seed crosses the pump beam and the cone, then the you have the right crossing angle. Figure 3.11c further shows a collinear auto-correlation trace of the compressed pulse. This pulse has a sech² FWHM of less than 8 fs.

The NOPA principle of operation leads to powerful broadband pulses, and can be used to create sub-10 fs pulses across the visible spectrum. Care must be taken to ensure the white-light seed and the pump beam have good overlap in time. Without compensation, the pump beam is often much shorter than the seed, so must be chirped in order to amplify the entire spectrum. For high-power applications, there is the additional issue of pulse front tilt and walk-off between the beams, which can be compensated through careful use of prisms or gratings[45].

3.2.2 Hollow-core fibres

Gas filled hollow-core fibres (HCFs) have been explored as continuum sources somewhat in parallel with the development of NOPAs. Early results were promising, showing sub-10 fs capability in the late 90's [40, 46], comparable to NOPAs of the time. While NOPAs covered more of the visible wavelengths, HCFs were fundamentally centered around the wavelength of the driving pulse. Despite this limitation, through high gas pressures and long fibre lengths, HCF setups have been developed that cover the entire visible regime [9, 47]. The system is overall easier to align and harder to damage due to the nature of the nonlinear medium; it is rather difficult to "burn" an ideal gas. This has led to high average power and high peak power implementations of HCFs [48].

The principle of operation in gas-filled HCFs is self-phase modulation (SPM). The goal is to have strong SPM while simultaneously avoiding plasma generation through multi-photon ionization. One common strategy is to use a large diameter fiber to avoid high intensity in a tight focus. Because SPM will be reduced in a larger diameter fiber, this is compensated with a longer fiber length. This is part of the motivation behind the Kambhampati labs' choice of a 2 meter, $400~\mu m$ diameter fiber. Due to the simple model, the pulse propagation through the fiber can be modelled numerically with very good precision. Additional details on the modelling can be found in chapter 6. These accurate models have allowed for simple, predictable dispersion compensation through transmission in a material with anomalous dispersion [49] or with chirped mirrors [48].

Bibliography

- [1] Mukamel, S. Principles of Nonlinear Optical Spectroscopy; Oxford University Press, 1995.
- [2] Hamm, P.; Zanni, M. T. Concepts and Methods of 2D Infrared spectroscopy; Cambridge University Press, 2011.
- [3] Palato, S.; Seiler, H.; Nijjar, P.; Prezhdo, O.; Kambhampati, P. *Proceedings of the National Academy of Sciences of the United States of America* **2020**, 117, 0–6.
- [4] Do, T. N.; Khyasudeen, M. F.; Nowakowski, P. J.; Zhang, Z.; Tan, H. S. *Chemistry An Asian Journal* **2019**, *14*, 3992–4000.
- [5] Nemeth, A.; Milota, F.; Mančal, T.; Lukeš, V.; Kauffmann, H. F.; Sperling, J. *Chemical Physics Letters* **2008**, 459, 94–99.
- [6] Stone, K. W.; Turner, D. B.; Gundogdu, K.; Cundiff, S. T.; Nelson, K. A. Accounts of Chemical Research 2009, 42, 1452–1461.
- [7] Shim, S.-H.; Zanni, M. T. Phys. Chem. Chem. Phys. **2009**, 11, 748–761.
- [8] Seiler, H.; Palato, S.; Kambhampati, P. Journal of Chemical Physics 2017, 147.
- [9] Ma, X.; Dostál, J.; Brixner, T. Optics Express 2016, 24, 20781.
- [10] Nardin, G.; Autry, T. M.; Moody, G.; Singh, R.; Li, H.; Cundiff, S. T. *Journal of Applied Physics* **2015**, *117*.

- [11] Aeschlimann, M.; Brixner, T.; Fischer, A.; Kramer, C.; Melchior, P.; Pfeiffer, W.; Schneider, C.; Strüber, C.; Tuchscherer, P.; Voronine, D. V. *Science* **2011**, *333*, 1723–1726.
- [12] Tian, P.; Keusters, D.; Suzaki, Y.; Warren, W. S. *Science* **2003**, *300*, 1553–1555.
- [13] Tekavec, P. F.; Lott, G. A.; Marcus, A. H. Journal of Chemical Physics 2007, 127, 1–22.
- [14] Langbein, W.; Patton, B. Optics Letters 2006, 31, 1151.
- [15] Decamp, M. F.; Tokmakoff, A. Optics Letters 2006, 31, 113–115.
- [16] Brosseau, P.; Palato, S.; Seiler, H.; Baker, H.; Kambhampati, P. *The Journal of chemical physics* **2020**, 153, 234703.
- [17] Engel, G. S.; Calhoun, T. R.; Read, E. L.; Ahn, T. K.; Mančal, T.; Cheng, Y. C.; Blankenship, R. E.; Fleming, G. R. *Nature* **2007**, *446*, 782–786.
- [18] Fleming, G. R.; Scholes, G. D.; Cheng, Y.-C. *Procedia Chemistry* **2011**, *3*, 38–57.
- [19] Scholes, G. D.; Mirkovic, T.; Turner, D. B.; Fassioli, F.; Buchleitner, A. *Energy and Environmental Science* **2012**, *5*, 9374–9393.
- [20] Collini, E.; Wong, C. Y.; Wilk, K. E.; Curmi, P. M.; Brumer, P.; Scholes, G. D. *Nature* **2010**, *463*, *644–647*.
- [21] Arsenault, E. A.; Yoneda, Y.; Iwai, M.; Niyogi, K. K.; Fleming, G. R. *Nature Communications* **2020**, *11*, 1–8.
- [22] Cao, J.; et al. Science Advances 2020, 6, eaaz4888.
- [23] Kaake, L. G.; Moses, D.; Heeger, A. J. Journal of Physical Chemistry Letters 2013, 4, 2264–2268.
- [24] Mukamel, S. Journal of Physical Chemistry A 2013, 10563–10564.

- [25] Kaake, L. G.; Moses, D.; Heeger, A. J. Journal of Physical Chemistry A 2013, 408700.
- [26] Ball, P. Nature Materials **2018**, 17, 220.
- [27] Biello, D. Scientific American **2010**.
- [28] Mandelbaum, R. Gizmodo 2020.
- [29] Bowman, R. M.; Zewail, a. H. Chem. Phys. Lett. 1989, 161, 297–302.
- [30] Dong, S.; Trivedi, D.; Chakrabortty, S.; Kobayashi, T.; Chan, Y.; Prezhdo, O. V.; Loh, Z. H. Nano Letters 2015, 15, 6875–6882.
- [31] Panitchayangkoon, G.; Hayes, D.; Fransted, K. A.; Caram, J. R.; Harel, E.; Wen, J.; Blankenship, R. E.; Engel, G. S. *Proceedings of the National Academy of Sciences* **2010**, 107, 12766–12770.
- [32] Seibt, J.; Pullerits, T. Journal of Physical Chemistry C 2013, 117, 18728–18737.
- [33] Walsh, B. R.; Saari, J. I.; Krause, M. M.; Nick, R.; Coe-Sullivan, S.; Kambhampati, P. *The Journal of Physical Chemistry C* **2015**, *119*, 16383–16389.
- [34] Saari, J. I.; Dias, E. A.; Reifsnyder, D.; Krause, M. M.; Walsh, B. R.; Murray, C. B.; Kambhampati, P. *Journal of Physical Chemistry B* **2013**, *117*, 4412–4421.
- [35] Sagar, D. M.; Cooney, R. R.; Sewall, S. L.; Dias, E. A.; Barsan, M. M.; Butler, I. S.; Kambhampati, P. *Physical Review B Condensed Matter and Materials Physics* **2008**, *77*, 1–14.
- [36] Bragas, A. V.; Aku-Leh, C.; Costantino, S.; Ingale, A.; Zhao, J.; Merlin, R. *Physical Review B Condensed Matter and Materials Physics* **2004**, *69*, 1–11.
- [37] Corkum, P. B.; Rolland, C.; Srinivasan-Rao, T. *Physical Review Letters* **1986**, *57*, 2268–2271.
- [38] Gérôme, F.; Jamier, R.; Auguste, J.-l.; Humbert, G.; Blondy, J.-m. **2010**, *35*, 1157–1159.

- [39] Wilhelm, T.; Piel, J.; Riedle, E. Optics Letters 1997, 22, 1494.
- [40] Nisoli, M.; De Silvestri, S.; Svelto, O. Applied Physics Letters 1996, 68, 2793–2795.
- [41] Brida, D.; Manzoni, C.; Cirmi, G.; Marangoni, M.; Bonora, S.; Villoresi, P.; De Silvestri, S.; Cerullo, G. *Journal of Optics A: Pure and Applied Optics* **2010**, 12.
- [42] Brida, D.; Bonora, S.; Manzoni, C.; Marangoni, M.; Villoresi, P.; Silvestri, S. D.; Cerullo, G. *Opt. Express* **2009**, *17*, 12510–12515.
- [43] Varillas, R. B.; Candeo, A.; Viola, D.; Garavelli, M.; Silvestri, S. D.; Cerullo, G.; Manzoni, C. Opt. Lett. **2014**, *39*, 3849–3852.
- [44] Cerullo, G.; Nisoli, M.; Stagira, S.; De Silvestri, S. Optics Letters 1998, 23, 1283.
- [45] Tzankov, P.; Zheng, J.; Mero, M.; Polli, D.; Manzoni, C.; Cerullo, G. *Optics Letters* **2006**, *31*, 3629.
- [46] Nisoli, M.; De Silvestri, S.; Svelto, O.; Szipöcs, R.; Ferencz, K.; Spielmann, C.; Sartania, S.; Krausz, F. *Optics Letters* **1997**, 22, 522.
- [47] Son, M.; Mosquera-Vázquez, S.; Schlau-Cohen, G. S. Optics Express 2017, 25, 18950.
- [48] Spokoyny, B.; Koh, C. J.; Harel, E. Optics Letters 2015, 40, 1014.
- [49] Béjot, P.; Schmidt, B. E.; Kasparian, J.; Wolf, J. P.; Legaré, F. *Physical Review A Atomic, Molecular, and Optical Physics* **2010**, *81*, 2–7.

Chapter 4

CdSe / CdS Dots-in-Rods as a Gain

Medium

Semiconductor quantum dots have been well investigated for their favorable optical properties in applications spanning lasers [1, 2, 3], light emitting diodes [4, 5], and photovoltaics [6, 7, 8]. Spherical quantum dots represent the model system for these studies, with well understood exciton dynamics [9]. The results on these model systems form a basis for how fundamental excitonics may be controlled via materials towards improved performance for optical applications. Hence there has been much work to explore more complex nanocrystal geometries such as core/shell structures[10], nanorods[11, 12, 13], or nanoplatelets[11, 14, 15, 16]. The aim is to see how the material system can control specific properties such as efficiency, Auger rates, and multiexciton interaction energies.

4.1 Introduction

There are three properties commonly used to characterize a gain material. These are the lifetime, threshold, and cross-section for gain. The lifetime is determined by the lifetime

of the upper lasing state. In the case of multiexcitons this is the Auger lifetime, which is on the order of 1-100 ps. For single excitons the lifetime is on the order of 10 ns, one of the motivations for single exciton gain materials. While the lifetime is an important parameter, it is not the determinant of efficiency. Efficiency is determined by the detailed level structure in the material and the presence of interfering absorbing states. While a shorter lifetime will never lead to a more efficient laser, a well designed system can mitigate this effect. If the laser radiation in the cavity builds up quickly to a large enough value, stimulated emission can become favored over population decay. This can occur in a small cavity with a densely packed medium. Any excited state absorption from the upper lasing level will always be a source of loss whatever is happening in the cavity, and is hence a more stringent determinant of efficiency in terms of lasing applications.

Because of the equivalency between the Einstein coefficients for absorption and stimulated emission, population inversion between two levels is necessary for light amplification to occur. This is only possible in a three or more level system. Three level systems will produce gain only when the ground state is half-empty, while a four-level system with the proper decay channels will in theory produce gain after a single excitation. Figure 1 shows some of the energy levels implicated in NC lasing. II-VI NCs form a three-level system between the ground state and the absorptive X_{abs} and emissive X_{em} states of the band edge exciton, which are separated by the Stokes' shift, δ_X . Gain would occur between the emissive exciton state and the ground state once the ground state is half empty. In practice, there is an interfering state that blocks gain. Absorption of a second photon can excite a second exciton, forming a biexciton (XX).

The biexciton is bound by an energy Δ_{XX} , placing biexciton absorption to the red of single exciton absorption. Because Δ_{XX} is similar to δ_{X} , excited state absorption overlaps stimulated emission, blocking gain and destroying the ideal three level system. As there is fine structure in X, there should be fine structure in XX as well. This structure may come from axial strain, exchange interactions, or phonon vibrations [17, 18], the

important thing is that the fine structure is present in both X and XX. Figure 4.1 shows how these energy levels are related. This fine structure leads to several ways of measuring the binding energy, $\Delta_X X$, either in emission or absorption. It is the overlap of X_{em} and XX_{abs} that dictate thresholds for single exciton gain and the overlap of XX_{em} with X_{abs} and XX_{abs} that dictate thresholds for biexciton gain.

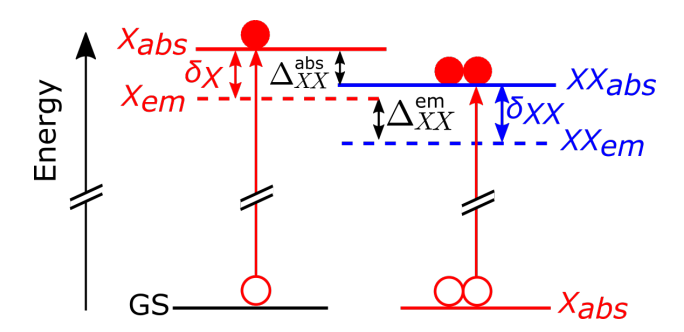


Figure 4.1: Energy level diagram showing absorptive and emissive states for the exciton and biexciton in quantum confined systems.

4.2 CdSe/Cds Dot-in-Rods

Semiconductor NCs have a number of favorable characteristics as an optical gain medium, but no single platform exists with ideal performance in all respects. Hence an understanding of the relationship between structure and function is useful. One aims for a material with decoupled emission and excited state absorption, which can be achieved through multiexciton interaction. This is very large in small NCs, but small NCs also have very fast Auger rates and suffer from surface trapping[19, 20]. Shape control can alter some gain properties. Comparing CdSe quantum dots to quantum rods with the same volume, rods will have a shorter Auger lifetime due to surface trapping effects[13, 21]. Despite this, it is possible to achieve room temperature optical gain in CdSe quantum rods[22]. Another approach is to form a heterostructure that spatially separates the electron and hole, as in a type-II core/shell NC. Here multiexciton interactions are extremely large and repulsive, due to Coulomb interactions between the excited and separated elec-

tron and hole. Long lived gain from single excitons is achieved in these systems[23]. Type-II heterostructures, however, suffer from reduced oscillator strength in the lasing transition. Another avenue for low-threshold gain is to take advantage of trap states to form a three-level [24] or a four-level system[25]. CdSe dots with an overgrown CdS rod (CdSe/CdS DiRs) offer both low threshold gain[26, 27, 28], reduced Auger rates [29, 30], and polarized emission [31, 32, 33]. These useful gain properties may be due to electron delocalization in the conduction band, which is controlled by the relative diameters of the CdSe dot and the CdS rod [34, 35, 36], providing a promising platform for optical applications such as lasers[37, 38, 39, 40] or LEDs[41, 42]. Previous ultrafast pump-probe studies on DiRs have already made some key obesrvations. Lupo et. al. specifically did a state-resolved approach that found evidence for electron delocalization in the conduction band[43]. Others assigned the features in the pump-probe spectrum to the CdS surface, CdSe/CdS interface states, and CdSe dot, and found relaxation rates between these three states[44, 45]. We present here a comprehensive, state-resolved pump-probe analysis of the gain characteristics of this system.

Figure 4.2 presents an overview of the CdSe/CdS DiR nanocrystals used here and their optical properties. All optical measurements are performed on DiRs dissolved in toluene at room temperature. Figure 4.2 **a** shows a schematic of the physical structure. Figure 4.2 **b** shows some of the important energy levels. The inset shows TEM images of the DiRs. The rods have dimensions of approximately 5 nm × 45nm. Figure 4.2 **c** gives an overview of the linear and non-linear optical spectra. The linear absorption spectrum shows two important features, one relatively weak absorption due to the CdSe quantum dot near 2.07 eV, and a large absorption near 2.58 eV due to the rod. Based on CdSe quantum dot sizing curves, the dot diameter is approximately 4.6 nm, not taking into account the delocalizing effect of the CdS shell[45]. Both the dot and the rod show quantized, excitonic states. Under optical excitation into the rod photoluminescence is observed from the dot. Also shown are pump pulse spectra under two pumping conditions; pumping into the dot (2.07 eV, in red) and pumping into the rod (2.58 eV, in blue) excitonic states.

Below is a TA spectrum at 10 ps after pumping into the dot excitonic state at 2.07 eV. The TA spectrum shows a strong bleach of the dot transition and a weaker bleach of the rod transition, with other very weak bleach signals occurring between these two states.

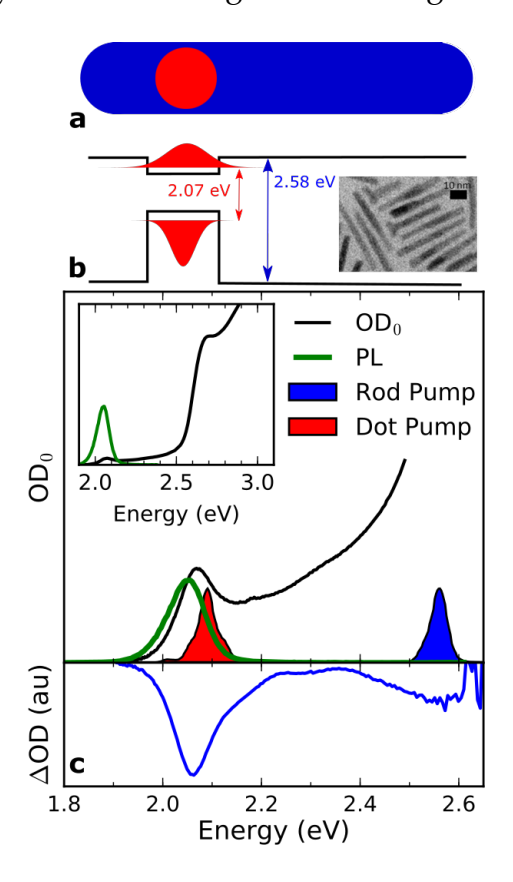


Figure 4.2: Linear absorption, emission, and pump-probe spectrum of the CdSe/CdS Dotin-Rod (DiR) system. **a** Schematic of the DiR system. **b** Energy level diagram showing dot and rod band structures. Inset:TEM image of the DiRs. **c** Linear absorption, PL, pump spectra and Δ OD spectrum of the DiRs. inset: PL and absorption showing rod absorption and dot emission..

The photo-luminescent properties of this CdSe/CdS DiR system demonstrate high photo-luminescent quality. Figure 4.3 shows single crystal emission data giving evidence for bright, nearly non-blinking emission. Figure 4.3 **a** shows the sample emission time trace obtained over 3 minutes of observation. It is clear that the system is spending most of its time in a bright state with high emission, with intermittent blinking for very

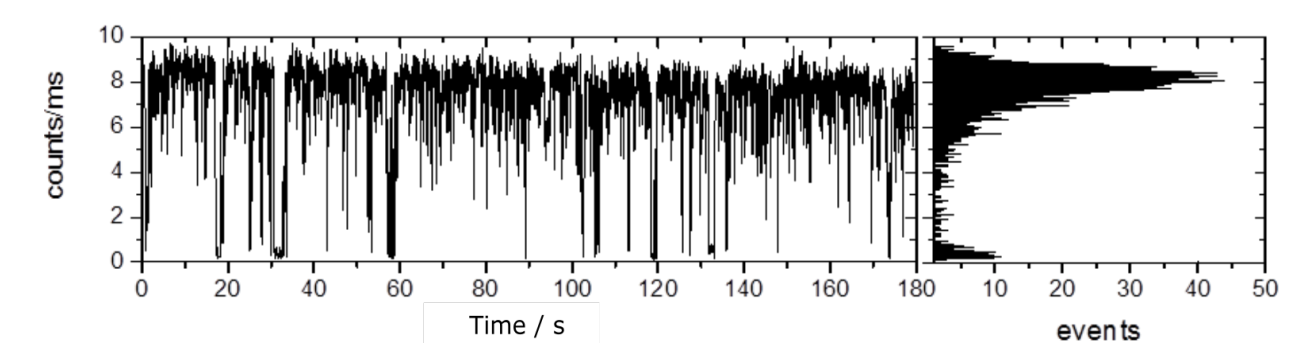


Figure 4.3: Single crystal emission data for CdSe/CdS DiRs. **a** Emission time trace showing bright and dark states. **b** Histogram of data presented in **a**.

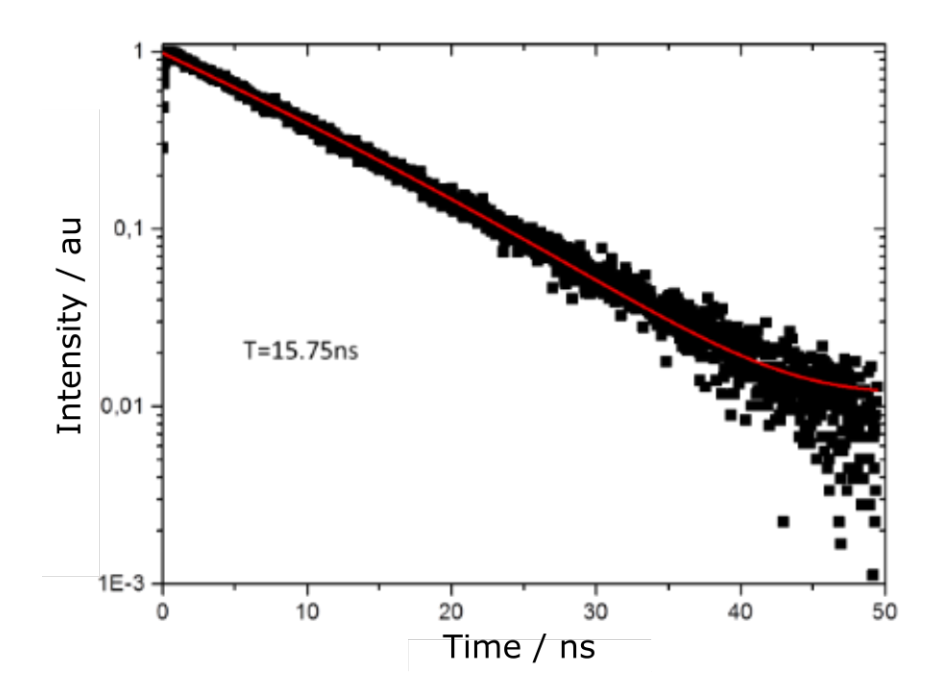


Figure 4.4: Population decay of a single CdSe/CdS DiR crystal.

brief periods of time. The amount of time spent in bright and dark states is quantified in figure 4.3 **b**, in a histogram of emission rates rates at each time interval.

With the data presented in figure 4.3 it is possible to build a fluorescence decay curve to obtain the lifetime of excitons in a single DiR system. This is shown in figure 4.4. A population lifetime of 15.75 ns is obtained with a clean, mono-exponential decay.

Figure 4.5 provides a more detailed overview of the excitonic state-resolved TA measurements. Figure 4.5 **a** and **b** show the different results obtained by specifying the

initial excitonic state, compared to the linear absorption spectrum. By pumping resonantly into the dot transition at 2.07 eV, an instrument response-limited bleach signal is created that doesn't change over ~ 100 ps. By pumping into the rod continuum at 3 eV, an initially hot exciton is created in the rod that then diffuses into the dot on a timescale of several 100s of fs, causing a growth in the bleach feature at 2.07 eV. There is also a stronger bleach signal in the 2.15 to 2.25 eV region compared to 2.07 eV pumping, which has been assigned in the literature to bleaching of a "bulge" state at the CdSe/CdS interface [46, 44] or quantum confined hole states in the CdSe dot [47]. Figure 4.5 c and d show the full energy and time resolved TA signal for dot (2.07 eV) and rod (3.0 eV) pumps, respectively. Figure 4.5 d further shows excited state absorption due to transitions from X \Rightarrow XX. Pumping resonantly into the rod state at 2.58 eV yields similar results to pumping into the rod continuum at 3 eV.

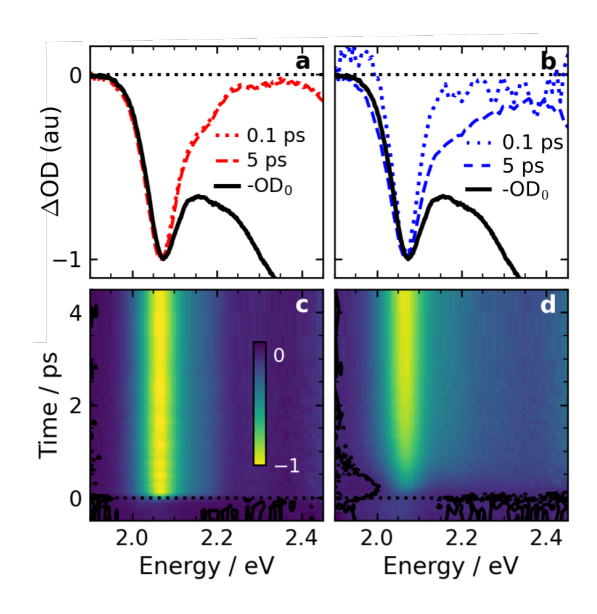


Figure 4.5: Overview of state-resolved pump-probe measurements in CdSe/CdS DiRs. **a,b** Linear absorption and transient spectra for pumping into **a** the dot and **b** the rod. **c,d** Full time and energy resolved SRPP signals for **c** dot pumping and **d** rod pumping

4.3 Gain Measurements

Figure 4.6 shows the development of optical gain via state-resolved pumping. The Kambhampati group has previously shown that state-resolved optical pumping reveals new aspects of gain physics, specifically these state-resolved methods demonstrate how cross-section, threshold, and bandwidth are intimately related to the pumped state[48]. We explore these effects here. Figure 4.6 **a,b** shows the development of optical gain through the nonlinear absorption spectrum. The nonlinear absorption spectrum is simply the linear absorption spectrum plus the transient absorption spectrum, $OD_{NL} = \Delta OD + OD_0$. The nonlinear absorption corresponds to the absorption of the pumped sample. These nonlinear absorption spectra are obtained at a time delay of 10 ps. Certain transitions in the pumped sample become bleached, ultimately producing transparency. At higher fluence one might obtain negative absorption corresponding to gain.

Figure 4.6 **a** shows the nonlinear absorption after pumping into the dot at 2.07eV. Gain is achieved from approximately 1.93 to 2.07 eV. Gain coefficients are also relatively large compared to the linear absorption cross-section. Figure 4.6 **b** shows the same measurement after pumping into the rod at 2.58 eV. At high fluence the gain extends from 1.93 to 2.03 eV. The gain is also much weaker relative to dot-pumped DiRs, and the shape of the gain spectrum is markedly different. The advantage of pumping into the rod state is that the threshold fluence is much lower. Gain is achieved at \sim 250 nJ/pulse for rod pumping and \sim 690 nJ/pulse for dot pumping. This is due to the funnel effect of the rod; the rod can very effectively absorb photons and transport charge to the dot for stimulated emission.

Figure 4.6 **c,d** shows the gain threshold for dot pump and rod pump. The key point is establishing the average number of excitons per DiR, $\langle N \rangle$. This is done by measuring the population of band edge excitons through the magnitude of the band edge bleach[49]. Since the band edge state can hold at most two excitons, the population is

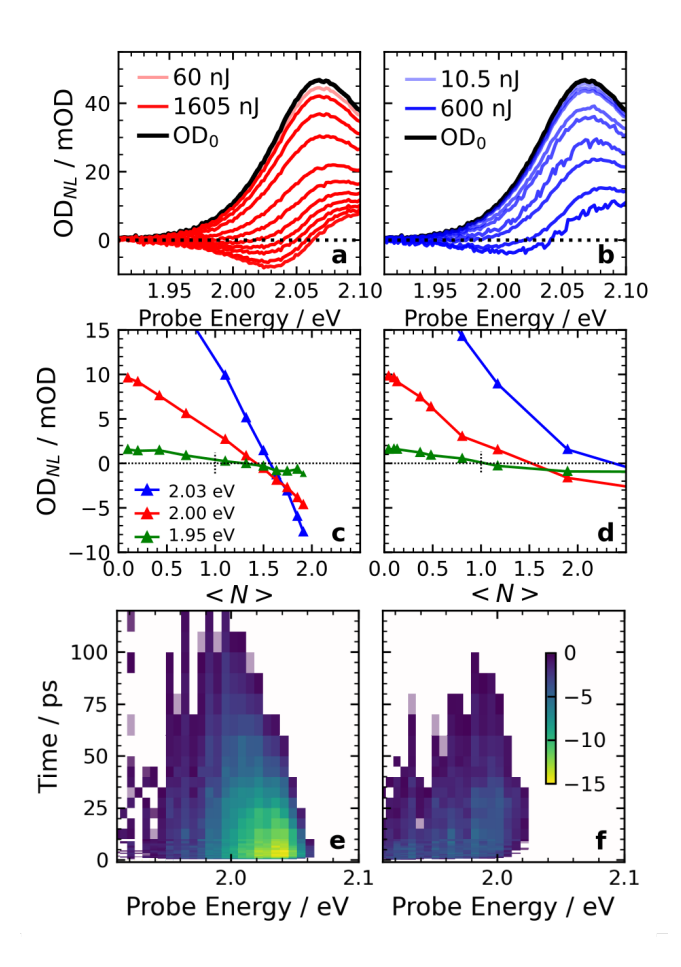


Figure 4.6: State-resolved gain properties of the CdSe/CdS DiR system, for pumping into the dot (left column) or rod (right column) excitonic states. **a,b** Non-linear optical density with increasing pump fluence for **a** dot and **b** rod pump. **c,d** Slices along selected probe energies of OD_{NL} , showing lower thresholds for rod pumping. **e,f** Time and energy resolved gain signal. Colorbar scale is in mOD.

simply twice the fractional bleach as given by equation 4.1 [48, 28].

$$\langle N_{dot} \rangle = -2 \frac{\Delta OD}{OD_0} = \langle N \rangle$$
 (4.1)

For pumping directly into the dot at 2.07eV only the dot state is populated, so $\langle N_{dot} \rangle = \langle N \rangle$. For pumping into the rod at 2.58 eV any number of excitons can be created in a single NC because of the high density of states at this energy. The number of NCs containing N excitons is given by a Poisson distribution with parameter $\langle N \rangle$. By relating

the number of NCs containing two excitons to that given by a Poisson distribution, the average exciton occupancy can be extracted. This is given by equation 4.2 [48, 49, 28]

$$\langle N_{dot} \rangle = -2 \frac{\Delta OD}{OD_0} = 2 - (2 + \langle N \rangle) e^{-\langle N \rangle}$$
 (4.2)

The gain threshold in terms of the average exciton occupancy is a measure of gain efficiency and exciton and biexciton overlap. For decoupled stimulated emission and excited state absorption, gain thresholds will be small. When stimulated emission competes with excited state absorption, gain thresholds will be larger. This results in a spectrum for the gain threshold. Figure 4.6c shows the threshold for dot pumping is $\langle N \rangle = 1.2$ on the red edge, and $\langle N \rangle = 1.6$ at the peak of gain. Figure 4.6d shows the threshold for rod pumping is $\langle N \rangle = 1.0$ at the red edge, and $\langle N \rangle = 1.6$ at the peak. A threshold of $\langle N \rangle = 1.6$ is approximately universal for CdSe NCs [50]. What is unique here is the low threshold for high pump energies. Previous studies that report only ASE [26, 51] or lasing [37, 39, 38, 40] thresholds miss valuable information that can only be found through pump-probe experiments, as reported here. These are the average exciton occupancy at the gain threshold, the gain spectrum and the gain lifetime. These state-resolved measurements allow observation and quantitative measurement for all of these properties.

Figure 4.6**e**,**f** further shows that both pumps yield gain that lasts up to 100 ps. The dynamics of optical gain can be connected to the lifetime of multiexcitons (MX). The lifetime of MX is determined by Auger recombination. If gain is produced by single excitons, MX recombination is of no relevance to the gain lifetime. Here MX recombination is the limiting factor for gain lifetime.

4.4 Surface coupling

Coupling between the surface states of a quantum dot (QD) and the core band edge exciton has several effects. There is obviously decreased PL quantum yield from the band edge exciton, but there is also often white light emission that competes with core emission [52, 53]. This white light emission is thought to originate from the surface of the QD because it is only apparent for smaller QDs, and is quite sensitive to capping ligands. Other experimental measures that show surface coupling include phonon spectra and Auger recombination. For poorly passivated or aged samples large LA phonons are created through surface trapping[54, 55], while well-passivated samples show little to no LA phonon amplitude when pumping the band edge exciton[56]. Phonon spectra after resonant dot pumping of the DiRs are shown in figure 4.7. Following a process similar to that described in section 3.1.3, The total lattice plus electronic response of the system is shown in figure 4.7a at two probe energies, 2.05 eV and 2.03 eV. The response was modelled as an exponential decay to an offset value.

Under close inspection, a phase shift between the oscillations in figure 4.7 can be discerned. This is expected, given the origin in these signals in motion along vibrational manifolds. Similar results showing a phase shift with detection energy has been seen in bare CdSe nanocrystals [57, 58, 59], and calculations based on Huang-Rhys coupling clearly demonstrate this pump energy phase-dependance [60]. The residuals from the TA signal were Fourier transformed to yield the phonon spectra, which are shown in figure 4.7b and c, for 2.05 and 2.03 eV probes respectively. For CdSe/CdS DiRs the phonon power spectrum largely consists of a single peak at ~208 cm⁻¹, the LO phonon frequency of bulk CdSe. For aged or photo-treated samples, the acoustic phonon is quite prominent, especially after pumping higher lying excitonic states [58]. This shows good overall surface passivation for the DiR system. The phase shift is also apparent in figure

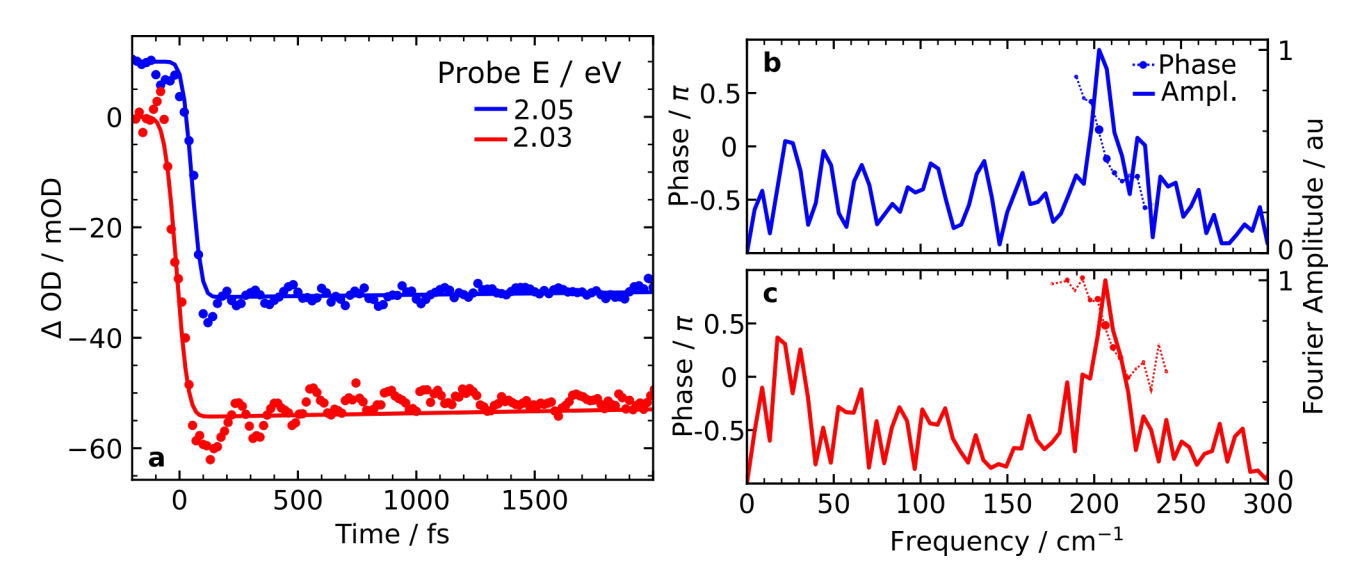


Figure 4.7: Phonons in CdSe/CdS DiRs. **a** The total response for two probe energies (2.03 and 2.05 eV) and the fit model. Data are offset for clarity. **b**,**c** Fourier transforms of the fit residuals. Both probe energies show a large peak near 208 cm⁻¹, but there is a $\pi/2$ phase difference between probe wavelengths.

4.7, for a probe energy of 2.05 eV the phase is approximately 0 at 208 cm⁻¹, while for 2.03 eV probing the phase is approximately $\pi/2$.

Figure 4.8 shows a measurement of exciton-exciton interactions in the Auger recombination rate. This rate is determined, to a certain extent, by the CdSe-CdS interface[61] and delocalization of the electrons in the conduction band [29]. Figure 4.8a shows the recombination kinetics after pumping into the dot (2.07 eV). Signals are normalised to -1 at 250 ps delay. Under increasing pump fluence a fast decay component grows in that reflects the higher proportion of XX relative to X in the sample. The bleach signals were globally fit to a single exponential decay with an offset, and the amplitudes of these components are shown in the inset. The Auger lifetime was found to be 125 ps. With pumping directly into the dot only XX recombination kinetics are probed, since no higher MX can be created due to the two-fold degeneracy of the conduction band electronic state. The data in figure 4.8a shows the ideal response of a system with two-fold degeneracy [62].

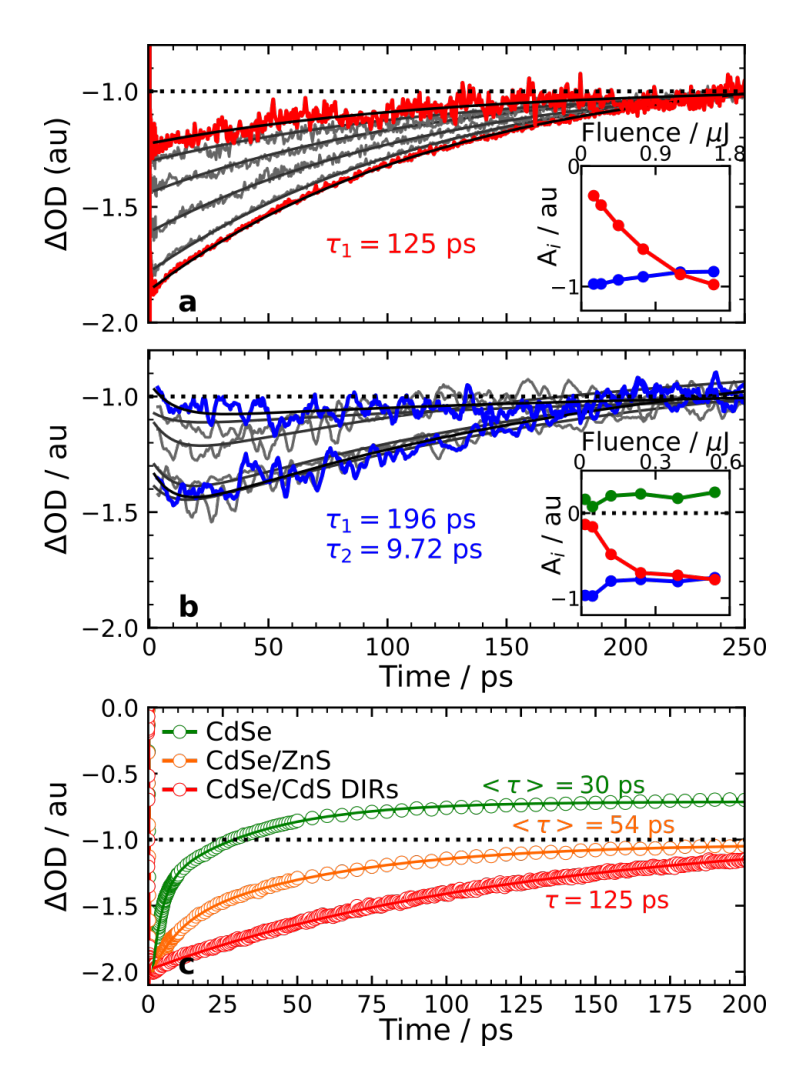


Figure 4.8: Auger recombination of biexcitons show good surface passivation in CdSe/CdS DiRs. **a** Pumping into the dot creates either a single exciton or a biexciton, with a lifetime of 125 ps. **b** Pumping into the rod can create any number of higher multiexcitons, leading to more complicated kinetics. insets of **b,c**: Power dependence of fit amplitudes, with blue an offset term, red the slow component, and green the fast component. **c** Auger recombination across CdSe samples.

Figure 4.8b shows the Auger recombination kinetics with rod pump (2.58 eV). The most notable point is that with rod pump decays are no longer monoexponential. The data are well fit by a biexponential with an offset. Because the first excited state can only hold 2 excitons, recombination of higher MX will not be reflected in the signal. The buildup time is nominally the decay time of higher MX, as XXX decays to XX for example.

This can lead to different results for Auger lifetimes than what would be observed for pumping into the first excitonic state, as the main decay component here has a lifetime of nearly 200 ps. Again, the inset shows the amplitudes of the various fitting components.

Figure 4.8c shows Auger rates across CdSe samples. In each case the core CdSe dot has roughly the same band edge exciton energy. The samples are pumped at high fluence to saturate the biexciton state. Signals are normalized such that the maximum bleach is -2. Probing at the band edge exciton state means the signal is only sensitive to single excitons or biexcitons. For ligand-passivated CdSe, the decay goes from -2 to -0.7, indicating the existence of a surface trapping channel for excitons[62]. The effective decay time is 30 ps. For ZnS capped CdSe, the signal decays from -2 to -1, indicating that the surface is well passivated and no excitons are lost on the way from XX to X. However, the decay is quite fast and remains biexponential. For the CdSe/CdS DiRs studied here, biexciton decay is monoexponential with a time constant of 125 ps, more than twice as long as CdSe/ZnS. The signal also decays from -2 to -1, indicating that no excitons are lost to surface traps. These results show that Auger recombination is highly sensitive to surface conditions and electron-hole overlap.

Figure 4.1 introduced a minimal level structure of the exciton and biexciton. We aim to relate the experimental observations of threshold and bandwidth for gain to an experimental determination of this energy structure. To do this one requires a measurement of absorbing and emitting states of both the exciton and the biexciton. This is enabled by state-resolved TA spectroscopy [63, 64].

Figure 4.9 shows a measurement of biexciton structure. The energy of X_{abs} is measured by linear absorption. Emission from X_{em} is measured by PL. The difference between these two is the well known exciton Stokes' shift, δ_X . Absorption into XX_{abs} is measured by Δ OD, the transient absorption spectrum. The Δ OD spectrum has three terms, ground state bleach, stimulated emission, and excited state absorption (ESA). ESA

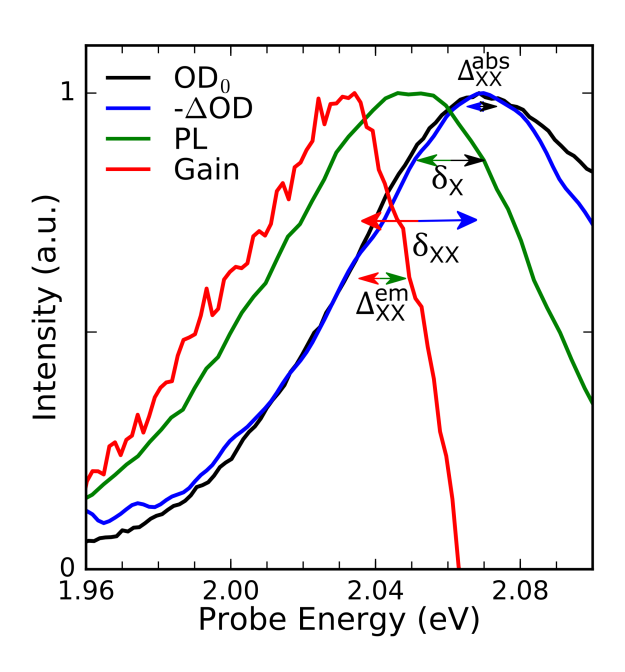


Figure 4.9: Energetics of states involved in gain revealed by linear and non-linear spectroscopies for CdSe/CdS DiRs.

occurs form X_{abs} to XX_{abs} , causing the ΔOD spectrum to shift relative to the linear spectrum by Δ_{XX}^{abs} . At high pump fluence, the biexciton is populated. Stimulated emission contributions to the ΔOD signal will be from XX_{em} . This results in the gain spectrum being shifted relative to the PL spectrum by Δ_{XX}^{em} . The combination of these measurements allows the full reconstruction of the energy levels presented in figure 4.1. Just as there is an exciton Stokes' shift, there is a biexciton Stokes' shift, δ_{XX} . Results of these measurements are summarised in table 4.1, with analogous results for CdSe NCs [63] and CdSe/Cd,Zn,S graded alloy NCs [65] from previous work. Apparent here are the reduced binding energies in emission and absorption, and the particularly small XX Stokes' shift. Other groups have also shown that biexciton binding energies can range from \sim 40 meV to -30 meV, placing biexciton emission to the red or blue of exciton emission depending on the relative size of the dot and rod[35, 28]. To the authors' knowledge, negative binding energies have not been observed in bare CdSe NCs.

Sample	δ_X / meV	Δ_{XX}^{abs} / meV	Δ_{XX}^{em} /meV	δ_{XX} / meV
CdSe ($R = 2.1 \text{ nm}$)	25	12	44	57
CdSe (R = 2.8 nm)	16	9	37	45
CdSe/Cd, Zn , $S(R = 2.1 nm)$	30	3	30	57
DiRs ($R = 2.3 \text{ nm}$)	22	-1	12	36

Table 4.1: Results of biexciton structure measurements across CdSe QD samples.

In conclusion, it has been shown that low threshold gain under both dot pumping and rod pumping conditions is possible in CdSe/CdS DiRs. This is in contrast to CdSe quantum dots and quantum rods, which show little or no gain for pumping into excited states [22, 48]. Electron delocalization in the conduction band has consequences on the Auger recombination rate, which is much smaller in this system than in ligand-passivated CdSe or type-I CdSe/ZnS core/shell quantum dots. Electron delocalization has further implications on the electronic structure of the biexciton. This work shows the potential of the CdSe/CdS DiR system as a platform for light emitting applications.

Bibliography

- [1] Adachi, M. M.; Fan, F.; Sellan, D. P.; Hoogland, S.; Voznyy, O.; Houtepen, A. J.; Parrish, K. D.; Kanjanaboos, P.; Malen, J. A.; Sargent, E. H. *Nature Communications* **2015**, *6*, 1–8.
- [2] Fan, F.; et al. Nature 2017, 544, 75-79.
- [3] Dang, C.; Lee, J.; Breen, C.; Steckel, J. S.; Coe-Sullivan, S.; Nurmikko, A. *Nature Nanotechnology* **2012**, *7*, 335–339.
- [4] Anikeeva, P. O.; Halpert, J. E.; Bawendi, M. G.; Bulovic, V. *Nano Letters* **2009**, *9*, 2532–2536.
- [5] Caruge, J. M.; Halpert, J. E.; Wood, V.; Bulović, V.; Bawendi, M. G. *Nature Photonics* **2008**, *2*, 247–250.
- [6] Sargent, E. H. *Nature Photonics* **2012**, *6*, 133–135.
- [7] Lee, Y.-L.; Lo, Y.-S. Advanced Functional Materials **2009**, 19, 604–609.
- [8] Pattantyus-Abraham, A. G.; Kramer, I. J.; Barkhouse, A. R.; Wang, X.; Konstantatos, G.; Debnath, R.; Levina, L.; Raabe, I.; Nazeeruddin, M. K.; Grätzel, M.; Sargent, E. H. ACS Nano 2010, 4, 3374–3380.
- [9] Kambhampati, P. J. Phys. Chem. C 2011, 115, 22089–22109.
- [10] Hines, M. A.; GuyotSionnest, P. Journal of Physical Chemistry 1996, 100, 468–471.

- [11] Cunningham, P. D.; Souza, J. B.; Fedin, I.; She, C.; Lee, B.; Talapin, D. V. *ACS Nano* **2016**, *10*, 5769–5781.
- [12] Mohamed, M. B.; Burda, C.; El-Sayed, M. A. Nano Letters 2001, 1, 589–593.
- [13] Htoon, H.; Hollingsworth, J. A.; Dickerson, R.; Klimov, V. I. *Physical Review Letters* **2003**, *91*, 1–4.
- [14] Tessier, M. D.; Javaux, C.; Maksimovic, I.; Loriette, V.; Dubertret, B. *ACS Nano* **2012**, *6*, 6751–6758.
- [15] Ithurria, S.; Tessier, M. D.; Mahler, B.; Lobo, R. P. S. M.; Dubertret, B.; Efros, A. L. *Nature Materials* **2011**, *10*, 936–941.
- [16] She, C.; Fedin, I.; Dolzhnikov, D. S.; Dahlberg, P. D.; Engel, G. S.; Schaller, R. D.; Talapin, D. V. ACS Nano 2015, 9, 9475–9485.
- [17] Granados del Águila, A.; Jha, B.; Pietra, F.; Groeneveld, E.; de Mello Donegá, C.; Maan, J. C.; Vanmaekelbergh, D.; Christianen, P. C. M. *ACS Nano* **2014**, *8*, 5921–5931.
- [18] Miscuglio, M.; Lin, M. L.; Di Stasio, F.; Tan, P. H.; Krahne, R. *Nano Letters* **2016**, *16*, 7664–7670.
- [19] Kambhampati, P.; Mack, T.; Jethi, L. ACS Photonics 2017, 4, 412–423.
- [20] Klimov, V. I.; Mikhailovsky, A.; McBranch, D. W.; Leatherdale, C. A.; Bawendi, M. G. *Science* **2000**, 287, 1011–1013.
- [21] Taguchi, S.; Saruyama, M.; Teranishi, T.; Kanemitsu, Y. *Physical Review B* **2011**, *83*, 155324.
- [22] Link, S.; El-Sayed, M. A. Journal of Applied Physics 2002, 92, 6799–6803.
- [23] Klimov, V. I.; Ivanov, S. A.; Nanda, J.; Achermann, M.; Bezel, I.; McGuire, J. A.; Piryatinski, A. *Nature* **2007**, *447*, 441–446.

- [24] Lahad, O.; Meir, N.; Pinkas, I.; Oron, D. ACS Nano 2015, 9, 817–824.
- [25] Geiregat, P.; Houtepen, A. J.; Sagar, L. K.; Infante, I.; Zapata, F.; Grigel, V.; Allan, G.; Delerue, C.; Thourhout, D. V.; Hens, Z. *Nature Materials* 2017 17:1 2017, 17, 35.
- [26] Moreels, I.; Rainò, G.; Gomes, R.; Hens, Z.; Stöferle, T.; Mahrt, R. F. *Advanced Materials* **2012**, 24, OP231–OP235.
- [27] Xing, G.; Liao, Y.; Wu, X.; Chakrabortty, S.; Liu, X.; Yeow, E. K. L.; Chan, Y.; Sum, T. C. ACS Nano 2012, 6, 10835–10844.
- [28] Saba, M.; Minniberger, S.; Quochi, F.; Roither, J.; Marceddu, M.; Gocalinska, A.; Kovalenko, M. V.; Talapin, D. V.; Heiss, W.; Mura, A.; Bongiovanni, G. *Advanced Materials* **2009**, 21, 4942–4946.
- [29] Zavelani-Rossi, M.; Lupo, M. G.; Tassone, F.; Manna, L.; Lanzani, G. *Nano Letters* **2010**, *10*, 3142–3150.
- [30] Rabouw, F. T.; Lunnemann, P.; Van Dijk-Moes, R. J. A.; Frimmer, M.; Pietra, F.; Koenderink, A. F.; Vanmaekelbergh, D. *Nano Letters* **2013**, *13*, 4884–4892.
- [31] Planelles, J.; Rajadell, F.; Climente, J. I. Journal of Physical Chemistry C 2016, 120, 27724–27730.
- [32] Vezzoli, S.; Manceau, M.; Leménager, G.; Glorieux, Q.; Giacobino, E.; Carbone, L.; De Vittorio, M.; Bramati, A. *ACS Nano* **2015**, *9*, 7992–8003.
- [33] Hadar, I.; Philbin, J. P.; Panfil, Y. E.; Neyshtadt, S.; Lieberman, I.; Eshet, H.; Lazar, S.; Rabani, E.; Banin, U. *Nano Letters* **2017**, *17*, 2524–2531.
- [34] Rainò, G.; Stöferle, T.; Moreels, I.; Gomes, R.; Hens, Z.; Mahrt, R. F. *ACS Nano* **2012**, *6*, 1979–1987.
- [35] Sitt, A.; Della Sala, F.; Menagen, G.; Banin, U. Nano Letters 2009, 9, 3470–3476.

- [36] Angeloni, I.; Raja, W.; Polovitsyn, A.; De Donato, F.; Zaccaria, R. P.; Moreels, I. *Nanoscale* **2017**, *9*, 4730–4738.
- [37] Di Stasio, F.; Grim, J. Q.; Lesnyak, V.; Rastogi, P.; Manna, L.; Moreels, I.; Krahne, R. *Small* **2015**, *11*, 1328–1334.
- [38] Zavelani-Rossi, M.; Lupo, M. G.; Krahne, R.; Manna, L.; Lanzani, G. *Nanoscale* **2010**, 2, 931–935.
- [39] Zavelani-Rossi, M.; Krahne, R.; Della Valle, G.; Longhi, S.; Franchini, I.; Girardo, S.; Scotognella, F.; Pisignano, D.; Manna, L.; Lanzani, G.; Tassone, F. *Laser & Photonics Reviews* **2012**, *6*, 678–683.
- [40] Grivas, C.; Li, C.; Andreakou, P.; Wang, P.; Ding, M.; Brambilla, G.; Manna, L.; Lagoudakis, P. *Nature Communications* **2013**, *4*, 2376.
- [41] Rastogi, P.; Palazon, F.; Prato, M.; Di Stasio, F.; Krahne, R. ACS Applied Materials and Interfaces 2018, 10, 5665–5672.
- [42] Castelli, A.; Meinardi, F.; Pasini, M.; Galeotti, F.; Pinchetti, V.; Lorenzon, M.; Manna, L.; Moreels, I.; Giovanella, U.; Brovelli, S. *Nano Lett* **2015**, *15*, 32.
- [43] Lupo, M. G.; Sala, F. D.; Carbone, L.; Zavelani-Rossi, M.; Fiore, A.; Lüer, L.; Polli, D.; Cingolani, R.; Manna, L.; Lanzani, G. *Nano Letters* **2008**, *8*, 4582–4587.
- [44] Wu, K.; Rodríguez-Córdoba, W. E.; Liu, Z.; Zhu, H.; Lian, T. *ACS Nano* **2013**, *7*, 7173–7185.
- [45] Yu, W. W.; Qu, L.; Guo, W.; Peng, X. Chemistry of Materials 2003, 15, 2854–2860.
- [46] Grennell, A. N.; Utterback, J. K.; Pearce, O. M.; Wilker, M. B.; Dukovic, G. Nano Letters 2017, 17, 3764–3774.
- [47] Grazia Lupo, M.; Scotognella, F.; Zavelani-Rossi, M.; Lanzani, G.; Manna, L.; Tassone, F. *Physical Chemistry Chemical Physics* **2012**, *14*, 7420.

- [48] Cooney, R. R.; Sewall, S. L.; Sagar, D. M.; Kambhampati, P. *Physical Review Letters* **2009**, *102*, 1–4.
- [49] Klimov, V. I. Annual Review of Physical Chemistry 2007, 58, 635–673.
- [50] Cooney, R. R.; Sewall, S. L.; Sagar, D. M.; Kambhampati, P. *Journal of Chemical Physics* **2009**, 131.
- [51] Krahne, R.; Zavelani-Rossi, M.; Lupo, M. G.; Manna, L.; Lanzani, G. *Applied Physics Letters* **2011**, *98*, 063105.
- [52] Jethi, L.; Mack, T. G.; Kambhampati, P. Journal of Physical Chemistry C 2017, 121, 26102–26107.
- [53] Krause, M. M.; Mooney, J.; Kambhampati, P. ACS Nano 2013, 7, 5922–5929.
- [54] Saari, J. I.; Dias, E. A.; Reifsnyder, D.; Krause, M. M.; Walsh, B. R.; Murray, C. B.; Kambhampati, P. *Journal of Physical Chemistry B* **2013**, *117*, 4412–4421.
- [55] Tyagi, P.; Cooney, R. R.; Sewall, S. L.; Sagar, D. M.; Saari, J. I.; Kambhampati, P. *Nano Letters* **2010**, *10*, 3062–3067.
- [56] Walsh, B. R.; Sonnichsen, C.; MacK, T. G.; Saari, J. I.; Krause, M. M.; Nick, R.; Coe-Sullivan, S.; Kambhampati, P. *Journal of Physical Chemistry C* **2019**, 123, 3868–3875.
- [57] Palato, S.; Seiler, H.; Nijjar, P.; Prezhdo, O.; Kambhampati, P. *Proceedings of the National Academy of Sciences of the United States of America* **2020**, 117, 0–6.
- [58] Sagar, D. M.; Cooney, R. R.; Sewall, S. L.; Dias, E. A.; Barsan, M. M.; Butler, I. S.; Kambhampati, P. *Physical Review B Condensed Matter and Materials Physics* **2008**, *77*, 1–14.
- [59] Mooney, J.; Saari, J. I.; Myers Kelley, A.; Krause, M. M.; Walsh, B. R.; Kambhampati,P. Journal of Physical Chemistry B 2013, 117, 15651–15658.

- [60] Butkus, V.; Zigmantas, D.; Valkunas, L.; Abramavicius, D. *Chemical Physics Letters* **2012**, *545*, 40–43.
- [61] Cragg, G. E.; Efros, A. L. Nano Letters **2010**, 10, 313–317.
- [62] Tyagi, P.; Kambhampati, P. Journal of Chemical Physics 2011, 134.
- [63] Sewall, S. L.; Franceschetti, A.; Cooney, R. R.; Zunger, A.; Kambhampati, P. *Physical Review B Condensed Matter and Materials Physics* **2009**, *80*, 1–4.
- [64] Klimov, V.; Hunshe, S.; H., K. Physical Review B 1994, 50, 8110–8113.
- [65] Walsh, B. R.; Saari, J. I.; Krause, M. M.; Nick, R.; Coe-Sullivan, S.; Kambhampati, P. *Chemical Physics* **2016**, *471*, 11–17.

Chapter 5

Quantum confinement in bulk-regime Perovskite nanocrystals

Disorder is intrinsic to ionic systems and gives rise to specific electronic processes. In recently developed perovskite ionic crystals, this dynamic lattice disorder is inferred to give rise to material properties, such as defect tolerance. Here, the elementary excitation of interest is the polaron, a localized lattice distortion. In this chapter state resolved pump-probe spectroscopy is used to monitor electron and lattice dynamics in bulk CsPbBr₃ perovskite nanocrystals. The data report spectral lineshape dynamics that monitor the system from optical birth through polaron formation and exciton formation to fully thermalized, confined exciton. The formation of quantum confined excitons arises from the liquid-like polaronic potential, as opposed to physical confinement in conventional CdSe nanocrystals.

5.1 Introduction

Recent interest has arisen in ionic semiconductors, as illustrated by semiconducting perovskites, due to their attractive electro-optical properties [1, 2, 3, 4] such as solar cells [5], LEDs [6], and lasers[7]. In the case of perovskites a key feature is their defect tolerance. This defect tolerance is inferred to be related to the glassy quality of an ionic lattice [8, 9, 10, 11]. As the polar lattice relaxes to accommodate an excited state charge distribution, the excited charges are screened from each other and crystal defects. This screening is thought to be responsible for the impressive performance of perovskite materials[12]. Another important aspect are the nature of defects in perovskite materials; deep trap states are nearly absent[13, 14] and only a small class of point defects exist. However, these point defects are numerous, possibly ~1-2% of atomic sites[4]. In this phonon glass electronic crystal, the elementary excitation of interest is the polaron [15, 16, 17, 18, 19, 20, 21].

The polaron is a localized lattice distortion associated with an electronic excitation. Ionic systems form polarons due to their glassy lattices. The electronic signature of polaron formation has been directly observed in two-dimensional electronic spectroscopy (2DES) of CsPbI₃ nanocrystals[22]. Other evidence for polaron formation comes from hybrid density-functional theory and first principles calculations [16], transport measurements [15, 23], time-resolved X-ray diffraction [24], and direct band mapping through angle-resolved photoemission spectroscopy [25]. Low frequency, overdamped acoustic modes are responsible for the lattice reorganization, and these have been found in low-frequency, temperature dependent Raman spectroscopy [26] across all crystal phases of CsPbBr₃ and CH₃NH₃PbBr₃. However, whether or not polarons are responsible for the impressive performance of perovskite devices is still an open question [27].

In contrast to ionic perovskites, covalent systems couple to the lattice via delocalized phonons [28, 29, 30, 31]. These are grown via hot-injection in a precursor solution[32],

and typically have fewer defects than perovskite NCs. Exactly how the dynamic disorder of ionic semiconductors confers optical and electronic properties is of great contemporary interest.

The salient ideas of electron-lattice coupling spanning covalent to ionic lattices are illustrated in figure 5.1 and figure 5.2. CdSe nanocrystal quantum dots (QDs) present the covalent limit. Their relatively narrow size dispersion and good electronic properties make them an ideal benchmark sample. Their response is shown in figure 5.1a-f. One observes coherent lattice dynamics and the response of a stiff covalent crystal. Figure 5.1a shows the linear spectroscopy of absorption and photoluminescence (PL). With QDs one has pronounced quantum confinement effects apparent in the simple linear spectroscopy, due to physical confinement of the exciton. In covalent QDs, the electronic excitation couples to lattice modes via coherent phonons (figure 5.1b). Illustrated is a polar optical phonon. Figure 5.1c is a schematic showing wavepacket dynamics on the electronic excited state potential energy surface (PES), shown in blue, after photoexcitation from the ground state PES in red. The response is described by normal modes of the crystal: delocalized and coherent. These can be detected in 2DES as a coherent beating of the signal along the diagonal and anti-diagonal linewdiths (figure 5.1d). This can also be detected in state-resolved pump-probe spectroscopy (SRPP) as in figure 5.1e. These normal lattice modes undergo coherent motion which in the frequency domain correspond to well-resolved Lorentzian peaks (figure 5.1f).

The response of ionically-bound soft lattices, such as CsPbBr₃ perovskite nanocrystals (NCs), was recently shown to have isomorphisms[22] with liquid phase solvation dynamics[33, 34]. Figure 5.2a shows the linear absorption and PL of these CsPbBr₃ NCs. The size of these crystals puts them in a bulk size regime, their edge length of 20 nm (inset of figure 5.2a) is significantly greater than the exciton Bohr diameter of 7 nm[35]. Hence, no quantum confinement is evident in the linear spectroscopy. These bulk NCs were chosen to minimize effects from physical confinement.

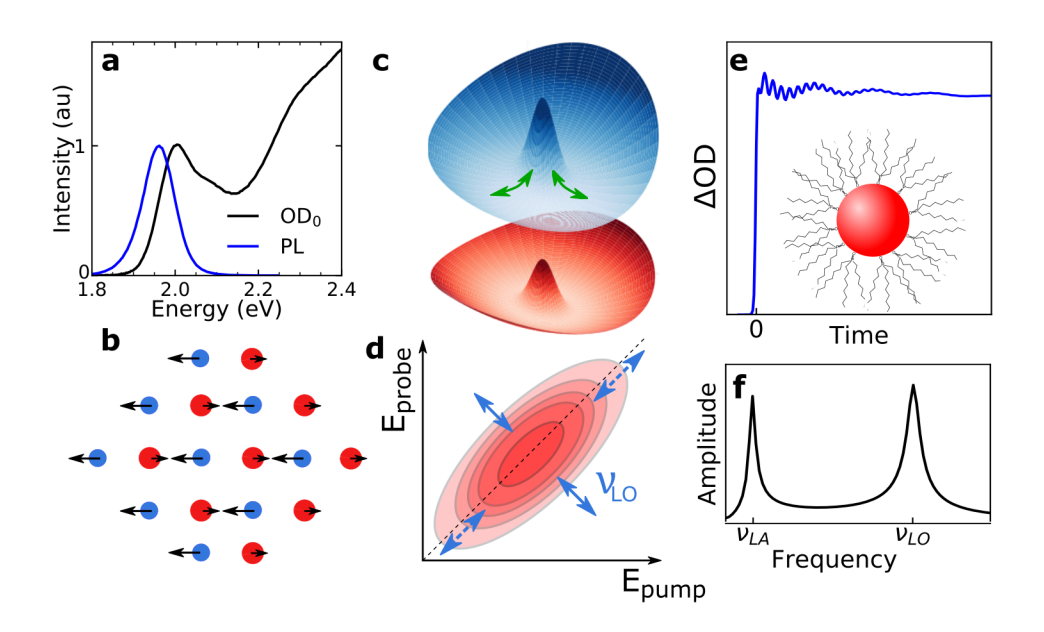


Figure 5.1: Electron-phonon coupling in covalent CdSe **a** Linear absorption and PL in CdSe shows excitonic peaks. **b** Schematic showing coherent optical phonons in the CdSe lattice. **c** These phonons correspond to coherent motion along vibrational coordinates in the upper state PES. **d** In 2DES the lineshape will oscillate along population time t_2 . **e** In SRPP, the lattice contribution is an oscillation on top of the electronic contribution. inset: Cartoon of a QD. **f** The Fourier transform of the oscillations in **e** show well-resolved Lorentzian peaks.

With NCs, one can also obtain better control of the number of excitations within some space – now defined by the particle volume. Figure 5.2b shows the lattice reorganization after photoexcitation; instead of delocalized coherent motion, there is a local overdamped reorganization around the excited carrier. This overdamped reorganization is thought to arise from acoustic modes that are overdamped at room temperature[26]. This lattice distortion stabilizes excited charges, creating a polaron. Wavepacket movement along the excited state PES is diffusive and incoherent, shown in figure 5.2c. This produces spectral diffusion in a 2DES experiment, shown in figure 5.2d. As the wavepacket diffusively explores the energy landscape the lineshape evolves from an ellipse along the diagonal to a rounded shape. In SRPP it is a highly damped signal that quickly approaches the pure electronic response, schematically shown in figure 5.2e. In an over-

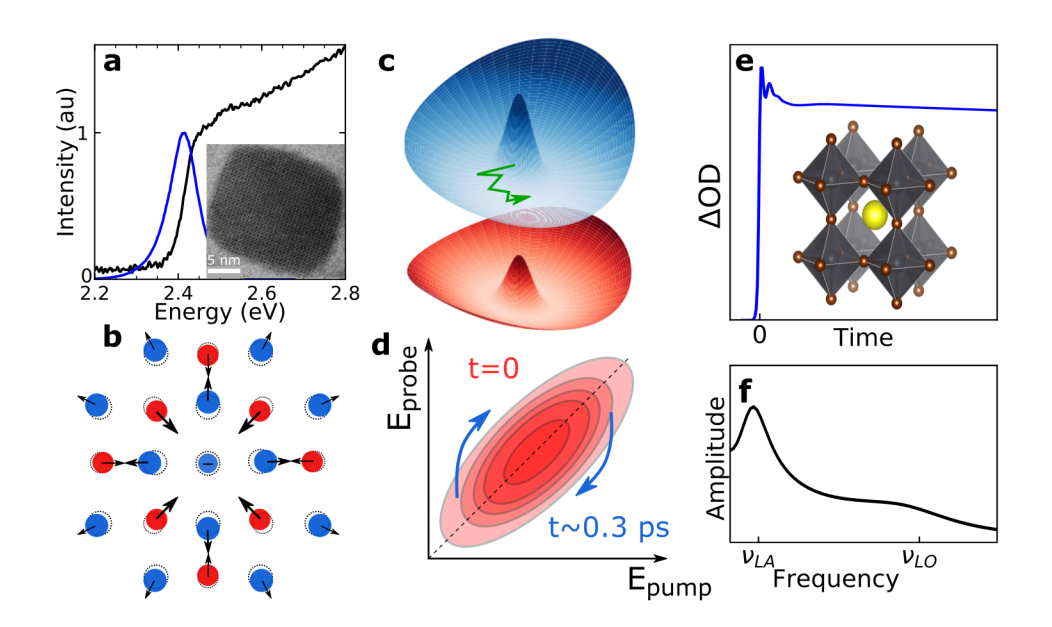


Figure 5.2: Electron-phonon coupling in ionic perovskite systems. **a** Linear absorption and PL in CsPbBr₃ NCs, with no obvious excitonic peaks. inset: TEM of a single NC. **b** Schematic showing polaron formation in an ionic crystal. **c** This is diffusive relaxation to the upper state PES minimum after photoexcitation from the ground state PES. **d** In 2DES the lineshape undergoes spectral diffusion as the wavepacket relaxes. **e** In SRPP polaron formation is an overdamped response on top of electronic dynamics. inset: CsPbBr₃ unit cell. **f** In frequency space this overdamped reponse is broad with indistinct peaks.

damped system with dynamic disorder, the local modes result in a broad spectral density as in figure 5.2f.

While some papers report coherent modulations in TA spectroscopy [36, 37, 38] these are all methyl-ammonium samples in thin films, so are not the same samples studied here. These results were also obtained with different instruments than those used here that may be better able to detect these small changes in TA signal. The results presented in figures 5.1-5.3 should be regarded as self-consistent since they were all detected in the same lab and following the same procedures. So even if coherent phonons exist in the CsPbBr₃ samples studied here, we can at least say they are significantly weaker than in CdSe quantum-dot based systems.

5.2 SRPP results

Figure 5.3 shows an overview of the SRPP data in both systems. Figure 5.3**a-d** shows the response of CsPbBr₃ NCs, while CdSe QDs are shown in figure 5.3**e-h**. Figure 5.3**a** shows the response after resonant band edge excitation for CsPbBr₃ NCs. There is a rapid shifting in the main bleach feature that is not apparent for CdSe nanocrystal QDs (fig. 5.3**e**). This rapid shift is completely hidden when pumping the sample at energies greater than the band gap, i.e 3.1 eV (fig. 5.3**b**). With a higher energy pump pulse, other signals are apparent; such as a broad, short-lived excited state absorption (ESA) to the red of the band edge, as seen figure 5.3**b**,**f**.

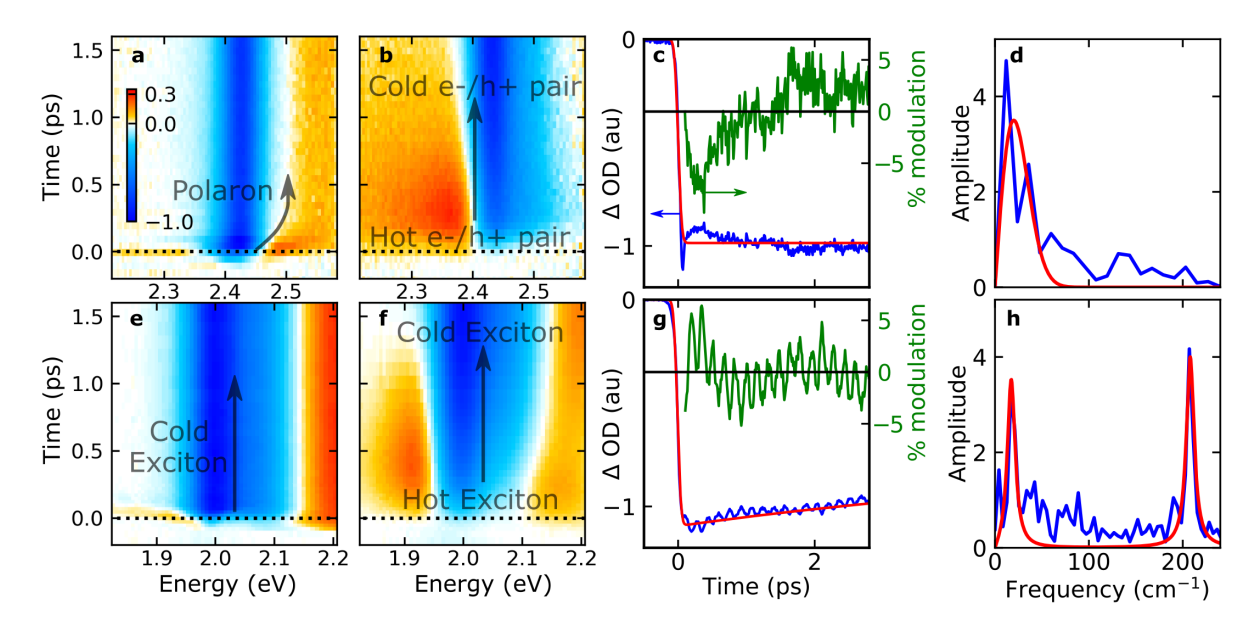


Figure 5.3: Overview of SRPP signals in **a-d** CsPbBr₃ NCs and **e-h** CdSe QDs. Time and energy resolved SRPP signals for **a,e** band edge pumping and **b,f** 3.0 eV pumping. **c,g** Band edge bleach dynamics (blue) are modelled as exponential decay (red). The residuals show motion along the upper PES (green). **d,h** Fourier transform of this motion (blue) shows the density of states in a multimode-Brownian oscillator model. (red)

By monitoring the main bleach feature through time, it is possible to detect wavepacket motion along the excited state through modulations of the pump-probe signal. These are shown in figure 5.3c and g, for CsPbBr₃ NCs and CdSe QDs respectively.

The electronic response (red line in figure 5.3c,g) is subtracted from the data (blue markers) to yield the lattice response (green line, right axis). The frequency space analog of the lattice response is shown in Figure 5.3d,f for CsPbBr₃ NCs and CdSe nanocrystal QDs, respectively. In ionic CsPbBr₃ NCs the response is incoherent and diffusive. Such a response is shown by the overdamped response in figure 5.3c and the broad low-frequency response in frequency space. This response is akin to a spectral density of local phonon modes, rather than discrete vibrations. One sees such spectral densities commonly in liquids and glasses[33, 39, 40]. For covalent CdSe, the lattice response is coherent, as shown by the clear oscillations in figure 5.3g, and well resolved Lorentzian peaks in figure 5.3h. Both systems can be modelled as a multi-mode Brownian oscillator (MBO) [40] (red lines in figure 5.3d,h). In the MBO the frequency-fluctuation correlation function (FFCF) is described as a sum of individual oscillator responses coupling to each bath mode. Due to the symmetry properties of the FFCF it is sufficient to describe the imaginary part of the complex FFCF in frequency space to fully describe the lineshape function of these transitions.

$$\tilde{C}''(\omega) = \sum_{j} \xi_{j}^{2} \tilde{C}_{j}''(\omega) \tag{5.1}$$

$$\tilde{C}_{j}^{"}(\omega) = \frac{\hbar}{2m_{j}} \frac{\omega \gamma_{j}(\omega)}{(\omega_{j}^{2} - \omega^{2})^{2} + \omega^{2} \gamma_{j}^{2}(\omega)}$$
(5.2)

(5.3)

In equations 5.1 and 5.2 the ω_j are the resonant frequencies of each individual system mode, ξ_j is a measure of ground state and excited state displacement along the j^{th} vibrational coordinate, and the $\gamma_j(\omega)$ represent oscillator damping due to system-bath

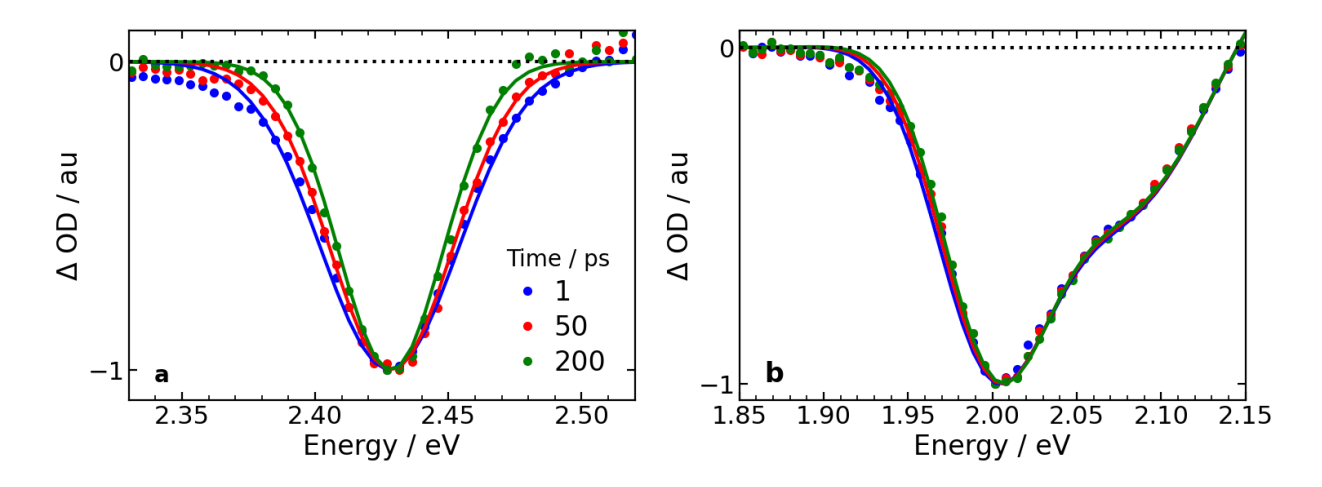


Figure 5.4: Normalised transient absorption spectra of **a** CsPbBr₃ NCs and **b** CdSe QDs. Dots represent data, and solid lines are models used to fit that data.

coupling. The damping of the j^{th} mode is a sum over the coupled bath modes ω_n .

$$\xi_j = \frac{m_j \omega_j^2}{\hbar} d_j \tag{5.4}$$

$$\gamma_j(\omega) = \pi \sum_n c_{nj}^2 2m_n \omega_n^2 \delta(\omega - \omega_n)$$
 (5.5)

Appropriate choices for ω_j and γ_j yield the red curves shown in figure 5.3**d,h**.

Looking more closely at the evolution of the pump-probe spectra under band edge pump in figure 5.3**a**,**e** it is apparent that clearly different processes are occurring in CsPbBr₃ NCs compared to CdSe QDs. To better visualise these changes, normalised spectra are plotted at 1, 50, and 200 ps for each sample in figure 5.4. Figure 5.4**a**(**b**) shows the evolution in shape of the CsPbBr₃ NC (CdSe QD) pump-probe spectrum. While the CdSe spectrum doesn't change in shape over the time range examined (300 fs - 200 ps) that of CsPbBr₃ undergoes significant change, particularly in the linewidth of the main bleach feature. To extract and quantify these lineshape changes, the Δ OD spectrum of each sample was modelled and a linewidth extracted. For CsPbBr₃ NCs that model was a single Gaussian peak centred at the band edge bleach, while the model used for CdSe is based on the literature [41] and summarised in appendix 5.A.

These lineshape dynamics for both CsPbBr₃ and CdSe are quantified in figure 5.5. Figure 5.5a shows the evolution of the 2.42 eV bleach linewidth in CsPbBr₃. Initially the linewidth is limited by the pump pulse bandwidth of 24 meV. The peak subsequently broadens in the first picosecond, then continuously narrows over the next 200 ps. Figure 5.5b shows the relative movement of the bleach in CsPbBr₃. The peak rapidly blueshifts in the first picosecond, redshifts very slightly over the next 20 ps, then remains static. In CdSe QDs, the linewidth of the main bleach feature at 2.0 eV undergoes a very slight narrowing of \sim 1.5 meV over 200 ps (Figure 5.5c) while the position of the bleach feature (Figure 5.5d, inset) blueshifts by \sim 2 meV over 200 ps. Both the line-narrowing and blueshifting in CdSe can be attributed to the recombination of biexcitons[42]. For CsPbBr₃, the fast process in both the line broadening and blue shifting can be assigned to polaron formation[18, 22]. The slow process of line narrowing in CsPbBr₃ NCs is a new observation, that can not be assigned to hot carriers because of the pump energy. We assign the observed line narrowing process in CsPbBr₃ to thermalization within an exciton fine structure. This invocation of fine structure is supported by single crystal PL measurements in similar systems [43, 44, 45].

5.3 Relaxation and recombination

Figure 5.6a,b shows the relaxation of excited charge carriers. To observe relaxation of single carriers, the evolution of the pump-probe signal is monitored for both 2.4 eV and 3.1 eV pump energies simultaneously. A state-resolved approach controls for relaxed state dynamics by subtracting the pump-probe signal with resonant band edge excitation from the pump-probe signal from a more energetic pump[46]. This yields a $\Delta\Delta$ OD trace that directly tracks the difference between highly excited carriers and band edge carriers.

The pump-probe spectral signatures depend on the state of the exciton. It has been previously shown in II-VI NCs that the band edge bleach reflects electron population[47].

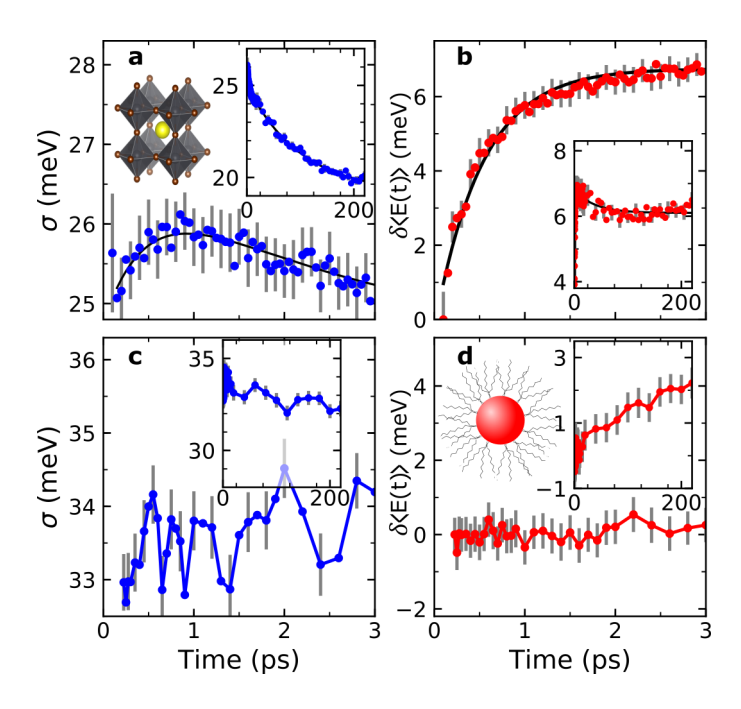


Figure 5.5: Lineshape dynamics in **a,b** ionic CsPbBr₃ perovskite and **c,d** covalent CdSe. a Linewidth and b blueshift of the band edge bleach in CsPbBr₃. c Linewidth and d blueshift of the the X_1 excitonic peak in CdSe. Insets in **a-d** show same data over a different scale.

The sub band edge ESA is due to absorption from a ground state exciton to a biexciton. Thus dynamics in the ESA reflect exciton dynamics[48, 49]. These spectral signatures allow for the disentangling of relaxation channels. Here, the bleach at 2.44 eV is used to follow electron relaxation (fig. 5.6a). With a 3.10 eV pump energy electrons are pumped relatively high in the conduction band, and relax through a complicated pathway described by quantum kinetics. A simple model is proposed here, where the electrons initially relax rapidly through a dense manifold of states. Immediately after photoinjection, this rate decreases linearly to a steady state, late time relaxation rate. This model is described below:

$$\frac{dn_e}{dt} = -k(t)n_e \tag{5.6}$$

$$\frac{dn_e}{dt} = -k(t)n_e$$

$$\Rightarrow n_e(t) = n_{e0} \exp\left(-\int_0^t k(t')dt'\right)$$
(5.6)

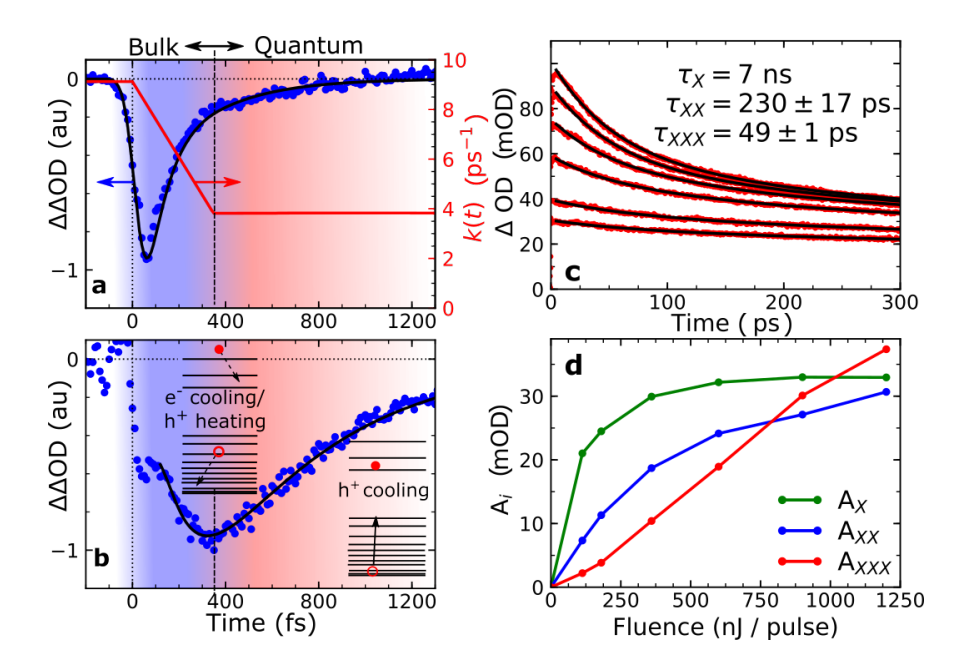


Figure 5.6: Carrier cooling and multiexciton recombination in bulk-regime CsPbBr₃ NCs. **a**,**b** $\Delta\Delta$ OD measures control for dynamics of the ground state, showing **a** non-exponential electron cooling and **b** electron to hole energy transfer. **c** Auger recombination rates measured through band edge bleach dynamics under increasing pump fluence. **d** Amplitude of exponential decay components as a function of pump fluence.

Where we have chosen k(t) to take the following form:

$$k(t) = \begin{cases} k_{start} & t \le 0 \\ k_{stop} & t \ge t_{stop} \\ \frac{k_{start} - k_{stop}}{t_{stop}} & 0 < t < t_{stop} \end{cases}$$

$$(5.8)$$

While other models can be found in the literature [50, 51] the simplest non-continuous model was chosen here to observe the effect. As the electrons approach the band edge, the density of accessible states decreases, causing relaxation to slow down.

The fit returns the expected result, an initially fast rate of \sim 9 ps⁻¹ slows down over 300 fs to a final rate of \sim 4 ps⁻¹. This non-exponential relaxation is a sign of bulk-like

decay becoming quantum confined, as the polaronic confinement dynamically creates sparse energy levels.

The dynamics of the sub-band gap ESA reveal new observations on excitons in these perovskites. Figure 5.6b shows the $\Delta\Delta$ OD signal at 2.36 eV. Here both a growth and a decay are apparent. In analogy to previous work in CdSe QDs, the growth is a sign of electron to hole energy transfer through two-particle intra-band Auger relaxation[46]. A growth in this signal is not possible without energy transfer from hot electrons to holes. The growth is well resolved; as can be seen in Figure 5.6b, the fit is performed only after 100 fs. The fast rise is followed by a slower decay through phonon coupling, as is observed in physically confined II-VI nanocrystal QDs[52].

Multiexciton recombination kinetics can further reveal the presence of quantum Confinement effects[47, 53, 54]. Figure 5.6**c**,**d** shows the presence of MXs through the decay of the bleach at 2.42 eV after resonant band edge pumping. Figure 5.6**c** shows the bleach signal under increasing pump fluence. At low fluence the Δ OD signal is mostly due to single excitons (X). As fluence increases biexcitons and triexcitons become sequentially more populated and contribute to the signal.

The overall signal decay is modelled as a triexponential decay, with each component corresponding to recombination of multiexcitons, biexcitons, and single excitons.

$$\Delta OD(t) = A_X e^{-t/\tau_X} + A_{XX} e^{-t/\tau_{XX}} + A_{MX} e^{-t/\tau_{MX}}$$
(5.9)

In fitting the Auger recombination curves in figure 5.6c the entire dataset was fit to the model presented in equation 5.9 with common time constants for each fluence probed and individual amplitudes allowed to float. The total decay lifetime of single excitons was fixed at 7 ns, corresponding to results from TCSPC measurements. Figure 5.6d shows the amplitudes of each component as a function of fluence. There is a clear

saturation behaviour for both excitons and biexcitons, direct evidence of the existence of confined excitons.

It is also interesting to look at another model for Auger recombination; that of a bulk semiconductor. Here, Auger rates will exist on a continuum dependent only on the concentration of carriers. Since it is free carriers interacting in a three-particle process we have

$$\frac{dn}{dt} = -C_A n^3 \tag{5.10}$$

With C_A a coefficient with units cm^6s^{-1} and n is the density of electrons or holes, assumed equal here. Equation 5.10 is often re-framed in the form of an instantaneous Auger rate[55].

$$\frac{1}{\tau_A} = C_A n^2 \tag{5.11}$$

Here $1/\tau_A$ scales as n^2 , so the rate should continue to increase, or the lifetime decrease, with increasing fluence. This power dependent model, where the recombination rates are allowed to float with excitation fluence, is shown in figure 5.7. By examining the SRPP data under 3.1 eV excitation, there is no state-filling limit to the number of excitons that can be created, as would exist with a band edge pump. This is shown in figure 5.7a. By examining the trend of Auger lifetime with fluence, as in figure 5.7b,c, no trend is observed. If anything lifetimes get longer with fluence, at least in the low fluence regime. This is the opposite of what would be expected.

Given that the physical size of these NCs is \sim 20 nm, and the exciton Bohr diameter is \sim 7 nm, the question naturally arises as to the origin of the observed confinement effects. In short, the polaronic potential causes confinement. Basic polaron properties can be derived from the static and optical dielectric constants, phonon energies, and effective mass of the bare carriers[56]. The electron-phonon coupling constant, α , describes how

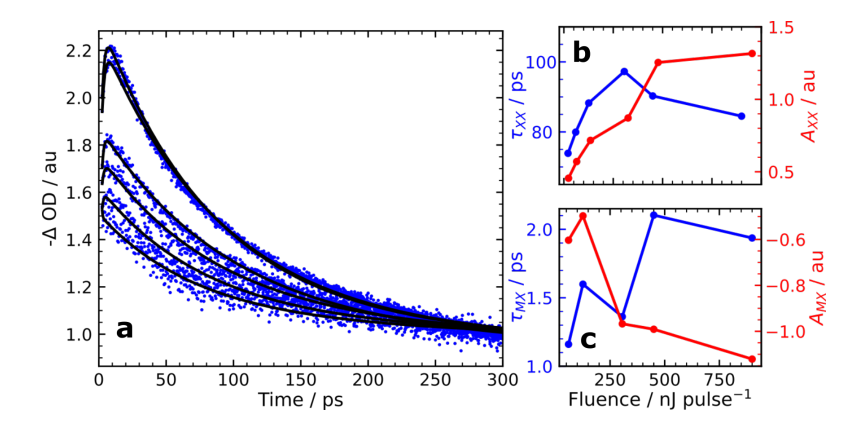


Figure 5.7: Auger recombination in a bulk-like model for CsPbBr₃ NCs. **a** tail-normalized Δ OD data after 3.1 eV excitation with fits to biexponetnial decay. **b,c** Pump pulse fluence dependence of the **b** slow and **c** fast components of the fit results.

well a charge is screened by the lattice. This is given by equation 1.23, and again below:

$$\alpha = \frac{e^2}{\hbar 4\pi\epsilon_0} \left(\frac{1}{\epsilon_\infty} - \frac{1}{\epsilon_0} \right) \sqrt{\frac{m^*}{2\hbar\omega_{LO}}}$$
 (5.12)

By examining the energy and radius of the formed polarons, using equations 1.25 and 1.26, we find that polarons in this material should have a binding energy of \sim 47 meV[15] and diameter of approximately 5 nm[16], yielding weak confinement for carriers. These values are in line with experimental [22, 25] and computational work[57].

Another question that naturally arises is that of spatial extent; how can a cube of 20 nm edge length support three or more exciton-polarons of 5-7 nm in diameter? There are two parts to the solution, one is realizing that multi-excitons are bound relative to single excitons, so a biexciton will have diameter less than $2a_0$. The second part of the solution comes from looking at conventional II-VI QDs, such as CdSe. These systems are often only 2 or 3 nm in radius, yet support biexcitons and even tri-excitons. This is despite their excitonic Bohr radius of 5.4 nm[58].

The carrier-lattice coupling in covalent and ionic semiconductor materials has been compared and contrasted. In agreement with previous work, polaron formation is found in ionic CsPbBr₃ NCs and coherent phonons are found in CdSe QDs. If polarons do indeed improve device performance; these results could point the way to new ionic semiconductors for opto-electronic applications. There is also the observation of confinement effects in the Auger recombination of multi-excitons in CsPbBr₃ NCs. This is an important result that could have implications in bulk systems, since the nanocrystals used here show no quantum confinement effects in linear spectroscopy.

Bibliography

- [1] Sutherland, B. R.; Sargent, E. H. Nature Photonics 2016, 10, 295–302.
- [2] Stranks, S. D.; Snaith, H. J. *Nature Nanotechnology* **2015**, 10, 391–402.
- [3] Kovalenko, M. V.; Protesescu, L.; Bodnarchuk, M. I. Science 2017, 358, 745–750.
- [4] Akkerman, Q. A.; Rainò, G.; Kovalenko, M. V.; Manna, L. *Nature Materials* **2018**, 17, 394–405.
- [5] Ren, H.; et al. Nature Photonics 2020, 14, 154–163.
- [6] Li, J.; Xu, L.; Wang, T.; Song, J.; Chen, J.; Xue, J.; Dong, Y.; Cai, B.; Shan, Q.; Han, B.; Zeng, H. Advanced Materials 2017, 29, 1603885.
- [7] Liao, Q.; Hu, K.; Zhang, H.; Wang, X.; Yao, J.; Fu, H. Advanced Materials 2015, 27, 3405–3410.
- [8] Zhu, H.; Miyata, K.; Fu, Y.; Wang, J.; Joshi, P. P.; Niesner, D.; Williams, K. W.; Jin, S.; Zhu, X. Y. Science 2016, 353, 1409–1413.
- [9] Thouin, F.; Srimath Kandada, A. R.; Valverde-Chávez, D. A.; Cortecchia, D.; Bargigia, I.; Petrozza, A.; Yang, X.; Bittner, E. R.; Silva, C. Chemistry of Materials 2019, 31, 7085–7091.
- [10] Lan, Y.; Dringoli, B. J.; Valverde-Chávez, D. A.; Ponseca, C. S.; Sutton, M.; He, Y.; Kanatzidis, M. G.; Cooke, D. G. *Science Advances* **2019**, 5.

- [11] Munson, K. T.; Kennehan, E. R.; Doucette, G. S.; Asbury, J. B. Chem 2018, 4, 2826–2843.
- [12] Zhu, X. Y.; Podzorov, V. Journal of Physical Chemistry Letters 2015, 6, 4758–4761.
- [13] Kang, J.; Wang, L. W. Journal of Physical Chemistry Letters 2017, 8, 489–493.
- [14] Brandt, R. E.; Stevanović, V.; Ginley, D. S.; Buonassisi, T. MRS Communications 2015, 5, 265–275.
- [15] Miyata, K.; Atallah, T. L.; Zhu, X. Y.; Lead halide perovskites: Crystal-liquid duality, phonon glass electron crystals, and large polaron formation; 2017. http://advances.sciencemag.org/lookup/doi/10.1126/sciadv.1701469.
- [16] Miyata, K.; Meggiolaro, D.; Tuan Trinh, M.; Joshi, P. P.; Mosconi, E.; Jones, S. C.; De Angelis, F.; Zhu, X. Y. *Science Advances* **2017**, *3*.
- [17] Wu, K.; Park, Y.-S.; Lim, J.; Klimov, V. I. Nature Nanotechnology 2017, 12, 1140–1147.
- [18] Bretschneider, S. A.; Ivanov, I.; Wang, H. I.; Miyata, K.; Zhu, X.; Bonn, M. *Advanced Materials* **2018**, *30*, 1707312.
- [19] Park, M.; Neukirch, A. J.; Reyes-Lillo, S. E.; Lai, M.; Ellis, S. R.; Dietze, D.; Neaton, J. B.; Yang, P.; Tretiak, S.; Mathies, R. A. *Nature Communications* **2018**, *9*, 1–9.
- [20] Neukirch, A. J.; Abate, I. I.; Zhou, L.; Nie, W.; Tsai, H.; Pedesseau, L.; Even, J.; Crochet, J. J.; Mohite, A. D.; Katan, C.; Tretiak, S. *Journal of Physical Chemistry Letters* **2018**, 9,7130–7136.
- [21] Forde, A.; Inerbaev, T.; Kilin, D. Journal of Physical Chemistry C 2020.
- [22] Seiler, H.; Palato, S.; Sonnichsen, C.; Baker, H.; Socie, E.; Strandell, D. P.; Kambhampati, P. *Nature Communications* **2019**, *10*, 1–8.
- [23] Yi, H. T.; Wu, X.; Zhu, X.; Podzorov, V. Advanced Materials 2016, 28, 6509-6514.

- [24] Guzelturk, B.; et al. Nature Materials 2021.
- [25] Puppin, M.; et al. Physical Review Letters 2020, 124, 206402.
- [26] Yaffe, O.; Guo, Y.; Tan, L. Z.; Egger, D. A.; Hull, T.; Stoumpos, C. C.; Zheng, F.; Heinz, T. F.; Kronik, L.; Kanatzidis, M. G.; Owen, J. S.; Rappe, A. M.; Pimenta, M. A.; Brus, L. E. *Physical Review Letters* 2017, 118, 1–6.
- [27] Schilcher, M. J.; Robinson, P. J.; Abramovitch, D. J.; Tan, L. Z.; Rappe, A. M.; Reichman, D. R.; Egger, D. A. ACS Energy Letters 2021, 2162–2173.
- [28] Bragas, A. V.; Aku-Leh, C.; Costantino, S.; Ingale, A.; Zhao, J.; Merlin, R. *Physical Review B Condensed Matter and Materials Physics* **2004**, *69*, 1–11.
- [29] Walsh, B. R.; Sonnichsen, C.; MacK, T. G.; Saari, J. I.; Krause, M. M.; Nick, R.; Coe-Sullivan, S.; Kambhampati, P. *Journal of Physical Chemistry C* **2019**, 123, 3868–3875.
- [30] Tyagi, P.; Cooney, R. R.; Sewall, S. L.; Sagar, D. M.; Saari, J. I.; Kambhampati, P. *Nano Letters* **2010**, *10*, 3062–3067.
- [31] Caram, J. R.; Zheng, H.; Dahlberg, P. D.; Rolczynski, B. S.; Griffin, G. B.; Dolzhnikov, D. S.; Talapin, D. V.; Engel, G. S. *Journal of Chemical Physics* **2014**, *140*.
- [32] Peng, Z. A.; Peng, X. Journal of the American Chemical Society 2001, 123, 183–184.
- [33] Myers, A. B. Annual Review of Physical Chemistry **1998**, 49, 267–295.
- [34] Jimenez, R.; Fleming, G. R.; Kumar, P. V.; Maroncelli, M. Nature 1994, 369, 471–3.
- [35] Protesescu, L.; Yakunin, S.; Bodnarchuk, M. I.; Krieg, F.; Caputo, R.; Hendon, C. H.; Yang, R. X.; Walsh, A.; Kovalenko, M. V. *Nano Letters* **2015**, *15*, 3692–3696.
- [36] Batignani, G.; Fumero, G.; Srimath Kandada, A. R.; Cerullo, G.; Gandini, M.; Ferrante, C.; Petrozza, A.; Scopigno, T. *Nature Communications* **2018**, *9*, 1–5.

- [37] Ghosh, T.; Aharon, S.; Etgar, L.; Ruhman, S. *Journal of the American Chemical Society* **2017**, 139, 18262–18270.
- [38] Wang, H.; Valkunas, L.; Cao, T.; Whittaker-Brooks, L.; Fleming, G. R. *Journal of Physical Chemistry Letters* **2016**, 7.
- [39] Cho, M.; Fleming, G. R.; Saito, S.; Ohmine, I.; Stratt, R. M. *The Journal of Chemical Physics* **1994**, *100*, 6672–6683.
- [40] Mukamel, S. *Principles of Nonlinear Optical Spectroscopy*; Oxford University Press, 1995.
- [41] Zhang, C.; Do, T. N.; Ong, X.; Chan, Y.; Tan, H. S. Chemical Physics 2016, 481, 157–164.
- [42] Palato, S.; Seiler, H.; Baker, H.; Sonnichsen, C.; Brosseau, P.; Kambhampati, P. *Journal of Chemical Physics* **2020**, 152.
- [43] Becker, M. A.; et al. *Nature* **2018**, *553*, 189–193.
- [44] Yin, C.; Chen, L.; Song, N.; Lv, Y.; Hu, F.; Sun, C.; Yu, W. W.; Zhang, C.; Wang, X.; Zhang, Y.; Xiao, M. *Physical Review Letters* **2017**, *119*, 026401.
- [45] Tamarat, P.; Bodnarchuk, M. I.; Trebbia, J.-B.; Erni, R.; Kovalenko, M. V.; Even, J.; Lounis, B. *Nature Materials* **2019**.
- [46] Cooney, R. R.; Sewall, S. L.; Anderson, K. E. H.; Dias, E. A.; Kambhampati, P. *Physical Review Letters* **2007**, *98*, 1–4.
- [47] Klimov, V. I. The Journal of Physical Chemistry B 2000, 104, 6112–6123.
- [48] Kambhampati, P. J. Phys. Chem. C 2011, 115, 22089–22109.
- [49] Kambhampati, P. Accounts of Chemical Research 2011, 44, 1–13.

- [50] Boehme, S. C.; Brinck, S. t.; Maes, J.; Yazdani, N.; Zapata, F.; Chen, K.; Wood, V.; Hodgkiss, J. M.; Hens, Z.; Geiregat, P.; Infante, I. *Nano Letters* **2020**, acs.nanolett.9b05051.
- [51] Forde, A.; Inerbaev, T.; Hobbie, E. K.; Kilin, D. S. Journal of the American Chemical Society 2019, 141, 4388–4397.
- [52] Cooney, R. R.; Sewall, S. L.; Dias, E. A.; Sagar, D. M.; Anderson, K. E.; Kambhampati, P. *Physical Review B Condensed Matter and Materials Physics* **2007**, *75*, 1–14.
- [53] Klimov, V. I. Annual Review of Physical Chemistry 2007, 58, 635–673.
- [54] Tyagi, P.; Kambhampati, P. Journal of Chemical Physics 2011, 134.
- [55] Melnychuk, C.; Guyot-Sionnest, P. Chemical Reviews 2021.
- [56] Frost, J. M. Physical Review B **2017**, 96, 1–10.
- [57] Bokdam, M.; Sander, T.; Stroppa, A.; Picozzi, S.; Sarma, D. D.; Franchini, C.; Kresse, G. *Scientific Reports* **2016**, *6*, 1–8.
- [58] Fisher, B.; Caruge, J. M.; Zehnder, D.; Bawendi, M. *Physical Review Letters* **2005**, 94, 1–4.

5.A Modelling the TA spectrum of CdSe quantum dots

Using the contributions to the TA signal discussed in section 2.2.2, the TA spectrum for a fully relaxed single exciton can be modelled with a high degree of accuracy to extract a biexciton spectrum [41] or to observe changes in linewidth or transition energy, as is done in chapter 5. The first step is to extract exciton energies and linewidths from the linear absorption spectrum. To do this, a good model is a sum of Gaussian peaks for each excitonic transition with a polynomial background to account for scattering and free-carrier absorption.

$$OD(\omega) = \sum_{i=1}^{3} A_1 \exp\left(\frac{-(\omega - \omega_i)^2}{2\sigma_i^2}\right) + a\omega^2 + b\omega + c$$
 (5.13)

The results of this fit for the CdSe samples used in chapter 5 are shown in figure 5.8. Figure 5.8a shows the raw data and the model result. Figure 5.8b shows the model residuals. Residuals are relatively small across the absorption spectrum. Table 5.1 shows the fitting parameters retrieved from this analysis.

X1	A_{X1}	σ_{X1} / meV	ω_{X1} / eV
value	0.68 ± 0.02	34.2 ± 0.3	$1.993 \pm 3e-4$
X2	A_{X2}	σ_{X2} / meV	ω_{X2} / eV
value	0.47 ± 0.01	53.3 ± 1.2	$2.066 \pm 2e-3$
X3	A_{X3}	σ_{X3} / meV	ω_{X3} / eV
value	0.82 ± 0.07	104 ± 4	$2.327 \pm 4e-3$
Background	a / eV^{-2}	b / eV ⁻¹	c
Value	2.5 ± 0.3	-8.9 ± 1.1	8.0 ± 1.0

Table 5.1: Fit parameters for the linear absorption model of CdSe in equation 5.13 and shown in figure 5.8

With the values obtained through fitting the linear spectrum for the excitonic peaks, it is now possible to accurately describe the Δ OD spectrum of a single fully relaxed

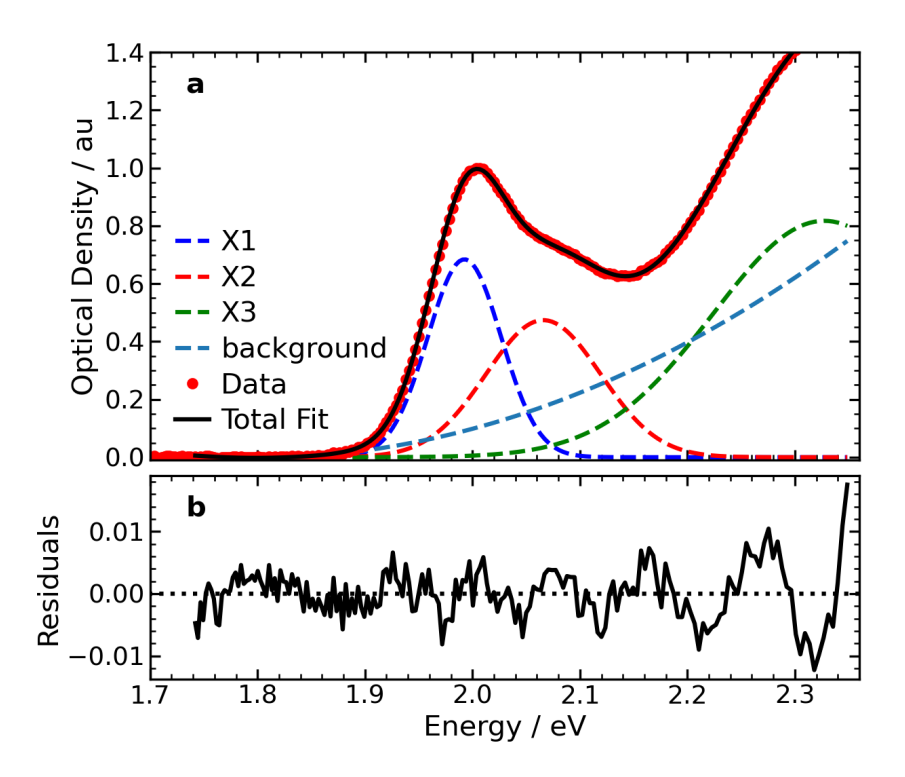


Figure 5.8: Result of fitting CdSe QD linear absorption data to equation 5.13 **a** Raw data and excitonic contributions to overall absorption. **b** Fit residuals.

exciton. This is given by the following set of equations:

$$GSB(\omega) = \sum_{i=1}^{3} A_i \exp\left(\frac{-(\omega - omega_i)^2}{2\sigma_i^2}\right)$$
 (5.14)

$$ESA(\omega) = \sum_{i=1}^{3} A_i \alpha_i \exp\left(\frac{-(\omega - (omega_i - \Delta_i))^2}{2\sigma_i^2}\right)$$
 (5.15)

$$SE(\omega) = A_1 \exp\left(\frac{-(\omega - \omega_1)^2}{2\sigma_1^2}\right)$$
 (5.16)

$$\Delta OD(\omega) = -GSB(\omega) - SE(\omega) + ESA(\omega)$$
 (5.17)

Here we have introduced two new sets of parameters for each excited state transition; α_i and Δ_i . The α_i describe the change in oscillator strength for the $X_1 \to X_1 X_i$ transition compared to the $0 \to X_i$ transition. The Δ_i are the binding energies of the biexciton state $X_1 X_i$. Using this model a fit result similar to that presented in figure 5.9 and

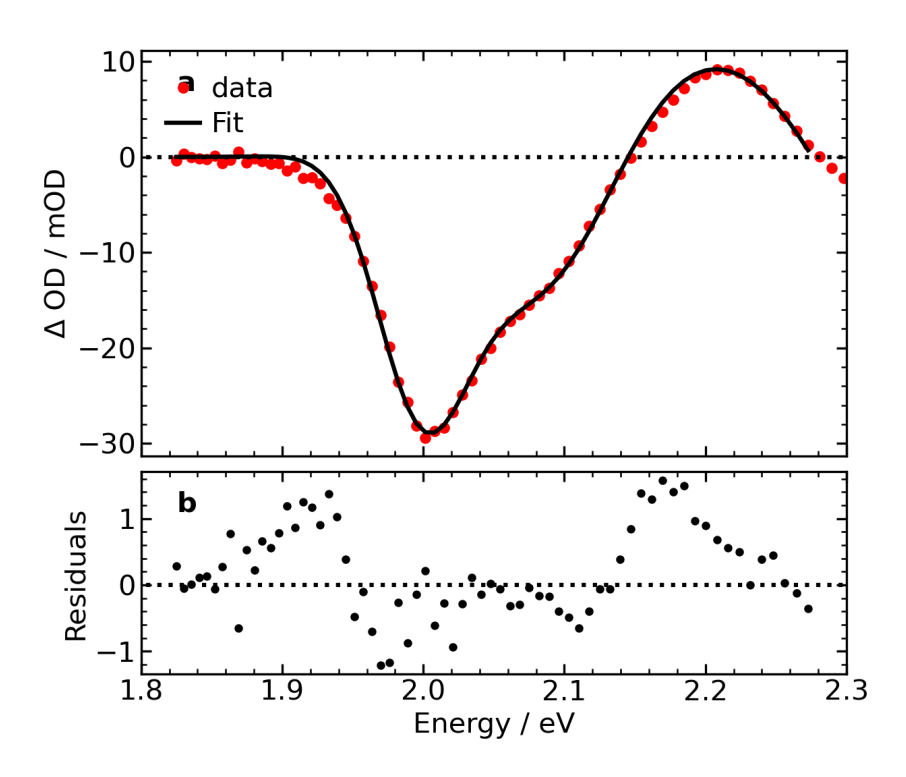


Figure 5.9: Result of fitting equations 5.14-5.17 to the transient absorption spectrum of CdSe QDs. **a** Raw data and fit result. **b** Fit residuals.

table 5.2 can be readily obtained.

Parameter	α_1	Δ_1 / meV	α_2	Δ_2 / meV	α_3	Δ_3 /meV
Value	0.69 ± 0.02	3.2 ± 0.5	0.732 ± 0.015	7.7 ± 1.9	0.94 ± 0.08	18 ± 4

Table 5.2: Fit results for the transient absorption model presented in equation 5.14-5.17 and figure 5.9.

These results are used in chapter 5 to create figure 5.5. The center energy and linewidth of X1 are allowed to vary in equation 5.17 and the fit is performed for each time. This yields the results presented in figure 5.5c and d.

Chapter 6

An OPA-driven hollow core fibre as a tunable source for 2DES

Despite the impressive abilities of two-dimensional electronic spectroscopy (2DES), its implementation is limited due to the complexity of continuum generation and phase stability between the pump pulse pair. In light of this, we have implemented a system producing sub-10 fs pulses with central wavelength tunable across the visible spectrum. Using a commercial OPA to drive a hollow-core fiber, the system is extremely simple. Output pulse energies lie in the 40-80 μ J range, more than sufficient for transmission through the pulse shaping optics and beam splitters necessary for multi-dimensional spectroscopy. Power fluctuations are minimal, mode quality is excellent, and spectral phase is well behaved at the output. To demonstrate the strength of this source, we measure the two-dimensional spectrum of CdSe quantum dots over a range of population times, and find clean signals and clear phonon vibrations. The combination of OPA and hollow-core fibre provides a substantial extension to the capabilities of 2DES.

6.1 Introduction

2DES is a powerful tool for probing the fastest dynamics in materials science. 2DES has already clarified fundamental questions about electron-phonon coupling in covalent II-VI semiconducting nanocrystals [1, 2, 3, 4] and ionic perovskite nanostructures [5, 6]. Other notable measures are the excited structure through double quantum spectroscopy [7, 8, 9], and electronic coherences between excitonic states [10] or individual quantum dot systems [9].

A common approach for broadband pulses in 2DES is to use a non-collinear optical parametric amplifier (NOPA) [11, 12, 13, 14]. These devices are large and involve several frequency conversions and mixing. Their proper alignment for maximum bandwidth, low noise, high power operation can be complicated. To switch a NOPA from visible to IR operation requires different crystal cuts and re-optimization of crossing angles, or construction of a completely separate NOPA.

Hollow-core fibres (HCFs) for continuum generation are a general approach for pulse broadening, and have been used to generate multiple-octave spanning spectra [15, 16]. These approaches use very high peak field strengths and high pressures to generate the super-broad spectra, and are often highly unstable, due to the several orders of nonlinearity in pulse propagation. In regards to precision spectroscopy, stability in phase, spectrum and power are all very important and these characteristics are prioritized over octave spanning pulses. For this unstructured fibres driven by weaker pulses have been used [17, 18, 19]. One issue with this approach is the inability to tailor the central wavelength of the laser spectrum to a particular sample, the experimenter is limited to samples whose transitions of interest lie in the fixed spectrum provided by the light source. In response to the problems presented by NOPAs and HCFs driven by the fundamental laser wavelength, we present an OPA-driven HCF as a tunable, broadband low noise source for 2DES.

The block diagram of the tunable continuum source is shown in figure 6.1a. A Ti:Sapphire based CPA system producing 2 mJ, 100 fs pulses (Coherent Legend Elite Duo) is used to drive a commercial OPA (TOPAS). The output of the OPA is used to drive a 2.57 m long, hollow-core fibre filled with Argon [18, 20]. The OPA pulses are typically somewhat shorter than the 800nm driving pulses (ca. 90 fs vs. 100 fs), and have central wavelength spanning 300-3000 nm and energies from 20-200 μ J. For our interest we used the OPA in the range 700-500 nm, as this is roughly the bandwidth of the DAZZLER acousite pulse shapers and GRISMs used in our 2DES experiment. Using the direct signal and idler beams, from 1200-2600nm, should produce more energetic pulses and provide broader spectra than seen here. To characterize the white light generation process, transient grating FROGs (TG-FROGs) were measured at 3 locations: Before the entrance window to the fiber, after the exit window of the fiber, and after pulse compression, as shown in figure 6.1b-d. The white light generation process was found to work across the visible spectrum; the results of driving the fiber with central wavelengths spanning 750 -500 nm is shown in figure 6.1e. Approximately 200 meV of bandwidth is generated over this entire range. The inset of figure 6.1e shows an image of the collimated beam after transmission through the fiber. The spatial structure is excellent and Gaussian along both axes.

An important metric for 2DES is the stability of the source in terms of spectrum, phase, and power. As almost all 2DES experiments rely on the subtraction of subsequent shots, any shot to shot variation in the spectral width of the driving fields will appear as signal. By driving the fiber with much less energetic pulses, plasma generation is avoided and stability is improved when compared to using the 800 nm fundamental for white light generation. The excellent stability of the source is shown in figure 6.2. Here, the DAZZLER pulse shapers are used to diffract two pulses with a delay 100 fs. Over the course of ~6 hours, there is no drift in interpulse phase or delay. Furthermore spectral bandwidth and power are stable over a similar time period, as shown in figure 6.2a. Figure 6.2 b shows the width of the diffracted spectrum over time, defined as the square root

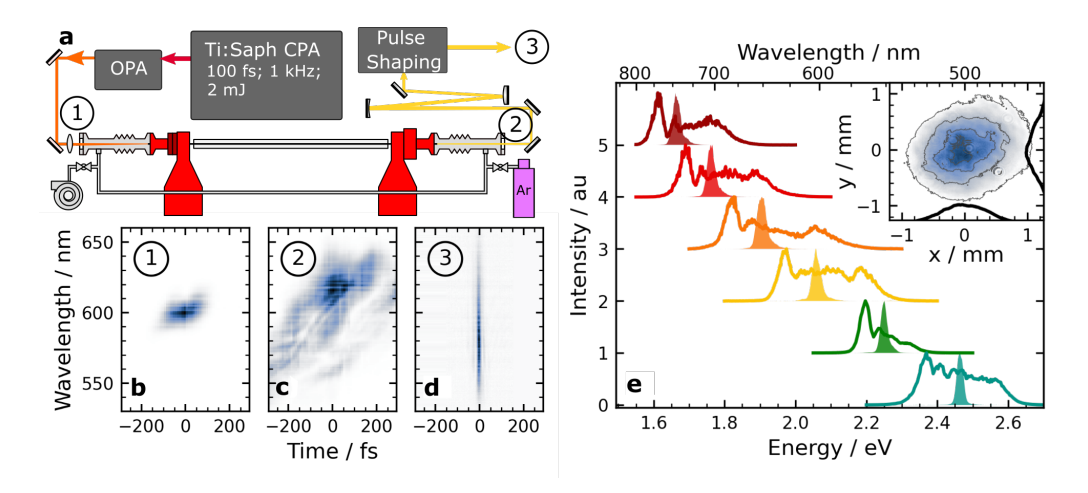


Figure 6.1: An HCF driven by an OPA for visible 2DES. **a** Optical layout of the setup. **b-d** TG-FROG traces of the pulse at the **b** fiber entrance, **c** fiber exit, and **d** after compression. The pulse in **d** has a time marginal FWHM of \sim 9.5 fs. **e** Output spectra as a function of input central wavelength. inset: Image of collimated beam profile, with sums along respective axes in white.

of the second central moment of the intensity spectrum. The overall standard error in the bandwidth is \sim 2.8%. To show the precision of delay and phase control, a TG-FROG trace of the pulse pair is measured, as shown in figure 6.2 **c**. Here the pulse copies are evident at \pm 100 fs, as is the spectral interference pattern at t=0. By changing the phase between the two pulses, the phase of this interference is shifted. In figure 6.2**d** the interference patterns for $\Delta\phi_{12}=[0,\pi]$ are shown. As these TG-FROG patterns are recorded over 1000s of laser shots, the interference patterns would not appear if there were drifts in either delay or interpulse-phase.

6.2 Modelling

The spectral broadening and phase evolution is in large part the balance of two processes: Self-phase modulation (SPM) and dispersion. SPM will create new frequencies while leaving the temporal pulse envelope unchanged. Dispersion serves to add chirp and

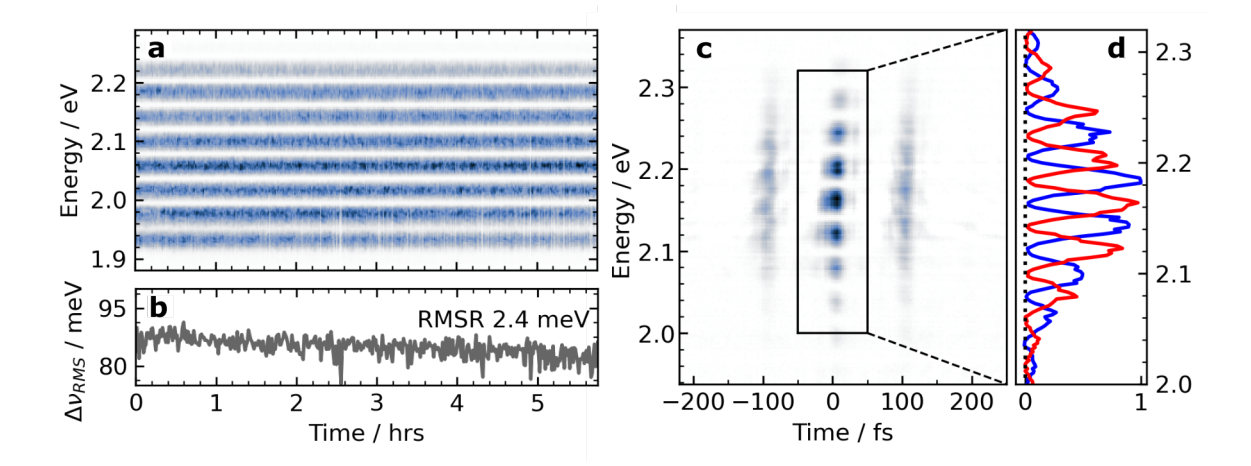


Figure 6.2: An overview of fiber stability. **a** Stable spectral interferograms show stability of phase, delay, and spectrum over the course of \sim 6 hours. **b** Spectral width over time. **c** TG-FROG trace of two pulses delayed by 100 fs. **d** time-integrated trace of the white-boxed area in **c** showing spectral interferograms for $\Delta \phi_{12} = 0$ (red) and π (blue)

lengthen the pulse, decreasing peak intensities and SPM. At high peak powers, close to resonance, or at high pressures, plasma generation becomes an issue as well[20]. Using a split-step Fourier method [21, 18] and taking into account Kerr coefficients up to 11th order, the performance of this system has been modelled by solving the nonlinear optical Schrödinger's equation.

$$\frac{\partial \tilde{\varepsilon}}{\partial z} = \tilde{D}\tilde{\varepsilon} + ik_o T \tilde{\Delta n}\varepsilon - \frac{\tilde{\alpha}}{2}\tilde{\varepsilon}$$
(6.1)

Here $\tilde{\varepsilon}$ is the Fourier transform of the slowly varying time-domain electric field envelope $\varepsilon(r,t,z)$. The right hand side of equation 6.1 describes dispersion;

$$\tilde{D}(\omega) = k(\omega) - k_0 - k_1(\omega - \omega_0) \tag{6.2}$$

self-steepening;

$$T = 1 + i\tau_{sh} \frac{\partial}{\partial t} \tag{6.3}$$

$$\tau_{sh} \approx 1/\omega_0 \tag{6.4}$$

instantaneous Kerr effects;

$$\Delta \tilde{n} = \sum_{m} n_{2m} |\varepsilon|^{2m} \tag{6.5}$$

and optical losses $\tilde{\alpha}$. The code used to perform these simulations uses a split-step Fourier method, is freely available [22], and can easily be applied to any hollow-core fibre system. Simulation results are summarised in figure 6.3. The simulated output spectra for the input pulses and fiber conditions used in figure 6.1e are shown in figure 6.3a.

The numerical simulations match experimental results very well in terms of pressure dependence, performance across the visible spectrum, and spectral structure. Increased broadening is predicted at shorter wavelengths, however this was not observed, possibly due to the anti-reflection windows at the fiber exit, which are coated for a center wavelength of 800 nm. Fiber pressure is another important consideration for fiber operation; Here numerical and experimental results are in excellent agreement, as shown in figure 6.3b. Here black is an experimental output spectrum, red is simulated, and grey is the common input spectrum. Spectral width increases almost linearly with pressure in the range explored, as in figure 6.3c. To improve performance of our HCF, increasing pressure is a good avenue to explore. Due to the absence of plasma generation in our OPA-driven HCF, greater fibre pressures compared to 800 nm driving fields is possible. Figure 6.3d shows the simulated evolution of the spectral pulse envelope as it propagates down the length of the fiber. The appearance and disappearance of spectral fringes as the pulse propagates are classic signs of SPM.

6.3 Results

To demonstrate the quality of experiment enabled by this light source, a 2DES dataset was acquired on CdSe quantum dots purchased from NNLabs. These results are shown in figure 6.4. Figure 6.4a shows the sample linear absorption in black and the laser spec-

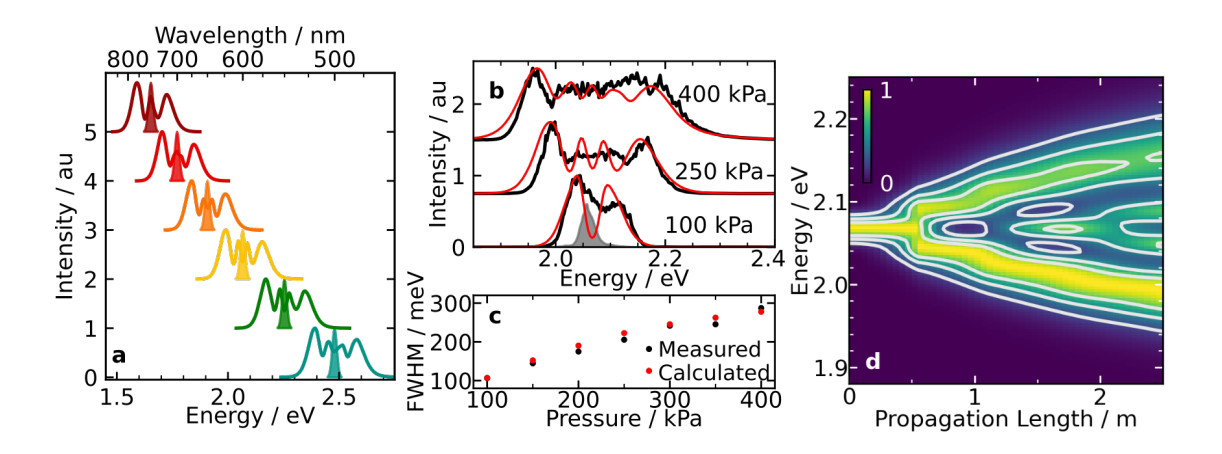


Figure 6.3: Simulated fiber performance. **a** Broadening across the visible spectrum is replicated. **b** Pressure dependence is very clear and accurately reproduced. **c** As pressure increases, pulse bandwidth increases. Simulated and experimental values show great agreement. **d** Evolution of the spectrum as the pulse propagates through the fiber.

trum in red. The linear absorption spectrum was modelled as a sum of Gaussian peaks corresponding to excitonic resonances, in addition to a polynomial background [23]. The dotted lines in figure 6.4a and b correspond to the two lowest excitonic resonances. The laser spectrum is broad enough to completely cover both excitonic peaks, as well as any sub-resonant features associated with multiexcitonic emissive states. Figure 6.4b shows a 2DES spectrum acquired at T_2 = 250 fs. The well resolved diagonal peaks are evidence of the good spectral power at higher energies. To demonstrate stability of the system, the 2DE spectra were acquired at many population times over the course of several hours. Traces along the population time at three loactions along E_1 , E_3 are shown in figure 6.4c. At all three locations a beating in the 2DES signal is apparent at the LO phonon frequency of 208 cm⁻¹. Also evident is a phase change between the three curves, which would be expected for coherent electron-phonon coupling [3]. This was also shown in CdSe / CdS DiRs in figure 4.7. To isolate the beating signal, each transient was modelled with a decaying exponential and the residuals were Fourier transformed. The results of this analysis are shown in figure 6.4d. For reference, the LO phonon frequency of CdSe is shown as a vertical dashed line. The clarity of vibrational coherence, and the obvious phase shifts

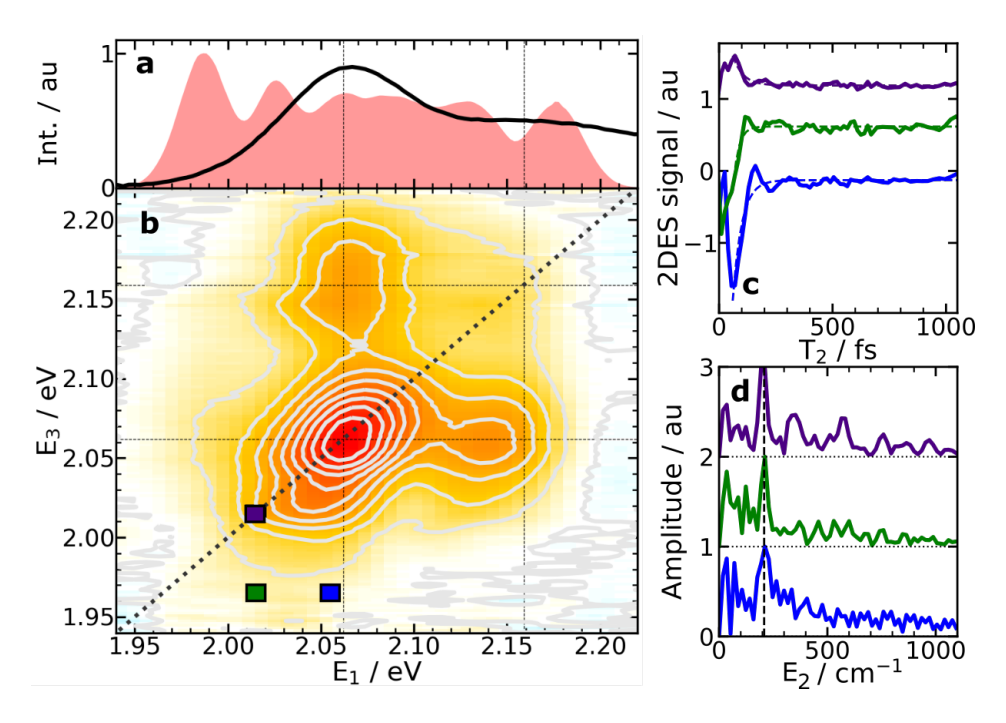


Figure 6.4: 2DES experimental results on CdSe quantum dots. **a** Linear absorption of the sample (black solid line) and laser spectrum (red filled area) **b** A 2D spectrum at T_2 = 250 fs. dotted vertical and horizontal lines indicate excitonic resonances of the sample. **c** Traces of the 2DES spectrum along T_2 (solid) and exponential models (dashed) used to fit them. **d** Fourier transform of the fit residuals. Dashed line shows the LO mode of CdSe at 208 cm⁻¹

with movement along either the E_1 or E_3 axis, demonstrates the suitability of this light source for 2DES.

6.4 Conclusion

In conclusion, we have demonstrated the feasibility and strength of using an OPA to drive tunable supercontinuum generation in Ar-filled hollow-core fibres. This method opens up the sample space of 2DES experiments to the bandwidth of an OPA and the resonances of noble gases (roughly 0.5 to 2.5 eV if difference frequency and fourth harmonic generation aren't included). This method would work very well in the near to mid

IR, where the signal and idler wavelengths provide more pulse energy and the central wavelength is further from plasma generation. Developing light sources is an important endeavor for the overall development of 2DES, as the excitation source is fundamentally linked to the samples that can be probed and the artifacts present in the data. This work presents an improvement in the dynamic range available to 2DES experiments.

Bibliography

- [1] Gellen, T. A.; Lem, J.; Turner, D. B. Nano Lett **2017**, 17, 56.
- [2] Seiler, H.; Palato, S.; Sonnichsen, C.; Baker, H.; Kambhampati, P. *Nano Letters* **2018**, 18, 2999–3006.
- [3] Palato, S.; Seiler, H.; Nijjar, P.; Prezhdo, O.; Kambhampati, P. *Proceedings of the National Academy of Sciences of the United States of America* **2020**, 117, 0–6.
- [4] Liu, A.; Almeida, D. B.; Bae, W. K.; Padilha, L. A.; Cundiff, S. T. *Physical Review Letters* **2019**, 123, 57403.
- [5] Seiler, H.; Palato, S.; Sonnichsen, C.; Baker, H.; Socie, E.; Strandell, D. P.; Kambhampati, P. *Nature Communications* **2019**, *10*, 1–8.
- [6] Thouin, F.; Neutzner, S.; Cortecchia, D.; Dragomir, V. A.; Soci, C.; Salim, T.; Lam, Y. M.; Leonelli, R.; Petrozza, A.; Ram, A.; Kandada, S.; Silva, C. PHYSICAL REVIEW MATERIALS 2018, 2, 34001.
- [7] Stone, K. W.; Turner, D. B.; Gundogdu, K.; Cundiff, S. T.; Nelson, K. A. Accounts of Chemical Research 2009, 42, 1452–1461.
- [8] Karaiskaj, D.; Bristow, A. D.; Yang, L.; Dai, X.; Mirin, R. P.; Mukamel, S.; Cundiff, S. T. *Physical Review Letters* **2010**, *104*, 1–4.
- [9] Delmonte, V.; Specht, J. F.; Jakubczyk, T.; Höfling, S.; Kamp, M.; Schneider, C.; Langbein, W.; Nogues, G.; Richter, M.; Kasprzak, J. *Physical Review B* **2017**, *96*, 1–6.

- [10] Caram, J. R.; Zheng, H.; Dahlberg, P. D.; Rolczynski, B. S.; Griffin, G. B.; Fidler, A. F.; Dolzhnikov, D. S.; Talapin, D. V.; Engel, G. S. *Journal of Physical Chemistry Letters* **2014**, 5, 196–204.
- [11] Wilhelm, T.; Piel, J.; Riedle, E. Optics Letters 1997, 22, 1494.
- [12] Arsenault, E. A.; Yoneda, Y.; Iwai, M.; Niyogi, K. K.; Fleming, G. R. *Nature Communications* **2020**, *11*, 1–8.
- [13] Thyrhaug, E.; Tempelaar, R.; Alcocer, M. J.; Žídek, K.; Bína, D.; Knoester, J.; Jansen, T. L.; Zigmantas, D. *Nature Chemistry* **2018**, *10*, 780–786.
- [14] Richter, J. M.; Branchi, F.; Valduga De Almeida Camargo, F.; Zhao, B.; Friend, R. H.; Cerullo, G.; Deschler, F. *Nature Communications* **2017**, *8*, 1–7.
- [15] Adamu, A. I.; Habib, M. S.; Smith, C. R.; Antonio Lopez, J. E.; Uhd Jepsen, P.; Amezcua-Correa, R.; Bang, O.; Markos, C. *Scientific Reports* **2020**, *10*, 1–10.
- [16] Hoang, V. T.; Kasztelanic, R.; Filipkowski, A.; Stępniewski, G.; Pysz, D.; Klimczak, M.; Ertman, S.; Long, V. C.; Woliński, T. R.; Trippenbach, M.; Xuan, K. D.; Śmietana, M.; Buczyński, R. Optical Materials Express 2019, 9, 2264.
- [17] Ma, X.; Dostál, J.; Brixner, T. Optics Express **2016**, 24, 20781.
- [18] Palato, S.; Seiler, H.; Baker, H.; Sonnichsen, C.; Zifkin, R.; McGowan, J.; Kambhampati, P. *Journal of Applied Physics* **2020**, 128.
- [19] Zheng, H.; Caram, J. R.; Dahlberg, P. D.; Rolczynski, B. S.; Viswanathan, S.; Dolzhnikov, D. S.; Khadivi, A.; Talapin, D. V.; Engel, G. S. *Applied Optics* **2014**, *53*, 1909.
- [20] Seiler, H.; Palato, S.; Schmidt, B. E.; Kambhampati, P. Optics Letters 2017, 42, 643.
- [21] Béjot, P.; Schmidt, B. E.; Kasparian, J.; Wolf, J. P.; Legaré, F. *Physical Review A Atomic, Molecular, and Optical Physics* **2010**, *81*, 2–7.

- [22] Zifkin, R.; McGowan, J.; Palato, S.; https://github.com/ry-dgel/self-phase; 2018.
- [23] Zhang, C.; Do, T. N.; Ong, X.; Chan, Y.; Tan, H. S. Chemical Physics 2016, 481, 157–164.

Summary and outlook

In this thesis I have described the important concepts and methods of ultrafast spectroscopy of nanocrystals. In Chapter 1 I described the important consequences of physical confinement on nanocrystals, and how size is a key factor in determining the linear optical properties of a system. In chapter 2 this discussion was expanded to show how size further determines carrier relaxation and recombination. The methods of ultrafast spectroscopy, specifically pump-probe spectroscopy, were also discussed. In chapter 3 the expansion to three pulse multidimensional spectroscopies was introduced. This powerful experiment has the capacity to unravel microscopic dephasing processes that are hidden in linear experiments, and has the potential to isolate interesting signals through phase-matching in frequency, phase, and wave-vector.

These experimental techniques are put to use in examining gain in quantum dot systems in chapter 4. It is found that the CdSe / CdS dot-rod system is a good candidate for a laser gain medium. The rod shell effectively decouples the exciton from the surrounding solvent, and furthermore decouples the electron from the hole through partial delocalization across the CdSe / CdS interface. Chapter 5 displays further pump-probe results that show very different behaviour in ionic CsPbBr₃ nanocrystals. Here, polaron formation leads to a fast dephasing of phonon modes and a second degree of quantum confinement, that arising from the polaronic potential well. Auger recombination in this system occurs as it would for a quantum confined particle, despite the bulk size regime of the nanocrystals studied.

Finally, in chapter 6, I describe a new source for multi-dimensional spectroscopy. By driving an argon-filled hollow-core fiber with an OPA, tunable pulses spanning the visible wavelength range are produced. These are characterized using optical gating techniques and compared to simulation. To demonstrate the excellent stability of the source, a 2DES experiment is performed. Very good results are produced, distinguishing the LO phonon of CdSe nanocrystals.

In terms of multidimensional spectroscopy, there remains much to be done with regards to source development and samples to study. Simulations hint that a fiber with a smaller core diameter should lead to greater broadening, especially for shorter driving wavelengths. One of these fibers arrived just as I was my obtaining the last of my data. It should be a matter of a week or two at most to characterize this source. There is also the possibility of using different gases in the fiber. Argon was chosen because of its' ionisation energy and affordability. By driving the fiber at lower pulse energies, ionisation is less of a concern and gases with lower ionisation energy but higher n_2 can be explored. The pressure range explored in chapter 6 was limited by leaks in the system, by changing out some pieces for higher rated components higher gas pressures can be explored. These developments could expand 2DES in our lab to below 500 nm.

With an OPA-driven fibre and new approaches to pulse shaping CsPbBr₃ nanocrystals could be studied. CsPbBr₃ is an attractive system due to its' relative stability in comparison to CsPbI₃. We have worked with CsPbI₃ in the past [1], and found great difficulty in maintaining sample quality. This was managed through great team effort. Several samples were produced by research intern Etienne Socie and Dallas Strandell, and procedures were developed to prevent sample degradation (synthesis under nitrogen, putting an Argon gas head on the capped sample vials, etc.). Every sample needed its own linear spectroscopy for quality control and to monitor degradation, and this was performed by Harry Baker. Linear spectroscopy on each studied sample was performed at synthesis, immediately before a 2DE run, immediately after a 2DE run, and often in the middle of

a long 2DE run. I was responsible for characterising the optical pulses and preparing the 2DE experiment. Hélène Seiler oversaw the overall effort, monitored and analysed data as it came in, and generally helped out wherever she was most useful. This was an effort that took our entire lab. Turning to CsPbBr₃ could free up other students to developing their own experiments or helping out in other ways instead of constantly turning out and analysing decaying samples.

Another system that has been seeing a lot of attention lately are transition-metal dichalcogenides (TMDCs) [2]. These materials are interesting because of their enormous excitonic binding energy and spin-orbit coupling. This spin-orbit coupling gives their band structure lots of spin texture. Some direct transitions will only excite certain spins and couple to only a particular polarization of light. This opens up the possibility of so-called spin-tronics. TMDCs also have favorable mechanical and electronic properties, which can be tuned through chemistry and layer thickness. There are links between charge density waves and superconductivity in these materials. The large family of TMDCs also offers a plethora of choices to fit our needs in terms of synthesis and instrument capabilities. Our combination of instruments, from 10 fs resolution in 2DES to 100 fs in SRPP to 10 μ s in time-resolved PL, makes us uniquely positioned to probe these new materials.

The common theme to this thesis is electron-phonon coupling in covalent and ionic systems. Each of the last three chapters presented a measure of electron-phonon coupling, from either SRPP as in chapters 4 and 5, or as projections along the population time of a 2DES dataset, as in chapter 6. The important thing to note is the nature of this coupling. We have seen the long-lived periodic modulation of the TA signal that betrays coherent lattice motion. This is the under-damped phonon mode. We have also seen the rapid decay to an equilibrium TA signal, with no periodic modulation. This is the over-damped response of polaron formation. Phonons in TA spectroscopy can be used to infer surface coupling [3, 4]. In 2DES the full phase and frequency information must be

exploited to distinguish vibrational from electronic beats along the population time axis [5]. This thesis highlights this important work, expands on it in chapter 5, and provides an experimental development to further these studies to new samples in chapter 6.

While the evidence for polaron formation is growing rapidly, and I believe there is large consensus in the community as to their existence in perovskite materials, it is still unclear exactly how important polarons are for device performance. In the future, I would like to see more studies that look at the polaron question from more of an applied perspective. Is polaronic screening sufficient to explain the remarkable carrier diffusion lengths[6, 7] or long lifetimes in perovskites? Other fundamental questions are the role of the cation in lead-halide perovskites. Clearly, there are rotational and vibrational modes related to large organic molecules such as methyl-ammonium or formadimium that are absent for inorganic Cs. Do these play an important role in polaron formation rates or energetics? Ultrafast pump-probe spectroscopy has also shown signals that look like a long-lived population of hot carriers can be created in perovskite nanocrystals[8, 9, 10]. This could open up the possibility of defeating the Shockley-Quessier limit of solar cell efficiency by extracting carriers with energy above the band gap[11]. Investigating the nature of these signals is a promising avenue for future research that our lab is well-equipped to explore.

Given enough time, there are several projects I would have liked to explore further. In terms of pump-probe experiments, it would be interesting to look at perovskite samples with quantum confinement and discernible excitonic peaks in their linear spectroscopy. There should be several things that can be teased out through SRPP experiments by tuning the pump frequency into resonance with the various excitonic states that has yet to be explored. For example, gain in CdSe is best when pumping the $|1P_e\rangle$ $|1P_{3/2}\rangle$ transition, and not the band edge transition. A similar thing could happen in perovskites as well. It is already known, for instance, that gain in CsPbBr₃ NCs is quite weak for 3 eV pumping but much larger for band edge pumping at similar carrier densities [12].

Looking at the differences between excitonic states could lead to better lasing media and also yield fundamental insights to material properties. Alternatively, a state-resolved approach can give details about the carrier relaxation process. Instead of 600 meV of excess energy, as in the data found in chapter 5, pumping with only 50 or 100 meV of excess energy could yield totally new results.

It would also be interesting to look for polaron signatures in simpler crystals, such as alkyl halide salts or some of the other examples shown in table 1.1. This has already been done to some extent in the previous millenium [13], and it would be great to see the powerful methods developed over the last 20 years turned towards these simpler systems. New insights could be found that apply to perovskites or other ionic crystals.

Bibliography

- [1] Seiler, H.; Palato, S.; Sonnichsen, C.; Baker, H.; Socie, E.; Strandell, D. P.; Kambhampati, P. *Nature Communications* **2019**, *10*, 1–8.
- [2] Manzeli, S.; Ovchinnikov, D.; Pasquier, D.; Yazyev, O. V.; Kis, A. *Nature Reviews Materials* **2017**, 2.
- [3] Walsh, B. R.; Sonnichsen, C.; MacK, T. G.; Saari, J. I.; Krause, M. M.; Nick, R.; Coe-Sullivan, S.; Kambhampati, P. *Journal of Physical Chemistry C* **2019**, 123, 3868–3875.
- [4] Tyagi, P.; Cooney, R. R.; Sewall, S. L.; Sagar, D. M.; Saari, J. I.; Kambhampati, P. *Nano Letters* **2010**, *10*, 3062–3067.
- [5] Palato, S.; Seiler, H.; Nijjar, P.; Prezhdo, O.; Kambhampati, P. *Proceedings of the National Academy of Sciences of the United States of America* **2020**, 117, 0–6.
- [6] Stranks, S. D.; Eperon, G. E.; Grancini, G.; Menelaou, C.; Alcocer, M. J.; Leijtens, T.; Herz, L. M.; Petrozza, A.; Snaith, H. J. *Science* **2013**, *342*, 341–344.
- [7] Xing, G.; Mathews, N.; Lim, S. S.; Lam, Y. M.; Mhaisalkar, S.; Sum, T. C. *Science* **2013**, 342, 346–347.
- [8] Kahmann, S.; Loi, M. A. Journal of Materials Chemistry C 2019, 7, 2471–2486.
- [9] Nguyen, D. T.; Lombez, L.; Gibelli, F.; Boyer-Richard, S.; Le Corre, A.; Durand, O.; Guillemoles, J. F. *Nature Energy* **2018**, *3*, 236–242.

- [10] Price, M. B.; Butkus, J.; Jellicoe, T. C.; Sadhanala, A.; Briane, A.; Halpert, J. E.; Broch, K.; Hodgkiss, J. M.; Friend, R. H.; Deschler, F. *Nature Communications* **2015**, *6*, 1–8.
- [11] Shockley, W.; Queisser, H. J. Journal of Applied Physics 1961, 32, 510–519.
- [12] Geiregat, P.; Maes, J.; Chen, K.; Drijvers, E.; De Roo, J.; Hodgkiss, J. M.; Hens, Z. *ACS Nano* **2018**, *12*, 10178–10188.
- [13] Iwai, S.; Tokizaki, T.; Nakamura, A.; Tanimura, K.; Itoh, N.; Shluger, A. *Physical Review Letters* **1996**, *76*, 1691–1694.